Prediction of NuMI electron and muon neutrino flux in ICARUS

D. Cherdack, A. Aduszkiewicz, A. Wood

Department of Physics, The University of Houston, Houston, Texas 77204, USA

November 9, 2023

Abstract

The NuMI neutrino flux prediction for ICARUS is extracted using Package to Predict the Flux (PPFX). Systematic effects on the flux due to modeling of the beamline and hadronic interactions are studied. Validity of the simulation's uncertainty characterization for high off-axis angles is evaluated, and potential avenues for improving the prediction and reducing the uncertainties are identified. The predicted electron and muon (anti–)neutrino flux for both forward and reverse horn operating modes is presented with its expected uncertainties. Covariance matrices were calculated and a principal component analysis (PCA) was performed to reduce statistical noise and remove degeneracies. The total uncertainty on the flux in the 0–20 GeV range of neutrino energy was found to be 11.5% (7.0%) for ν_μ (ν_e) incident on the ICARUS detector.

SBN Document 27384

Contents

List of Figures

List of Tables

ACKNOWLEDGEMENTS

We would like to thank

- Linda Cremonesi for help with accessing the simulation datasets and providing crucial information about them,
- Leo Aliaga Soplin and other members of the PPFX group for multiple discussions which allowed us to develop the analysis procedure,
- Vittorio Paolone, Leo Aliaga Soplin, and Stephen Dolan for reviewing the note and providing helpful remarks and comments,
- Robert Hatcher and Minerba Betancourt for help in analyzing data in the dk2nu format,
- Nilay Bostan for access to the 1 MW dataset.

This text is based upon work that is supported by the Visiting Scholars Award Program of the Universities Research Association 21-F-01. Any opinions, findings, and conclusions or recommendations expressed in this material are those of the author(s) and do not necessarily reflect the views of the Universities Research Association, Inc.

1 INTRODUCTION

ICARUS [1, 2] is a 430 t (fiducial volume) liquid argon (LAr) Time projection chamber (TPC) neutrino detector located at Fermi National Accelerator Laboratory (FNAL). ICARUS serves as the primary far detector of the FNAL Short Baseline Neutrino (SBN) program, seeking to resolve to several observed anomalies [3–7]. Many believe that sterile neutrinos are the source of these anomalies and analyses will focus on sterile oscillation searches. The sterile neutrino search utilizes neutrinos produced by the FNAL Booster Neutrino Beam (BNB), and the Short Baseline Near Detector (SBND) which will measure the BNB near the source, before any neutrinos will have had the chance to oscillate to sterile neutrinos. ICARUS is 600 m downstream of the BNB at a baseline consistent with the anomalous sterile neutrino oscillation probability for BNB neutrino energy range. SBND sits 110 m downstream where the anomalous sterile neutrino oscillation probability is negligible [8]. Both detectors lie along the central axis of the BNB.

The ICARUS detector also lies 795 m downstream of the Neutrinos at the Main Injector (NuMI) neutrino beam at an off axis angle of 5.75°. From this vantage point, ICARUS will be able to measure neutrino interaction rates on Ar nuclei in a LArTPC detector, which will be an important input to the DUNE physics program with a 40 kt far detector fiducial volume [9]. The large off-axis angle provides a significant flux of both muon and electron flavor neutrinos and antineutrinos in both the neutrino-focusing (FHC) and antineutrino-focusing (RHC) beam configurations given a planned exposure of $3 \cdot 10^{20}$ protons on target (POT) per year over a 3-year period. This should nominally allow for high statistics absolute and relative interaction cross section measurements of all four flavors. The high-resolution, low-threshold detector opens up possibilities for differential measurements in multiple kinematic quantities for exclusive topological interaction channels. However, several challenges still exist that may reduce the statistical power of the data.

The NuMI flux (via the simulation described in Sec. 2.2) has not been well characterized at large off-axis angles, e.g. 5.75°. The on-axis neutrino beam is produced primarily by well-focused pions that are created in proton-carbon interactions in the target, and that decay in NuMI decay pipe. The flux at ICARUS, presented in Fig. 1.1 and Tab. 1.1, on the other hand, is produced by a combination of muon decays (low energies < 0.5 GeV), pions either outside of the well-focused phase space (π^+ in FHC and π^- in RHC) or unfocused (π^- in FHC and π^+ in RHC, moderate energies 0.5 – 2 GeV), and high-angle kaon decays (high energies > 2 GeV). These parent particles are produced in interactions of multiple hadron flavors over a wide range in energy on a variety of nuclei, and occurring in multiple locations within the beamline facility. This differs from the on-axis and near-on-axis fluxes of MINERνA and NOνA, respectively (henceforth referred to as the on-axis flux in this note), where the majority of neutrinos in the flux peak come from focused primary (resulting from p-C interactions in the target) pion decays within the decay pipe. (The MicroBooNE experiment also studied the NuMI flux at a high, 8° off-axis angle. Details can be found in Chapter 5 of Ref. [10].)

These differences lead to many sources of potential flux model uncertainties that have not been previously constrained, or even studied. Large amounts of data for pro-

Table 1.1: Composition of the uncorrected NuMI flux in ICARUS, integrated in the 0–20 GeV range, for both FHC and RHC operating modes, as a percentage of the total flux. Significant wrong-sign contamination can be found in each case, where the unfocused flux is > 50% of the focused.

FHC Flux (%)				RHC Flux (%)			
ν_e	$\bar{\nu}_e$	ν_μ	$\bar{\nu}_\mu$	ν_e	$\bar{\nu}_e$	ν_μ	$\bar{\nu}_\mu$
1.3	0.7	62.7	35.3	0.9	1.1	38.4	59.6

tons scattering off of carbon exist, which account for the vast majority of the interaction that produce near-on-axis neutrinos. However, data for interactions of non-proton hadrons, and off of non-carbon target nuclei (in the kinematic regions of interest and with sufficient detail to be useful), is relatively sparse. In this note, the authors use the PPFX software package [11–14] to study the sources of neutrinos at ICARUS, how they are treated in the simulation, and whether the assigned uncertainties on the relevant processes are adequate for ICARUS analyses. Based on these studies, recommendations for further data-based constraints, most of which will require further data from NA61/SHINE [15] and EMPHATIC [16], are made.

Once the model and related uncertainties have been characterized, PPFX is used to extract the current flux uncertainties at ICARUS as a function of neutrino energy, neutrino flavor and beam horn current i.e. running mode. Uncertainty correlations between bins of energy, flavor, and mode are also considered. These uncertainties and their correlations are then propagated to determine the flux error on potential measurements to determine the total flux error on various analyses.

It should also be noted that the ICARUS detector is not magnetized, so it cannot sign-select the outgoing charged leptons from charged-current (CC) interactions, at least on an event-by-event basis. While track and shower characteristics can be used to estimate the lepton sign ratio statistically, the relative $\bar{\nu}/\nu$ flux prediction (and the associated uncertainties) will be an important component in any attempt at a sign selected analysis.

The note is organized as follows. Section 2 introduces the software tools on which the analysis was based. Section 3 describes the simulated NuMI flux datasets used and compares the properties of the off-axis flux in ICARUS with on-axis flux. Section 4 presents analysis of flux uncertainties related to hadron production modelling and beamline configuration. Section 5 summarizes the findings of the note and discusses potential future development. Additional materials are provided in appendices; in particular, Appendix O includes tabulated neutrino flux uncertainties.

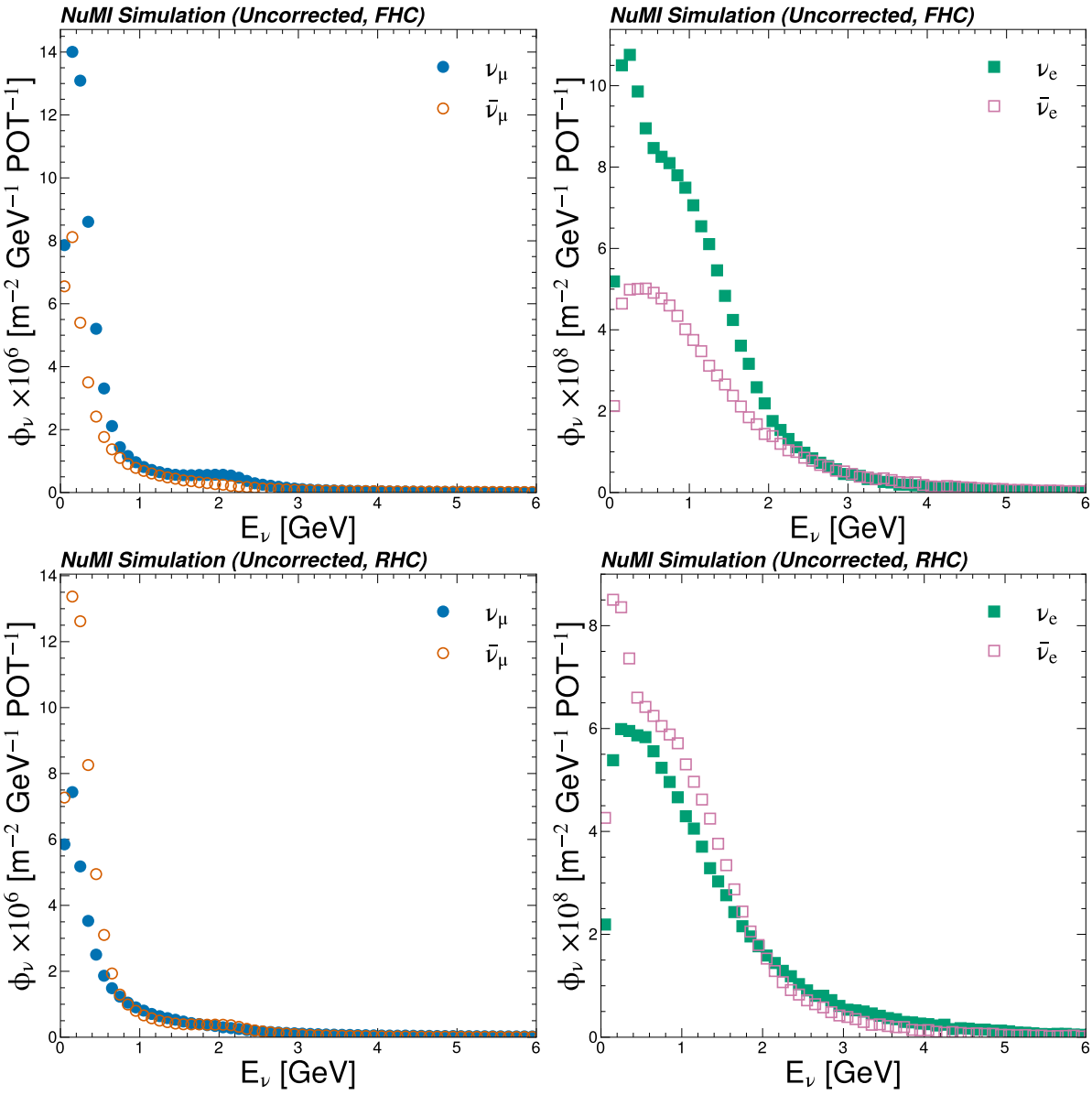

Figure 1.1: NuMI flux with forward (*top*) and reverse horn current configuration (*bottom*) in ICARUS. It does not include corrections for hadron modelling effects and systematic uncertainties, introduced later in this note.

2 ANALYSIS TOOLS

2.1 NuMI Beamline

The Neutrinos at the Main Injector beamline [17] was constructed for the on-axis MINOS experiment, later also used by on-axis MINERνA and ArgoNeuT, and 14.6 mrad (0.867°) off-axis NOνA experiment [18]. The beamline utilizes 120 GeV proton beam from the Fermilab Main Injector by directing them onto a 120 cm long carbon target [19], which produces a shower of hadrons. Two magnetic *horns*, located downstream of the target, bend the positively charged hadron trajectories along the beam axis, and the negatively charged ones away from the beam axis, when powered in *forward horn current* (FHC) mode, and vice versa in *reverse horn current* (RHC) mode. The focused hadrons then proceed towards a 700 m long helium filled *decay pipe*, where a large fraction decay into neutrinos and corresponding charged leptons (mostly muon neutrinos and muons). The ICARUS LArTPC is located approximately 80 meters above the end of the decay pipe (see Sec. 3.2 for details).

The horns focus pions in a specific energy range determined by the horn current and their relative positions with respect to the target. Pions outside of that range and of the wrong sign are not focused, and do not decay into neutrinos along the beam axis, and thus do not contribute to the on-axis and near-on-axis fluxes. Switching between forward and reverse horn current switches from a neutrino dominated flux to an antineutrino dominated flux composition on axis. As the primary sources of ν_μ are π^+ and K^+, the FHC flux will consist predominately of ν_μ; similarly, the RHC flux of $\bar{\nu}_\mu$. The primary sources of ν_e are K^+ and K^0_L, approximately in similar fractions of each. The contribution of charged kaons is therefore controlled by the horn current polarity, but the horns do not affect neutral kaons. High energy, forward going hadrons are less affected by the horns, which leads to high antineutrino contamination on-axis at high neutrino energies. As will be demonstrated in Sec. 3.3, the efficacy of the horns also diminishes for particles produced at high off-axis angles. This also leads to large antineutrino and contamination at highly-off-axis detector positions. Kaon decay kinematics produce ν_e over a wide angular range. Thus, forward going focused kaons produce a relatively high energy ν_e flux on axis that shifts to lower energies with increasing off-axis angle. Muons decay to both ν_μ and ν_e with relatively low energies and small decay angles compared to kaon decays. While the ν_μ contribution is overwhelmed by pion decays at those energies, the ν_e contribution is significant since only ~0.012% of charged pions decay to ν_e.

2.2 The NuMI Flux Simulation

The NuMI flux is simulated using the GEANT4 9_2_p03 package g4numi using hadronic model FTFP_BERT [11, 20]. The geometrical model was developed for the MINOS experiment and subsequently upgraded for MINERνA [12] and used by NOνA. The impact of additional unmodeled materials was also studied, specifically material away from the beam axis, which may impact flux at high off-axis angles. It was found that

including the Horn 1 current strips could improve the flux prediction, but the effect is likely to be small, see Sec. 3.5.

The NuMI beamline was recently upgraded to allow for 1 MW beam power from the Main Injector. The new high power NOνA target was installed in 2019 and the 1 MW horn system was installed in 2020 [19]. The geometry file used for beam simulations was updated to incorporate the changes and new flux files have been produced. However, the new flux files do not include the full suite of beamline focusing systematic alternative runs required for a full error analysis, and thus are not used in this note. Studies comparing the fluxes from the two geometries are shown in Sec. 4.2.4. The impact of the change is mostly small, but not entirely negligible. However, given the sample sizes the statistical uncertainties on the correction factors are on par with the size of the corrections, the authors recommend taking the difference as systematic rather than as a correction. An effort to produce a full suite of nominal and systematically altered samples with the updated geometry should commence in Fall 2023, after which this process of uncertainty propagation studies and of PPFX flux corrections should be repeated. The tools cited in Appendix A of this note should be able to be easily updated to repeat the analysis and production of analysis data products.

2.3 The dk2nu Beam Simulation Data Format

The simulated data is stored in the *dk2nu* format [21]. A dk2nu entry in the file contains detailed information about the decay point of a neutrino and its entire ancestor particle chain. This chain includes all the particles leading up to the primary beam proton and their interactions. As an example, consider an interaction between a proton incident upon the carbon target that produces a positively charged pion, π^+. This pion then interacts again within the carbon target, creating another π^+. This second pion subsequently decays into a positively charged muon (μ^+) and a muon neutrino (ν_μ), which in turn decays into a positron (e^+), an electron neutrino (ν_e), and an anti-muon neutrino ($\bar{\nu}_\mu$). In this scenario, the dk2nu file would contain three separate entries for the neutrinos, with the following ancestor chains:

- $p+C \rightarrow \pi^+ + C \rightarrow \pi^+ \rightarrow \nu_\mu$,
- $p+C \rightarrow \pi^+ + C \rightarrow \pi^+ \rightarrow \mu^+ \rightarrow \bar{\nu}_\mu$,
- $p+C \rightarrow \pi^+ + C \rightarrow \pi^+ \rightarrow \mu^+ \rightarrow \nu_e$.

The simulation chain does not predict neutrino decay in a particular direction. Instead, neutrino energy in the frame of the decaying parent is retained. When analyzing the simulated data, the probability density of the neutrino reaching the detector located at a particular location is calculated based on its parent mass, momentum, and polarization in the case of μ decays. This greatly improves available statistics, as all neutrinos are assumed to reach the detector with an appropriate probability weight w_{geom} [m^{-2}].

Neutrinos with decay chains including particles considered as over-represented are randomly excluded from the data file with an arbitrarily chosen probability $(1 - p)$ depending on the particle type, energy, and number of such interactions. If an entry is saved, it includes the value $w_{\text{imp}} = p^{-1}$, referred to as the *importance weight*. When

analyzing the data, the total weight of each neutrino used in determining the flux at a particular angle needs to be multiplied by this importance weight.

The total weight w_l for l-th neutrino entry is therefore

$$w^l = w^l_{\text{geom}} \cdot w^l_{\text{imp}} \,, \tag{2.1}$$

and the total flux per NuMI beam proton in a given energy bin i is

$$\phi^i = \frac{\sum_l w^{l,i}}{\text{POT}} \,, \tag{2.2}$$

where POT stands for the total simulated *protons on target* in the analyzed data set, and the statistical uncertainty in the energy bin i is

$$\sigma^i_{\text{stat}} = \frac{\sqrt{\sum_l (w^{l,i})^2}}{\text{POT}} \,. \tag{2.3}$$

It should be noted that the flux files (with the dk2nu format) are used directly by GENIE in the event generation procedure (via the GENIE Flux Driver), and the dk2nu record is saved along with each event. These same files are used as the input to the work presented here. While it is possible to construct flux error estimates on an event-by-event basis at analysis time, this process is computationally expensive and the only relevant degrees of freedom are the neutrino energy and flavor. Thus, this external analysis of the flux can be done externally, characterized in those variables, and easily propagated to events at analysis time.

2.4 Package to Predict the Flux (PPFX)

The Package to Predict the Flux (PPFX) corrects neutrino flux prediction and calculates systematic uncertainties related to hadron production cross sections. The corrections errors are propagated from experimental data on hadron production where available. In cases where experimental data is not available, data-like templates are constructed from GEANT4 (using the same physics models in the flux simulation to preserve central values) and conservative bin to bin hadron production uncertainties are assumed [11–14]. When available, covariance between measurements (bin-to-bin and sample-to-sample) are included. When covariance are not available (some data sets and GEANT4-based templates) they are assumed. The exact details of the assumed errors and covariances can be found in the relevant citations. GEANT4 templates corresponding to each data sample are also generated using the same binning as the data.

PPFX corrections are extracted by taking the ratio between the data and GEANT4 templates. For the cases where no data is available, the templates are identical and the extracted corrections are unity. The correction applied to each neutrino is the product of the ratios for the processes associated with hadron interaction chain associated with the neutrino. This interaction chain is stored in the dk2nu format. These correction factors are stored as weights.

In order to propagate the associated hadron production uncertainties, PPFX creates a number of *universes* in which the interaction cross sections are randomly altered based

on experimental uncertainties and correlations. The GEANT4 template "data" will vary based on the assigned uncertainties, and thus non central value universes will produce ratios (and thus weights) that differ from unity. The hadron interactions model uncertainties are propagated to the neutrino flux by analyzing the distribution of the neutrino fluxes between the universes, as will shown in Sec. 4. (Other propagation methods exist, but this is the method used in PPFX and adopted by all NuMI beam simulation Users to date.)

The PPFX output files used for this note contained the following information:

- *nominal* flux histograms at the ICARUS detector location, calculated without any corrections to the hadron interaction cross sections,
- *central value* flux, calculated by correcting the hadron interactions based on the experimental hadron interaction cross sections,
- 100 *universes* with randomly modified hadron interaction cross sections, as described above,
- number of *protons on target* (POT) in the input file, needed to normalize the results.

2.4.1 Interaction Channels in PPFX

The hadron production channels that PPFX uses to generate the flux universes are:

- **p + C $\rightarrow$ $\pi^{\pm}$ + X:** inclusive charged pion production in p+C interactions,
- **p + C $\rightarrow$ K + X:** inclusive kaon production in p+C interactions,
- **n + C $\rightarrow$ $\pi^{\pm}$ + X:** inclusive charged pion production in n+C interactions, *spectra estimated based on p+C data and isospin symmetry*,
- **p + C $\rightarrow$ N + X:** inclusive nucleon production in p+C interactions,
- **($\pi^{\pm}$, K) + A $\rightarrow$ ($\pi^{\pm}$, K, N) + X:** meson interactions, *no experimental data*,
- **N + (Al,Fe) $\rightarrow$ X:** interactions of nucleons on aluminum and iron; new channel added for the purpose of this analysis, see Sec. 2.4.2, *no experimental data*,
- **N + A $\rightarrow$ X:** interactions of nucleons on nuclei, not included in other channels; this contribution includes p+C (50%) and n+C (20%) interactions not covered by experimental data, *no experimental data*,
- **others:** interactions not included in the other channels; primarily interactions of Λ, $\overline{\text{p}}$ and $\overline{\text{n}}$, *no experimental data*,
- **attenuation:** correction for the probability of a particle interacting in a given volume, or passing without interacting, based on data on total inelastic cross section measurements of p+C, $\pi^{\pm}$+C, $\pi^{\pm}$+Al, $K^{\pm}$+C and $K^{\pm}$+Al interactions.

In order to correct the models, PPFX used results from experiments measuring hadron production and interaction cross sections on thin targets. The experimental data does not cover all kinematic regions of the phase space, in particular the very forward region, nor all relevant interaction energies; for some channels, there was no experimental data at all. In such cases, PPFX assigned a conservative estimate of 40% uncertainty to the hadron production cross section. The details of the data sets used and implementation of uncorrelated and correlated uncertainties are complex, and can be found in Refs. [11, 12].

There is an ongoing effort to collect and implement more recent data into PPFX, see e.g., Ref. [22], this analysis used only data sets from the original PPFX version. The authors suggest that this analysis be reproduced with the updated version of PPFX once a significant amount of new data has been incorporated ion PPFX and validated.

2.4.2 Modifications to PPFX

Three alterations to PPFX were tested and ultimately adopted for this analysis. The first set of changes were related to grouping of interaction channels related to interactions with non-carbon nuclear targets, non-nucleon projectiles, and p+C interactions where no data is available. These changes allowed for better understanding of the exact processes that were impacting the 5.75° off-axis flux. The second change was to neglect uncertainties related to forward-going nearly-elastic nucleon scatters. The third change involves fixing a bug in the propagation of meson interaction uncertainties. They are described in more detail below.

Separating interactions on iron and aluminum from the N+A channel. PPFX, as designed, reports the uncertainties on p+C interactions covered by data and by all other p+A interaction lumped together. The p+A contribution to the total flux uncertainty is subdominant in the on-axis flux, and this categorization was deemed sufficient. (Although this is changing as additional p+C data continues to suppress the dominant p+C uncertainties.) As shown in Sec. 3.4, there is a significantly larger number of interactions on Al (horn magnets) and Fe (steel within the decay pipe walls) for the flux at high off-axis angles as compared to the on-axis flux for which PPFX was originally developed. In order to quantify the impact of these interactions on the flux, N+Al and N+Fe interactions were separated into additional channels that exclusively contained nucleon interactions on aluminum or iron. After separating the N+(Al,Fe) channel, 72% of the remaining interactions in the remaining interactions covered by the N+A channel are N+C interactions not covered by the other channels. (Note that when p+C data is available, the impact of proton and neutron scattering uncertainties are reported separately as p+C and n+C. Otherwise, they are combined into a nucleon scattering channel N+A.)

Neglecting quasi-elastic and similar interactions on nucleons. Quasi-elastic (and similar) interactions are defined by final states where the outgoing primary hadron has the same flavor and nearly the same momentum as the incoming hadron. The lack of data for these interactions comes from the inability of the experiments (whose data is used by PPFX) to measure forward-going hadrons over a small angular range. This sets a strict limit on the transverse momentum difference between the incoming and outgoing primary hadrons.

The multiplicity and momenta of low momentum particles produced in these interactions can vary widely. However, due to conservation of energy, at most only one outgoing particle can carry the majority of the projectile momentum. Therefore, the uncertainty on the differential cross section does not impact the probability of forming additional neutrinos of interest. Moreover, since the flavor of the produced particle

is the same as that of the projectile, and their momenta are similar, the number of particles available for production of relevant neutrinos, and their properties, would be very similar with or without such interaction.

As of now, PPFX includes no data on the production of hadrons in this very forward region, and thus applies a conservative 40% uncertainty to the corresponding bins of differential cross section. While the assumption of 40% uncertainty in the unconstrained region of the simulated spectrum is not unreasonable, such interactions have little impact on the predicted flux since the properties of the outgoing primary hadron are essentially unaffected. Thus, the authors argue that the additional 40% uncertainty propagated to neutrinos for each of these interactions is needlessly conservative, and leads to overestimation of the flux uncertainties.

PPFX was thus modified such that the N+A channels no longer assign additional weights to interactions matching the following criteria:

The produced particle is of the same flavor as the projectile, and either

- x_{F} (Feynman x) of the produced particle exceeds 0.95, or its
- p_{T} (transverse momentum) expressed in GeV/c is less than $(x_{\mathrm{F}} - 0.5)$.

The above accounts for 36% of interactions from the N+A channel. Removing the associated weights results in reduction by a factor varying from 5 at low neutrino energies, to 2 at 6 GeV. While the authors believe the above arguments are valid, the impact is large and the exact phase space cuts are somewhat arbitrarily defined, so they concede that this procedure has increased the "uncertainty on the uncertainty" at low neutrino energies.

Fixing a bug in PPFX A minor bug was found in PPFX that affects the characterization of uncertainties associated with meson re-interactions. The bug was caused by an error in the calculation of the Feynman x (x_{F}) for the outgoing hadron. (The mass of the target particle was assumed to have the mass of the incoming particle. This does not affect nucleon-nucleon interactions, but causes a large bias for lighter mesons.) The bug causes meson interactions to be grouped incorrectly in the flux universe based error propagation scheme. The impact of the bug was to increase the correlations between E_ν/flavor bin uncertainties. The change to PPFX was to fix the bug and rerun. Given that incident meson interaction uncertainties dominate the flux error budget, the impact of this small change is significant. The details of the meson interaction uncertainty propagation, the bug, its fix, and the impact are described in Appendix B.2. Details on the associated uncertainties are given in Sec. 4.2.1.

3 THE NUMI BEAM AT ICARUS

This Section characterizes the NuMI beam simulation at the off axis-angle subtended by the ICARUS detector. Understanding the simulated hadron interaction chains that contribute to neutrinos which will reach ICARUS is crucial to evaluating the current set of systematic uncertainties developed for on-axis detector positions. Information gleaned from the studies described in this section were used to motivate the changes to PPFX described in Sec. 2.4.2, gave the intuition required to understand the error characterizations shown in later Sections, and demonstrated the negligible impact of common analysis simplifications at high off-axis angles.

3.1 Analyzed Data Samples

The studies presented in this note used the NuMI Flux Monte Carlo simulation samples generated for the third NOνA analysis of the beam focusing systematic uncertainties [18, 23]. The data was simulated for the nominal beamline configuration, along with 24 additional samples with varied configurations (see the list of configurations in Appendix J). Each of these samples was generated for each of the two running modes: FHC and RHC.

In each of the 50 samples, interactions of $500{\times}10^6$ (120 GeV/c Main Injector) *protons on target* (POT) were simulated. This corresponds to statistics of $150{\times}10^6$ saved simulated neutrinos. (Note, the simulation does not save all neutrinos, as explained in Sec. 2.3). (Additional samples with altered values of the Earth magnetic field in the decay pipe were used for the analysis in Appendix D.) This section presents results obtained from studying the FHC samples only, while companion plots for RHC can be found in Appendix C. Both FHC and RHC samples are used in subsequent Sections. The MC was processed using PPFX along with standalone code that reads the dk2nu file structure.

3.2 Detector Location

The GENIE flux driver correctly samples the flux variations across the detector when generating neutrino interactions. However, it is difficult to study the flux independently across the solid angle of the detector. Instead, a single ray between the target and the center of the detector is defined. (Studying the flux across the detector volume requires determining the correct weighted average over all potential rays that intersect the TPC volume. The flux driver accomplishes it through an accept-reject algorithm when swimming neutrinos through the detector.)

Along with studies of the flux change across the detector volume, studies of the change in the PPFX based flux corrections and uncertainty characterizations were also done to ensure that any data products extracted for analysis were unaffected by the flux difference. These studies demonstrated that, while the flux changes significantly across the detector, the fractional error on the flux is stable.

A dedicated study was performed to find the exact ICARUS detector position at Fermilab and specifically with respect to the NuMI coordinate system. This lead to a re-

vised the detector geometry [24], and required deriving the coordinate transformations to calculate detector position in NuMI beam coordinates [25]. The cryostat locations provided by the Fermilab survey team are given with precision of fraction of a mm, and the internal ICARUS TPC position w.r.t. to the cryostat is known with a precision of an inch.

This study was necessitated by the discovery that the actual detector position differed from some of the previously used values from early construction plans. The difference was on the order of several meters. As will be demonstrated, the neutrino flux is quite sensitive to the off-axis angle, which for ICARUS depends mostly on the vertical coordinate of the detector position, i.e., elevation or y coordinate in the NuMI system.

The origin of the NuMI coordinate system is located approximately at the front face of Horn 1 on the primary proton beam axis. In ICARUS coordinates, the ICARUS detector is located at (315.12 m, 33.64 m, 733.63 m) with respect to the NuMI origin [25]. As will be shown in Sec. 3.6, the majority of NuMI neutrinos reaching ICARUS originate from the very beginning of NuMI beam line and angular dispersion is very small, thus this vector provides a good approximation of the angle at which NuMI neutrinos enter the ICARUS detector. The origin of the ICARUS coordinate system lies 23 cm above the center of TPC active volume [24].

In NuMI coordinate system, the z axis is oriented along the NuMI beam axis, northwest, slightly downwards, x is horizontal, to the southwest, and y is almost vertical, perpendicular to x and z [25]. Table 3.1 lists selected positions in NuMI coordinates. In this note, the center of the active volume is used when calculating neutrino flux. In ICARUS simulation [1], the origin of the coordinate system is used.

Table 3.1: ICARUS detector coordinates, denoted with $^{\mathrm{I}}$, expressed in NuMI beamline coordinates with $^{\mathrm{N}}$, as well as the angle θ between the line connecting the point with NuMI origin, and the NuMI beam axis. The table lists the origin of the coordinate system, the geometrical center of the TPC system, and points above and below the geometrical center, at the limits of the TPC active volume.

		x^{N} [m]	y^{N} [m]	z^{N} [m]	θ [mrad]	θ [°]
ICARUS origin	$x^{\mathrm{I}} = y^{\mathrm{I}} = z^{\mathrm{I}} = 0$	4.50	80.15	795.11	100.6	5.77
TPC center	$y^{\mathrm{I}} = -0.23\,\mathrm{m}$	4.50	79.92	795.13	100.3	5.75
TPC bottom	$y^{\mathrm{I}} = -1.82\,\mathrm{m}$	4.50	78.35	795.22	98.4	5.64
TPC top	$y^{\mathrm{I}} = +1.35\,\mathrm{m}$	4.50	81.50	795.03	102.3	5.86

Figure 3.1 shows the dependence of the neutrino energy spectrum on the off-axis angle of the detector. Dk2nu files include information on the momentum vector of the

[1] https://github.com/SBNSoftware/icaruscode/commit/56eea5331147ec1ab324e6a73d15a7c773693875

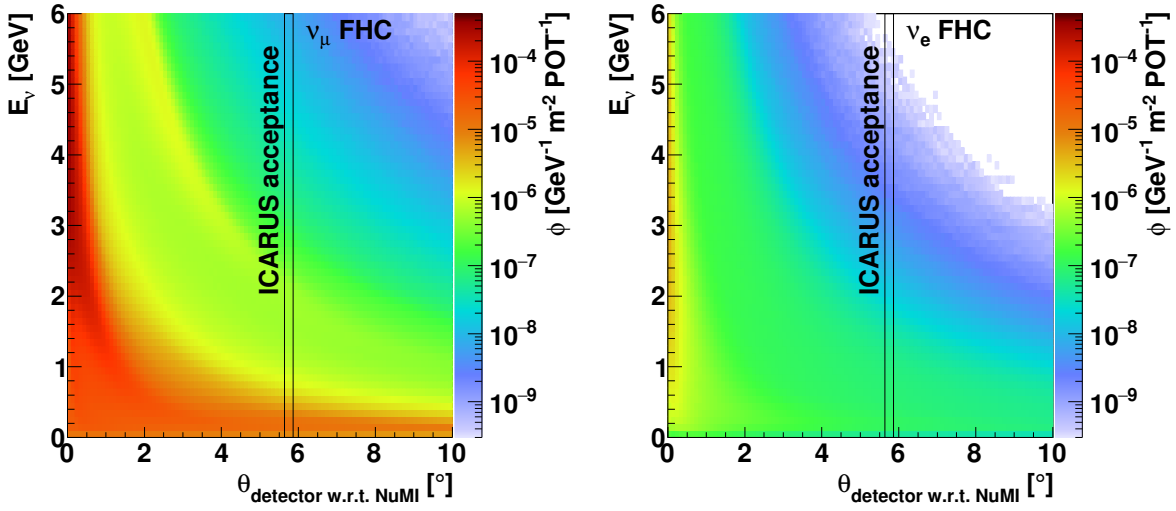

Figure 3.1: Neutrino energy spectrum as a function of angle with respect to the NuMI beam axis, at the same distance (z coordinate) as ICARUS for ν_μ (*left*) and ν_e (*right*). The vertical lines show the actual angular acceptance of ICARUS. Corresponding antineutrino and RHC plots are shown in Fig. C.1.

neutrino parent, as well as neutrino energy in the parent frame of reference. Based on this information, the neutrino energy in the detector at a given location is then:

$$E_\nu^{\text{LAB}} = M \cdot E_\nu^{\text{CM}} \,, \tag{3.1}$$

where,

$$M = \frac{1}{\gamma(1 - \beta \cos\theta_{\text{parent-}\nu})} \,, \tag{3.2}$$

where $\gamma = (1-\beta^2)^{-1/2}$, β is the velocity of the parent particle in the laboratory frame divided by c, and $\theta_{\text{parent-}\nu}$ is the angle between the momentum vectors of the decaying parent and the neutrino [26]. The flux density is thus:

$$\phi^{\text{LAB}} \mathrm{d}\Omega^{\text{LAB}} = M^2 \cdot \phi^{\text{CM}} \mathrm{d}\Omega^{\text{CM}} \,. \tag{3.3}$$

The position and angular range of ICARUS is indicated by the two vertical lines in each plot. While the angular size of the ICARUS TPCs is only 0.2° (see Tab. 3.1), for parent mesons, β is close to 1 at the relevant energies of several GeV. As a result, equation (3.2) is very sensitive to the value of $\theta_{\text{p-n}}$. Both the neutrino flux shape and intensity depend substantially on the detector off-axis position. This effect creates a position dependent flux spectrum across the ICARUS detector in the dimension most closely aligned with the angular spread, namely the y-axis (vertical).

Figure 3.2 shows that the electron to muon neutrino flux ratio is higher in ICARUS, in comparison to on-axis flux.

The change in flux across the ICARUS detector, up to the edges of the TPC active volume, were studied by individually varying the flux position along the x, y, and z

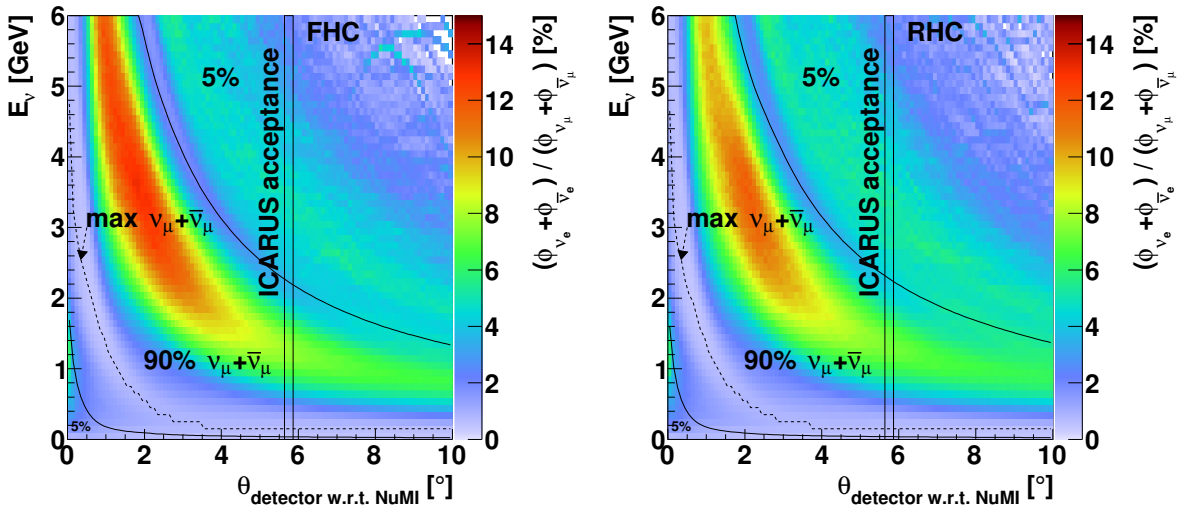

Figure 3.2: Ratio of electron to muon neutrino flux, as a function of angle with respect to the NuMI beam axis, at the same distance (z coordinate) as ICARUS. The vertical lines show the actual angular acceptance of ICARUS. The continuous curves show the middle 90% of the muon neutrino flux, and the dashed line shows its maximum (mode).

axes of the TPC. Figure 3.3 shows that the flux varies by up to ±10% between the largest and smallest off-axis angles, and generally varies smoothly through that range. The dependence is mostly symmetric with respect to the center of the TPC system, thus the flux at the middle point should represent the flux in the full detector well. However, vertical misalignment of the detector would introduce a bias of up to 0.6% per 10 cm of misalignment. The flux dependence on the position along the horizontal axes does not exceed 2% (see Fig. C.2).

3.3 Horn Focusing

Figure 3.4 shows that most of the neutrino parents decay before reaching Horn 2, and many inside Horn 1. As a result, the beam at 5.75° is mostly composed of unfocused or partially focused hadrons. Hadrons producing wrong sign neutrinos are not deflected, as they are for on-axis detector positions. (There is a beam component from focused hadrons that decay in the decay pipe. However, these particles often undergo a secondary interaction within the decay pipe, off helium or the reinforced concrete walls, which deflect the pion direction towards ICARUS.) Figure 3.5 shows significant wrong sign neutrino contribution to the NuMI flux in ICARUS.

3.4 Hadron Interactions

In this Section, the significance of the secondary interactions of particles which eventually decay to neutrinos is studied. In the most simple case, the primary beam from the Main Injector interacts with the carbon target, produces hadrons which are focused by the horns and decay weakly into neutrinos. However, the produced hadrons may

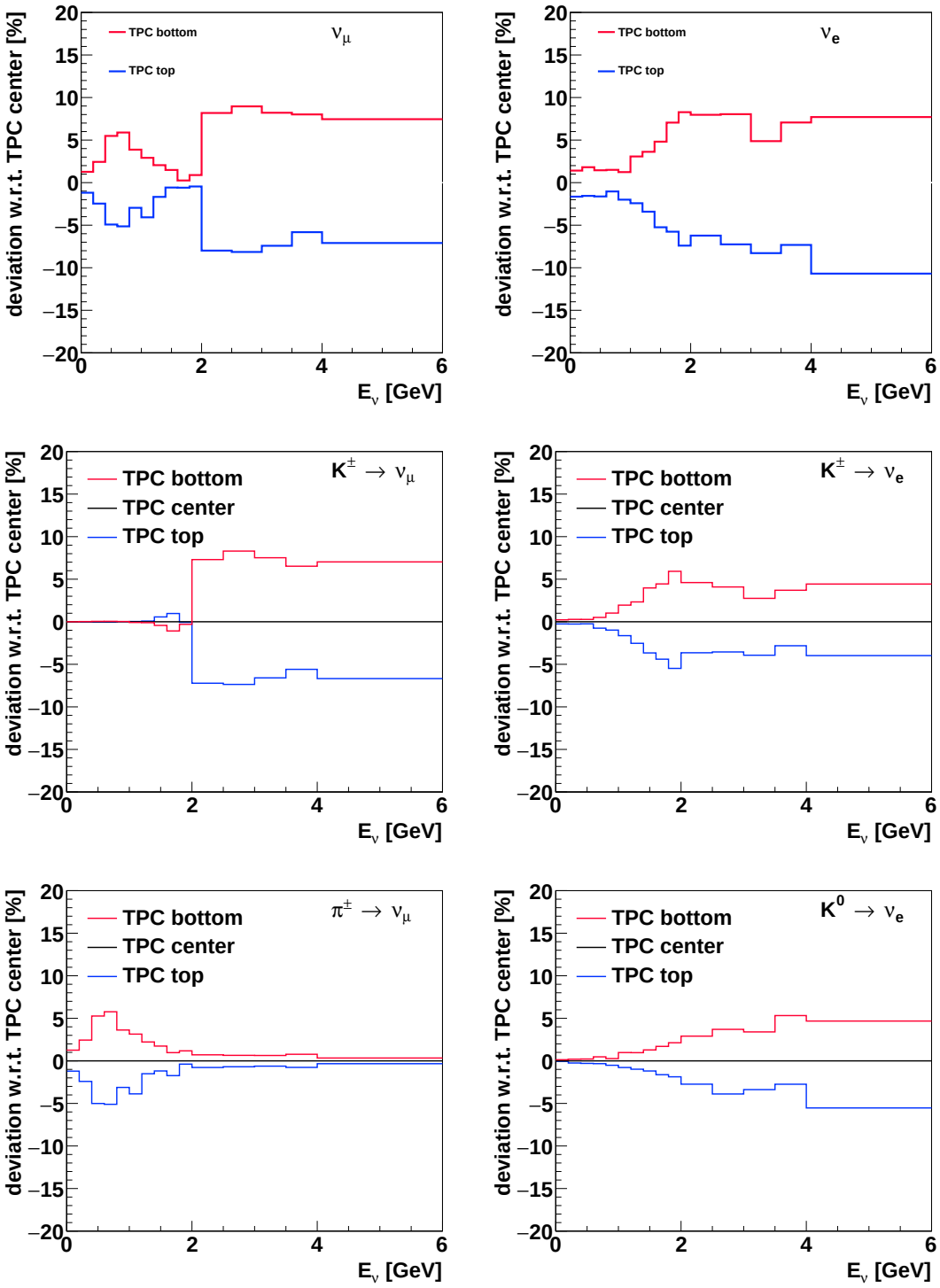

Figure 3.3: *Top:* flux change at the top and bottom of ICARUS TPCs for ν_μ (*left*) and ν_e (*right*). *Middle* and *bottom* panels show the contributions of parent particles responsible for the bulk of the dependence: K^+ and π^+ for ν_μ and K^+ and K^0 for ν_e. Contribution of μ^+ responsible for 1% shift at low ν_e energies is not shown. Plots for the horizontal axes can be found in Fig. C.2.

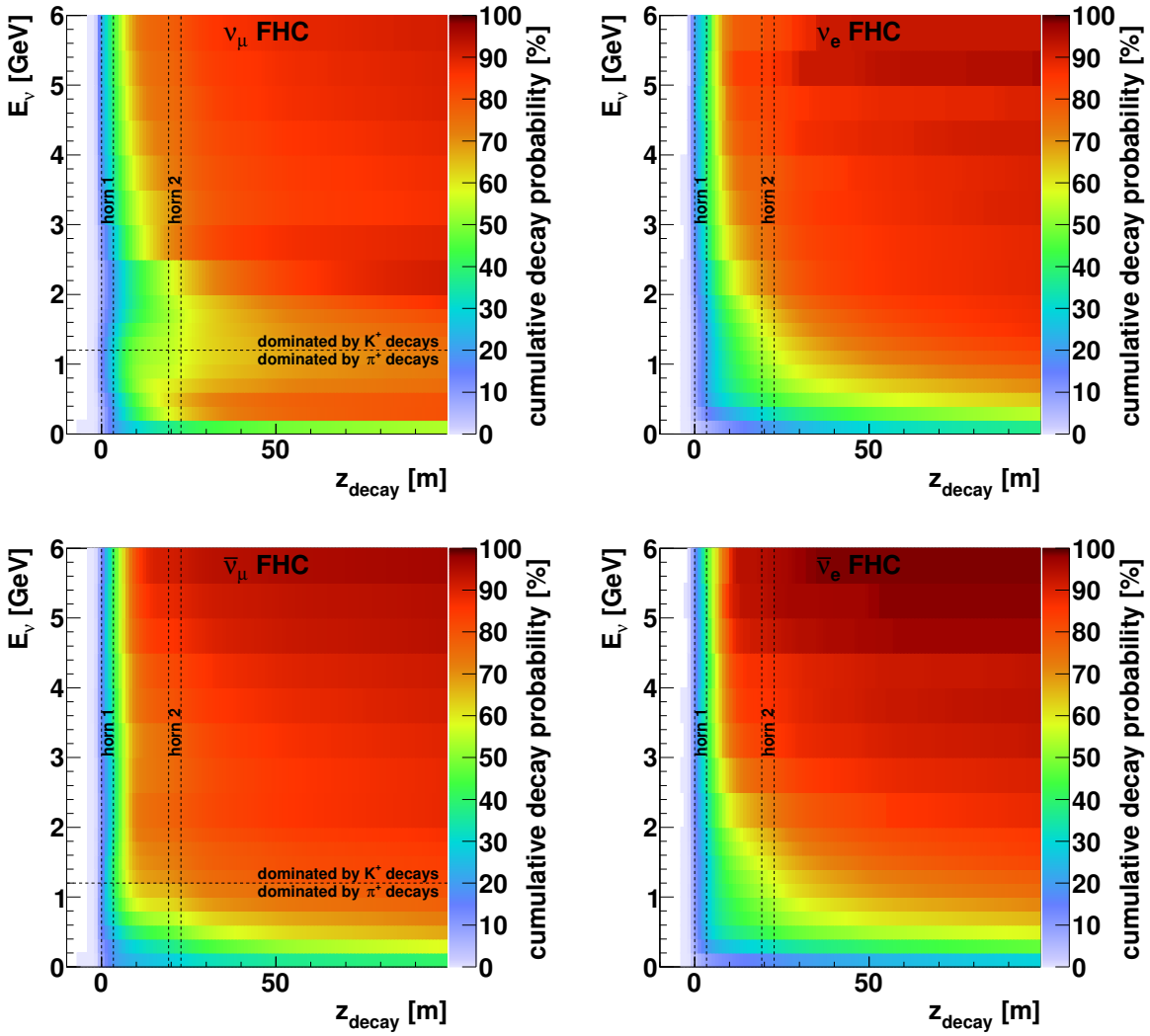

Figure 3.4: Cumulative probability for a parent of a neutrino to decay along the beam line for various energy ranges for ν_μ, ν_e (*top left* and *right*) and $\bar{\nu}_\mu$, $\bar{\nu}_e$ (*bottom left* and *right*). Vertical dashed lines mark horn positions. Horizontal dashed lines in ν_e figures separate the low energy neutrinos originating mostly from $\pi^\pm$ decays and high energy ones originating from $K^\pm$ decays. RHC plots can be found in Fig. C.3

re-interact with the target and/or surrounding materials. The secondary produced particles may themselves also interact multiple times, before eventually decaying to a neutrino. The primary proton can also pass through the target or deflect out of the target and interact with other materials, as well.

To quantify these phenomena the *number of interactions per neutrino*, $\langle \mathcal{N} \rangle$, was studied (as was done for a variety of PPFX studies, e.g., Refs. [11, 12]). $\langle \mathcal{N} \rangle$ is defined as the average number of interactions in the interaction chain which lead to production of the particle that eventually decays to the neutrino. This includes the primary proton interaction, along with a set of consecutive interactions that led to the direct neutrino

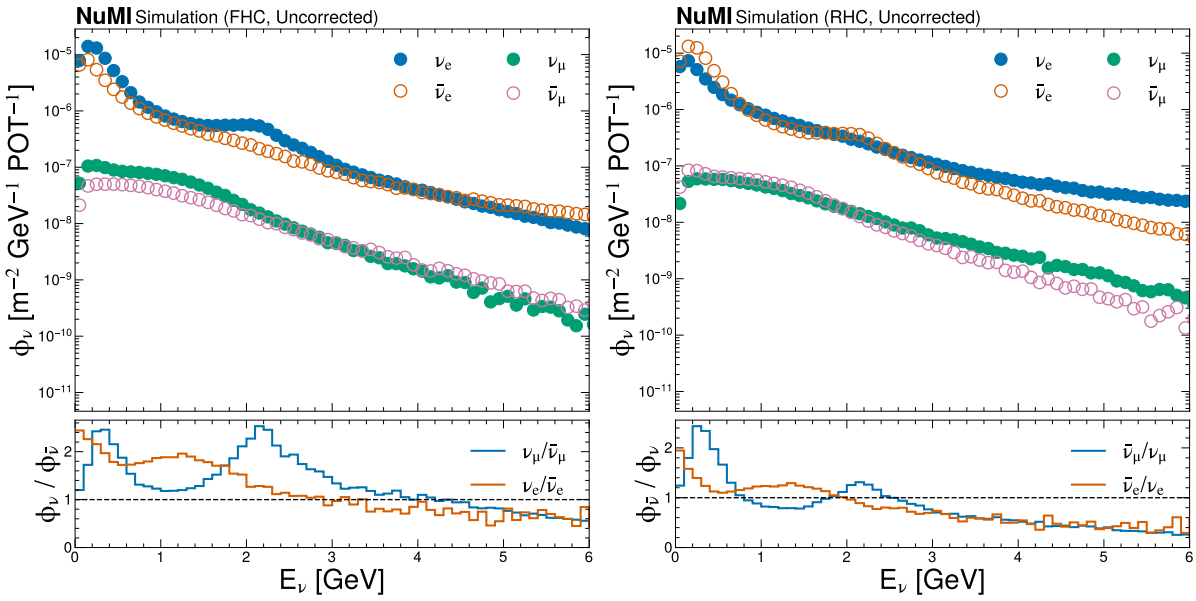

Figure 3.5: NuMI beam flux in ICARUS for forward (*left*) and reverse (*right*) horn current.

parent particle. By this definition, the total number of interactions is greater than or equal to one.

Figure 3.6 shows that the average number of interactions at 5.75° off axis (in ICARUS) is ∼50% larger than on axis (MINERνA location was used to calculate the on-axis flux in this and the subsequent plots in this note). The uncertainties of hadron interaction models will thus have a larger impact on the flux prediction in ICARUS. Figure 3.7 shows the number of interactions on the various nuclei that make up the target chase and decay pipe. In comparison to on-axis flux, there is a greater number of interactions on carbon, and there is also a significant fraction of interactions on other targets (∼0.4 on iron and ∼0.25 on aluminum). These non-carbon interactions are negligible on axis, with the exception of the highly suppressed wrong-sign components.

Figure 3.8 visualizes spacial distribution of the hadronic interactions. Black points represent the positions of interactions, and the histograms show the number of interactions on each target in slices of z position along the beam axis. The number of interactions on aluminum, shown in green, occur primarily on the two aluminum horns. Interactions on iron are distributed in structural components of the target hall and broadly along the steel of the decay pipe.

Figure 3.9 shows the identity of the projectiles and targets participating in hadron interactions. The leading contributions to $\langle \mathcal{N} \rangle$ are from p+C, then p+Fe, and p+Al interactions. There are also non-negligible contributions at the ∼0.1 level from $\pi^\pm$ on C, Fe and Al, and n+C and n+Fe interactions. Interactions of n+Al, as well as charged and neutral kaons are on the level of ∼0.01–0.04. Other target nuclei, not listed separately, include helium, oxygen, and nitrogen. In the on-axis flux, p+C, n+C and π^++C account for almost all interactions, with only a few other channels contributing ∼0.01–0.02 interactions per neutrino.

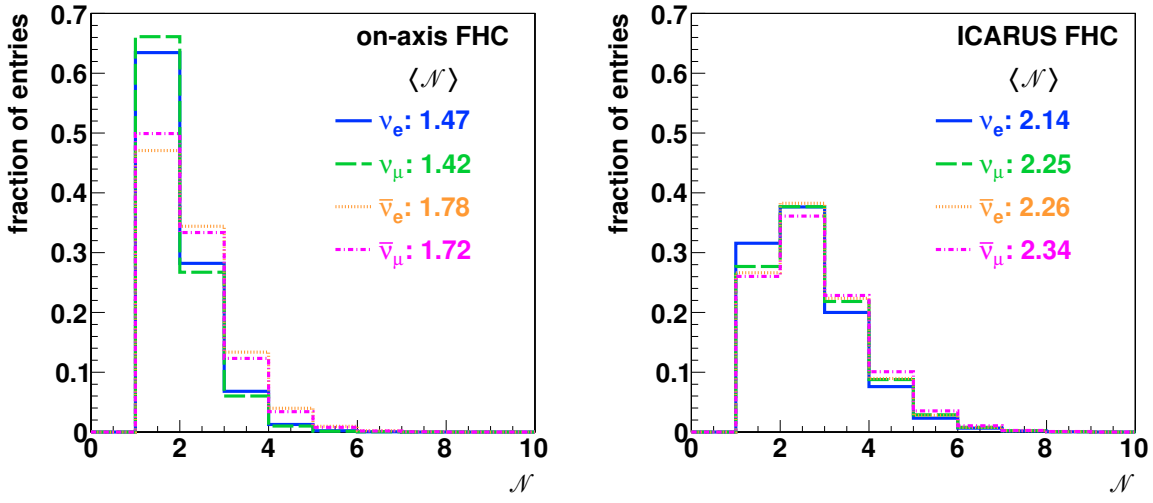

Figure 3.6: Distribution of number of interactions in the target and other material leading to production of a particle which decays to a neutrino produced on-axis (*left*) and going to ICARUS (*right*). Only neutrinos with $E_\nu > 400\,\text{MeV}$ are plotted. The area of the histograms is normalized to unity. The legend shows the average number $\langle \mathcal{N} \rangle$ for each neutrino type.

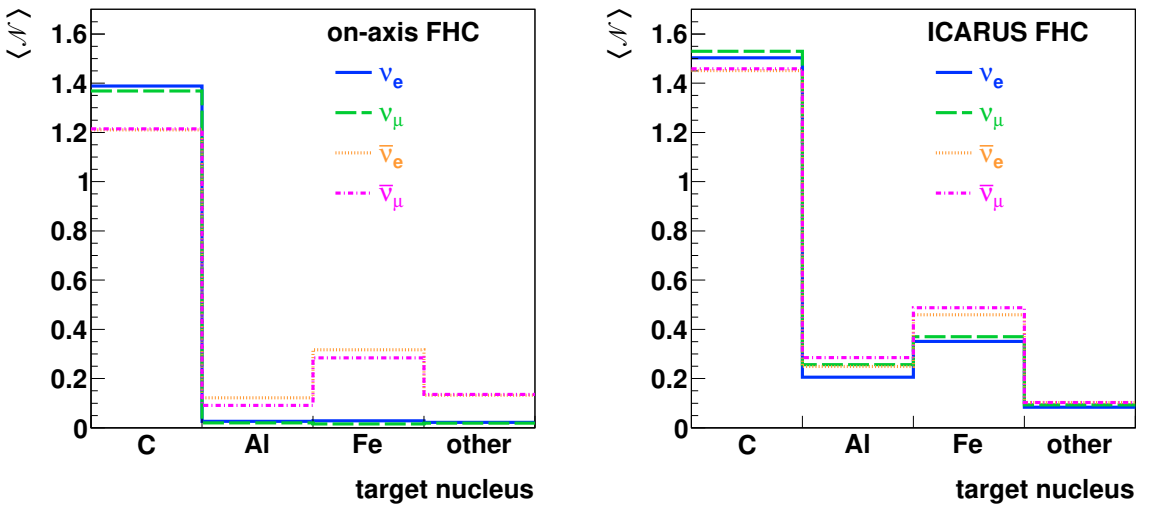

Figure 3.7: Distribution of the average number of interactions $\langle \mathcal{N} \rangle$ on various nuclei leading to production of a particle which decays to a neutrino produced on-axis (*left*) and going to ICARUS (*right*). Only neutrinos with $E_\nu > 400\,\text{MeV}$ are plotted.

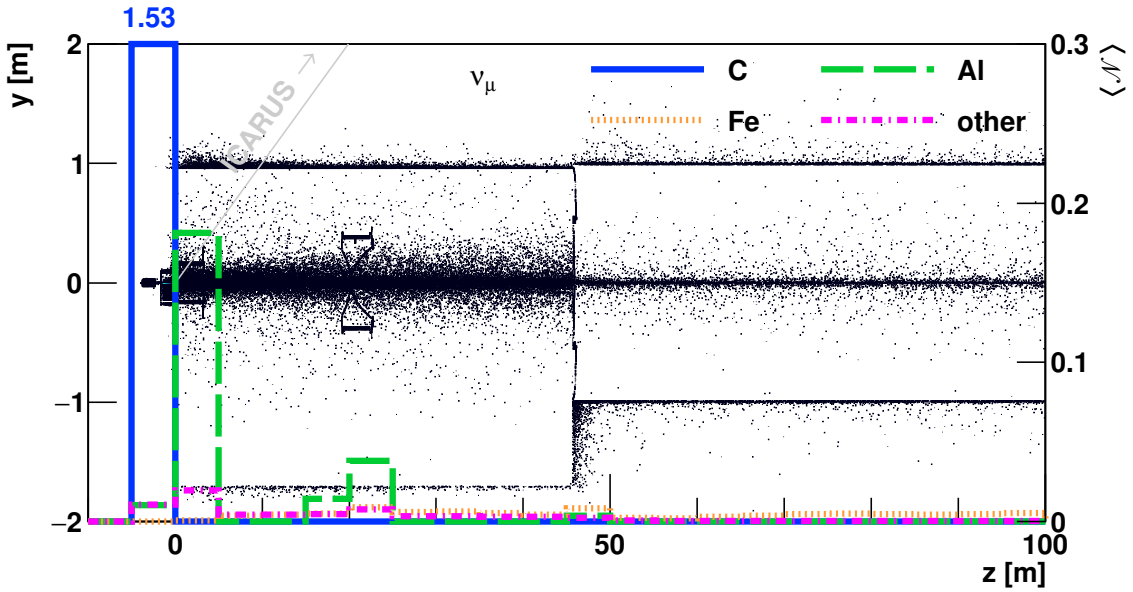

Figure 3.8: Distribution of the position of the last hadronic interaction before decay to ν_μ in the target region. For clarity, only a vertical strip of $|x| < 0.5$ cm is shown. Note, the horizontal and vertical axes are scaled differently. The slanted gray line shows the straight line from the NuMI origin to the center of ICARUS (5.74° in y–z plane). The overlaid histogram shows the average number of interactions (right axis). The vertical axis is truncated as the contribution of interactions on the carbon target (solid blue line) much larger than on the other materials.

Figure 3.10 shows the contributions of hadron interactions to the NuMI flux in ICARUS broken down according to projectile type, projectile momentum, target type and the eventual neutrino flavor. There is a very large contributions from proton interactions at and near 120 GeV/c, the incoming proton beam momentum. The integrated contributions at lower momenta are significant as well: interactions of protons and neutrons at 10–80 GeV/c and kaons and charged pions at 5–40 GeV/c.

3.5 Horn Strips Modelling

The geometrical model of the NuMI beamline was optimized for the on-axis experiments, which determined the level of detail for modelling various beamline components and structural elements. In particular, strips delivering current to the horn magnets appear to be missing from the model.

The fraction of hadrons that pass through various regions of the horns was estimated and is shown in Fig. 3.11. This provides an upper estimate of the fraction of neutrinos which may be affected by interactions with the current strips. It reaches 20% for Horn 1, and several percent for Horn 2. Only a small fraction of these hadrons will actually interact, so the impact on the flux is expected to be small. Note that the simulated geometry has been updated to account for upgrades to a MW beam configuration. Any

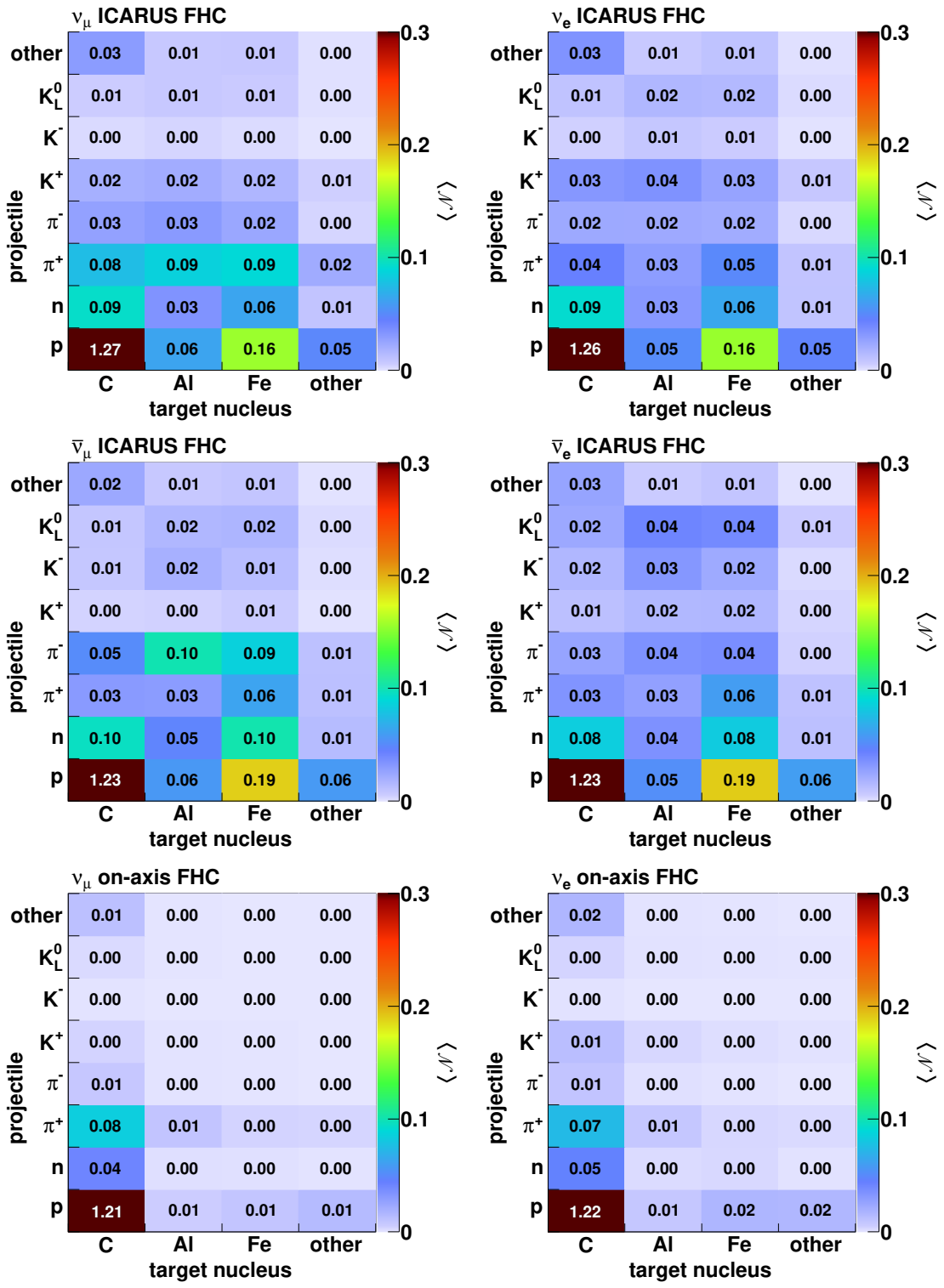

Figure 3.9: Distribution of the average number of interactions $\langle \mathcal{N} \rangle$ of various projectiles on various nuclei leading to production of a particle which decays to a neutrino going to ICARUS (*four top panels*) and produced on-axis (*two bottom panels*). Only neutrinos with $E_\nu > 400\,\text{MeV}$ are plotted. Additional plots can be found in Fig. C.4.

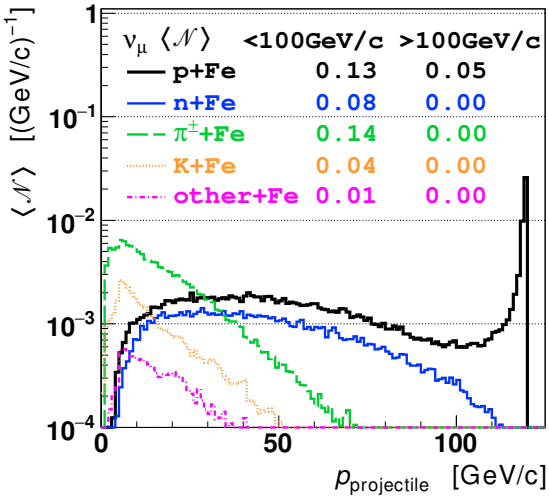

Figure 3.10: Example of momentum distributions of interactions on iron contributing to the NuMI flux in ICARUS. Colored lines distinguish hadron projectiles: p (thick black), n (solid blue), $\pi^\pm$ (dashed green), K (dotted orange) and other (dash-dotted magenta). Legend shows the number of interactions per neutrino ($\langle\mathcal{N}\rangle$) integrated separately below and above 100 GeV/c. Only neutrinos with $E_\nu > 400$ MeV are plotted. Full set of plots for all neutrinos and other target types (C, Al, other) can be found in Fig. C.5.

new large production simulation runs should include this new geometry and will have the ability to add the strip lines.)

3.6 Decay Location

The previous Section focused on the hadronic interaction chains that led to the hadrons, which produced neutrinos of interest. The focus of this Section will shift to the various processes of neutrino production from these neutrino parent hadrons and their impact on the flux in ICARUS. Table 3.2 lists the primary decay channels for neutrino production in NuMI.

Figure 3.12 compares the position along the beam axis for hadron decays that produce neutrinos going to ICARUS and on-axis, which is centered just 0.8 m away from NuMI axis, 1 km downstream from the target. The on-axis flux originates from decays along the whole length of the decay pipe. The ν_μ are produced almost exclusively by π^+ in the beam pipe. The plot shows also a tiny contribution of low momentum, unfocused π^+ producing neutrinos below 1 GeV in the target area. In the first tens of meters after the target, ν_e are produced in decays of relatively short living K^+ and K^0, while the bulk of ν_e comes from μ^- decays in the downstream part of the decay pipe. In contrast, the majority of ν_e and ν_μ travelling to ICARUS originate from decays in the first tens of meters after the target. There is also a small contribution from decays in the beam dump, mostly at $E_\nu < 400$ MeV.

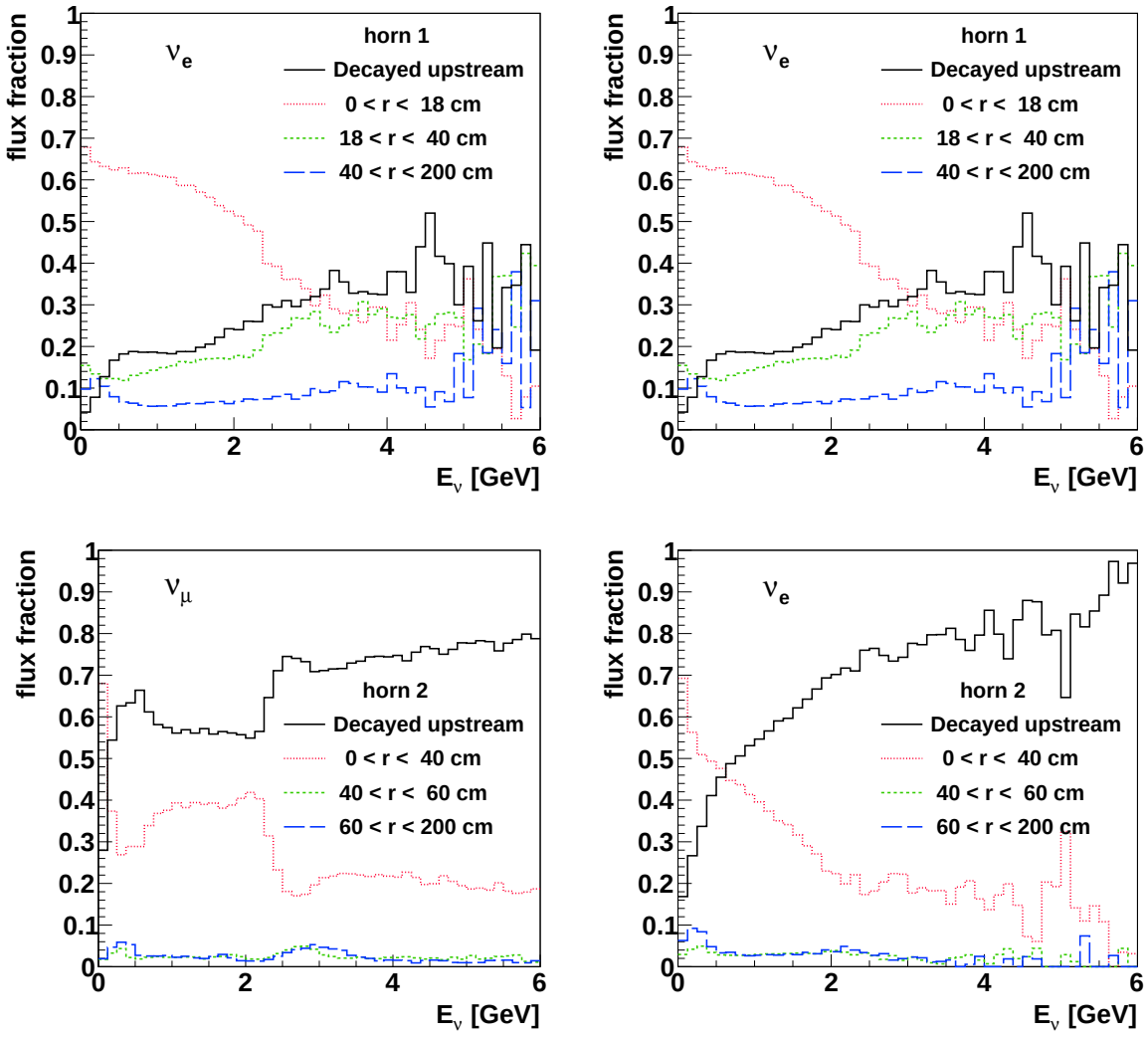

Figure 3.11: Fraction of neutrinos with ancestor hadrons passing through the plane perpendicular to the downstream face of Horns 1 (z = 3.40 m, *top* panels) and 2 (z = 22.80 m, *bottom*), for various distances from the beam axis for ν_μ (*left*) and ν_e (*right*), as a function of energy of the neutrino in ICARUS. Dotted red line shows hadrons passing inside the horns; short-dashed green line roughly represents the region where some hadrons may interact with current strips; long-dashed blue line shows hadrons farther away from the beam axis, less likely to hit the strips; solid black line shows hadrons which decayed before reaching the region in question.

Table 3.2: Properties of decays to neutrinos in NuMI beamline. For three-body decays, the neutrino energy distribution is continuous, ranging from 0 up to the listed value.

parent	decay products	branching ratio	E_ν^{CMS} [MeV]
K^+	$\to \mu^+ + \nu_\mu$	63.6%	235.5
	$\to \pi^0 + e^+ + \nu_e$	5.1%	< 228
	$\to \pi^0 + \mu^+ + \nu_\mu$	3.4%	< 188
K_L^0	$\to \pi^- + e^+ + \nu_e$	40.6%	< 229
	$\to \pi^- + \mu^+ + \nu_\mu$	27.0%	< 188
π^+	$\to \mu^+ + \nu_\mu$	99.99%	29.8
μ^+	$\to e^+ + \nu_e + \bar{\nu}_\mu$	~100%	< 53

Figure 3.13 shows the angle (w.r.t. the NuMI beam axis) of the hadrons decaying to neutrinos. The energy of the ν_μ from $\pi^\pm$ decays is only 29.8 MeV in the center of mass system. The neutrinos will therefore have relatively little transverse momentum with respect to the parent particle. In order to produce ν_μ above 1 GeV along the direction of the ICARUS detector, the pions must be moving in the direction of ICARUS, resulting in a narrow distribution of the pion angles, centered at the ICARUS direction, 5.75°. The angular distribution of low momentum pions producing neutrinos reaching ICARUS is much wider, but these neutrinos have very low energies. In turn, kaons have many decays modes, with neutrino energies exceeding 200 MeV in some of them. ICARUS accepts neutrinos coming from decays of kaons aligned with the beam axis, or even moving downwards, up to 2–3 GeV.

Figure 3.14 shows the distance travelled by neutrinos (baseline) from the decay point to the detector. As the transverse dimensions of the target hall and the decay pipe are relatively small, the baseline is strongly correlated with the decay position along the z axis, and the angle between the neutrino trajectory and the beam axis, as shown in Fig. 3.15. With the highly constrained relationship between baseline and angle, analyzers should be able to directly relate the reconstructed neutrino angle to the neutrino baseline. The resolution of the reconstructed angle will likely contribute more to the baseline uncertainty than the baseline-angle correspondence shown in Fig. 3.15.

The distribution of angle with respect to the beam axis of neutrinos coming to ICARUS is shown in Fig. 3.16. While the spread of the angles is almost 50°, the vast majority of neutrinos are in the 6–10° range, originating from the vicinity of the target. The higher angle contribution decreases quickly with neutrino energy. In particular, the peak at 50° from the beam dump is significant only for $E_\nu < 400$ MeV. A tail for ν_e above 50° originates from decays of μ^+ penetrating the absorber at the end of the

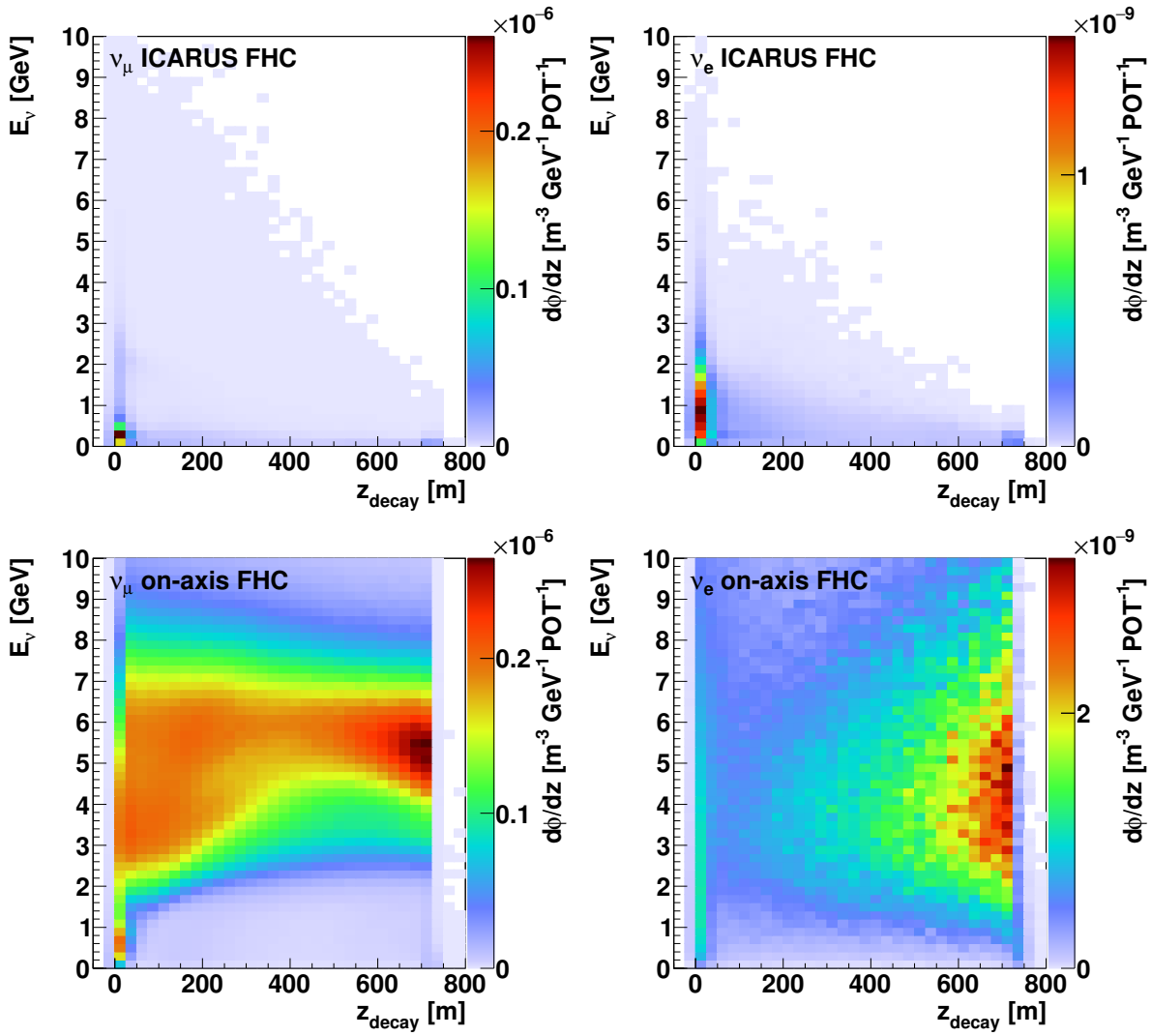

Figure 3.12: Distribution of neutrino energy as a function of the position along the NuMI beam line of decays to ν_μ (*left*) and ν_e (*right*) going to ICARUS (*top*) and on-axis (*bottom*). The target is at $z \approx 0$ and the beam dump at $z \approx 725$ m. Plots for antineutrinos found in Fig. C.6.

decay pipe, and the rock behind it. The same decays produce $\bar{\nu}_\mu$ above 50° (not shown). In Forward Horn Current, there is no such tail for ν_μ, as the horns deflect π^-, which would decay to μ^- and then ν_μ and $\bar{\nu}_e$. Overall there is strong dependence between the neutrino energy and the angular ranges of the incoming neutrinos and almost all neutrinos above 1 GeV come from the region near the target and horns, while low energy neutrinos have a much wider spectrum or origination.

Putting this all together, the neutrino production of NuMI at ICARUS can be summarized. The following processes dominate ν_μ production:

- Very low momentum μ^+ decaying in the beam dump (baseline < 100 m). As shown in Fig. 3.16, this μ contribution is much lower than for ν_e.

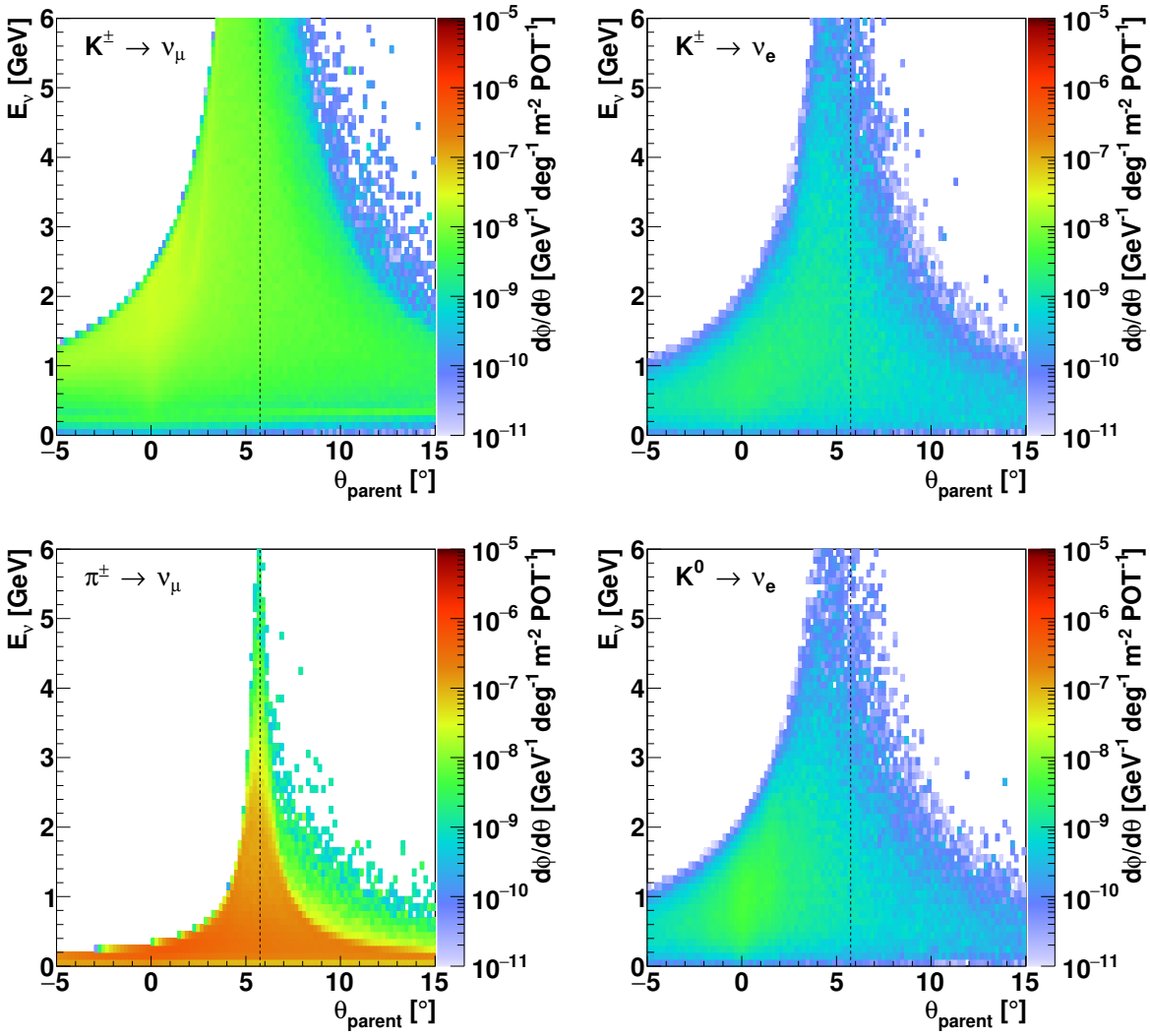

Figure 3.13: Distribution of angle projected onto the plane connecting the beam axis and ICARUS detector, of the momentum vector at the decay point of the most common parents of neutrinos reaching ICARUS: K^+ decaying to ν_μ (*top left*), ν_e (*top right*), π^+ decaying to ν_μ (*bottom left*) and K^0 decaying to ν_e (*bottom right*). The dashed vertical line shows the ICARUS detector location from the NuMI origin.

- Very low momentum ($p \lesssim 1$ GeV/c), short trajectory, tertiary π^+ produced in the beam dump and along the decay pipe (low E_ν, baseline > 100 m).
- Low momentum (several GeV/c) π^+ produced in the target and decaying in the beam pipe (baseline < 800 m, $0.5 < E_\nu < 1$ GeV). As the neutrino energy in pion decay is low, only low momentum pions moving along the beam axis can produce neutrinos going to ICARUS. However, pion survival distance decreases with decreasing momentum. At 1 GeV/c, 85% pions decays before 100 m. This limits production of neutrinos below 0.5 GeV in the decay pipe, and makes this contribution diminish after ~150 m from the target.

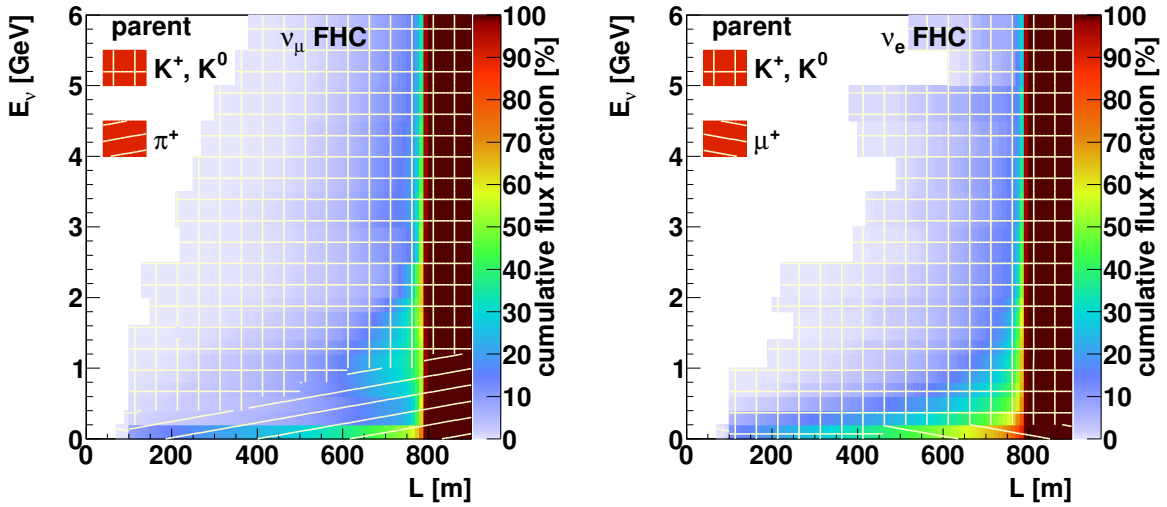

Figure 3.14: Distribution of neutrino energy as a function of neutrino flight path from the decay point to the geometrical center of ICARUS, for ν_μ (*left*) and ν_e (*right*). The plots are cumulative along the horizontal axis, and normalized to 100% in each E_ν bin. The baseline of 100 m corresponds to decays in the beam dump, and 800 m to the target area. The hatched areas show the identity of neutrino parent particles contributing the most to the cumulative distribution in those bins. Corresponding antineutrino plots can be found in Fig. C.7.

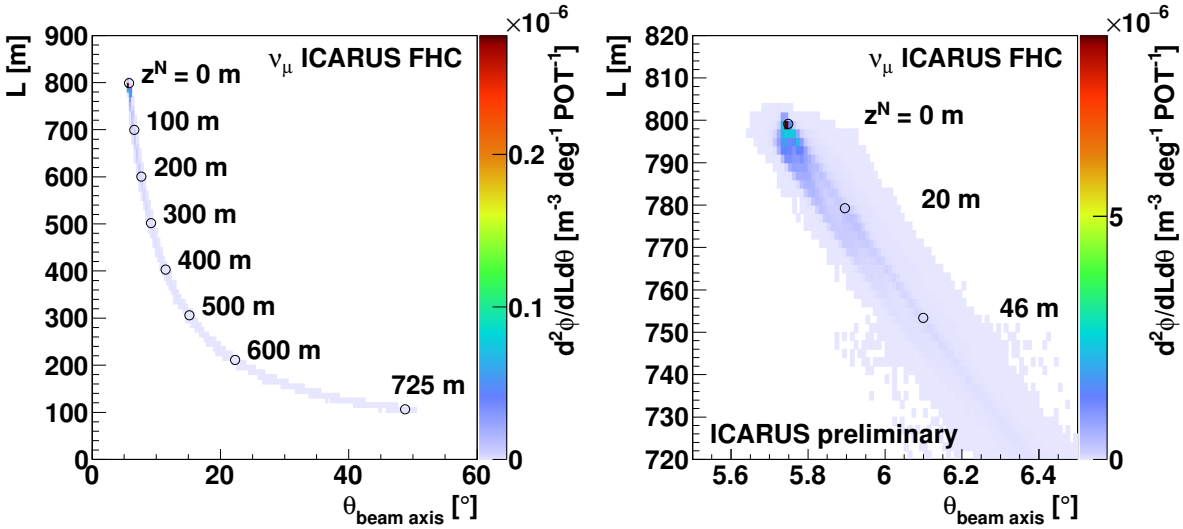

Figure 3.15: Distribution of baseline as a function of the angle between neutrino trajectory and NuMI beam axis. Both plots show the same distribution for ν_μ, the *left* one is zoomed on the decays near the target. Open circles mark positions along the NuMI axis, labeled as distance z^N from the target, in particular 0 m: Horn 1, 20 m: Horn 2, 46 m: window between the target area and the decay pipe and 725 m: end of the decay pipe. Only neutrinos with $E_\nu > 400$ MeV are shown.

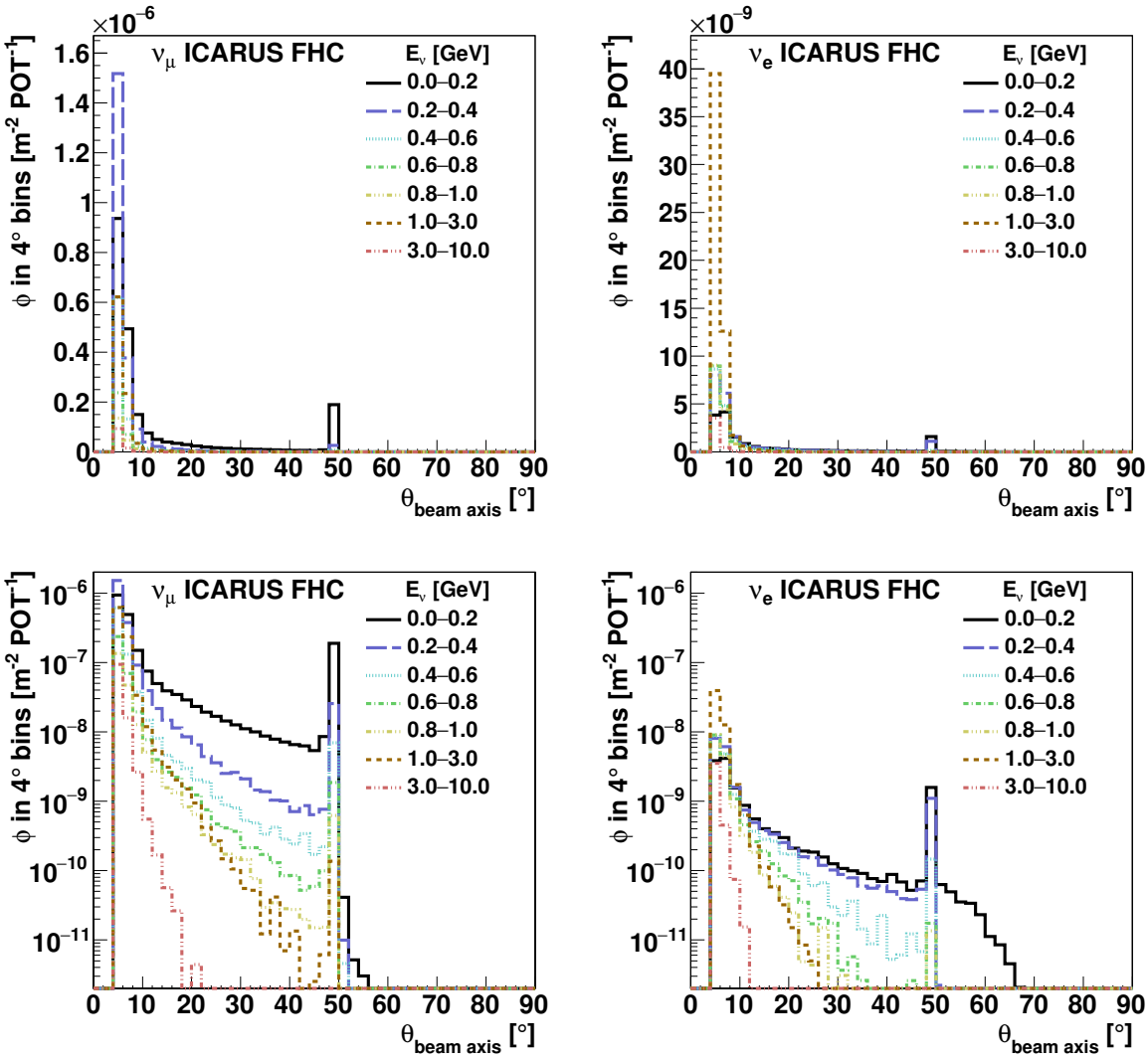

Figure 3.16: Distribution of neutrino angle w.r.t. the NuMI beam axis for ν_μ (*left)* and ν_e (*right*) in various energy ranges. The *bottom* plots show the same data as the *top* but in the logarithmic scale in order to better represent the large angle region. Full set of plots for antineutrinos and RHC can be found in Fig. C.8.

- Low momentum K^+ produced in the target and decaying in the beam pipe at baseline < 800 m and $1 < E_\nu < 2$ GeV. Kaons are affected by similar constraints as pions, however, kaon decay energy is larger. In the decay pipe, kaons of larger momentum can produce neutrinos going to ICARUS. However, as the pion contribution grows rapidly below $E_\nu = 1$ GeV, fractional kaon contribution becomes very low in this region.
- Decays of large momentum K^+ and π^+ in the target area (baseline > 800 m). For a large momentum kaon or pion to produce a neutrino going to ICARUS, it must travel in the direction of the detector. As shown in Fig. 3.8, such mesons hit the ceiling of the decay pipe already after passing 10 m. Only 2.5% of charged kaons at 10 GeV/c decay before passing 10 m. This limits the high energy neutrino flux

from kaon decays. As the pion lifetime is much longer than that of a kaon, their contribution rapidly diminishes for neutrinos above 1 GeV.

The following processes dominate ν_e production:

- Very low momentum μ^+ decaying along the beam pipe ($E_\nu < 0.2\,\text{GeV}$, baseline < 800 m), and in the beam dump (baseline < 100 m).
- Very low momentum, show trajectory, tertiary kaons decaying in the decay pipe ($E_\nu < 0.2\,\text{GeV}$, baseline < 800 m). One should note that kaons can decay to both ν_e and ν_μ. However, ν_μ production below 1 GeV is strongly dominated by π^+, which is why kaon contribute very little to the corresponding region of the ν_μ distribution.
- Low momentum (several GeV/c) K^+ produced in the target and decaying in the beam pipe (baseline < 800 m, $E_\nu < 1\,\text{GeV}$). As explained in the previous point, in the ν_μ distribution the corresponding kaon contribution is much lower than the π^+ one.
- Kaons decaying in the target area (baseline > 800 m). The contribution of K^+ and K^0_L is similar in the whole neutrino energy range, with slightly more K^0_L at $E_\nu > 2\,\text{GeV}$.

4 NUMI NEUTRINO FLUX PREDICTION AND UNCERTAINTIES

This section contains a discussion of the NuMI flux prediction, as well as its related uncertainties, calculated from simulated data prepared as described in Sec. 2. The results of this analysis have been merged into SBNSoftware/sbndata[27], and the code to reproduce it is currently published, and publicly available, on GitHub [28]. The inputs used in this section are as follows.

(i) The nominal flux used in the previous Sections.
(ii) The PPFX central value flux produced by the PPFX reweighting procedure discussed in Sec.2.4
(iii) The set of $N = 100$ PPFX universes created using the procedure described in Sec. 2.4.
(iv) A set of alternate flux simulations created using alternate beamline configurations.

Input (iv) requires fully regenerated flux files that are statistically independent of each other. Each file has a single parameter of the flux simulation adjusted by an amount recommended by the designers and operators of the NuMI beamline complex.

4.1 Methods for Estimating and Combining Uncertainties

4.1.1 Methods to Extract the Hadron Production Corrections and Uncertainties from PPFX

PPFX was used to perform hadronic interaction reweighting on the input Monte Carlo simulation, which produced a set of flux universes varied according to the underlying hadron interaction probability model. The distribution of flux universes was studied and used to calculate the NuMI flux prediction as well as the systematic uncertainty due to hadron interactions. After verifying that the universes were distributed normally (see Sec. 4.1.5), the predicted flux in each bin of neutrino flavor and energy was calculated as the mean flux across N PPFX universes:

$$\overline{\phi}_i = \frac{1}{N}\sum_{k=1}^{N}\phi_i^k, \tag{4.1}$$

where $\overline{\phi}_i$ is the mean flux in bin i, and ϕ_i^k is the neutrino flux in bin i and universe k. Similarly, the systematic uncertainty due to hadron production modelling in a particular bin, σ_i, was calculated as the width of the flux universe distribution:

$$\sigma_i = \sqrt{\frac{\sum_{k=1}^{N}\left(\phi_i^k - \overline{\phi}_i\right)^2}{N-1}}. \tag{4.2}$$

To quantify the impact of the hadron interaction reweighting across the entire neutrino energy-flavor space, a covariance matrix, $\mathbf{V}_{\text{hp}}$, whose entries are the covariance between energy-flavor bins i and j:

$$\mathbf{V}_{\text{hp}} = \left[\text{cov}_{\phi_i\phi_j}\right], \tag{4.3}$$

$$\text{cov}_{\phi_i\phi_j} = \frac{1}{N-1}\sum_{k=1}^{N}\frac{\left(\phi_i^k - \overline{\phi}_i\right)\left(\phi_j^k - \overline{\phi}_j\right)}{\overline{\phi}_i\overline{\phi}_j}, \tag{4.4}$$

where $\text{cov}_{\phi_i\phi_j}$ is the matrix element corresponding to the covariance between energy-flavor bins, i and j.

A principal component analysis of the total hadron production uncertainty covariance matrix, $\mathbf{V}_{hp}$, was performed to extract its eigenvalues, λ, and normalized eigenvectors, $\hat{\mathbf{u}}$.

$$\mathbf{V}_{hp} = \begin{bmatrix}\hat{\mathbf{u}}_1 & \cdots & \hat{\mathbf{u}}_n\end{bmatrix}\begin{bmatrix}\lambda_1 & \cdots & 0 & 0\\ \vdots & \ddots & 0 & 0\\ 0 & \cdots & \lambda_{n-1} & 0\\ 0 & \cdots & 0 & \lambda_n\end{bmatrix}\begin{bmatrix}\hat{\mathbf{u}}_1 & \cdots & \hat{\mathbf{u}}_n\end{bmatrix}^{-1} \tag{4.5}$$

The eigenvalue and eigenvector pairs were sorted in order of decreasing eigenvalue. The eigenvectors are a linear combination of energy-flavor bins from the covariance matrix, pointing in directions of maximal variance. Eigenvalues, λ_k, expressed as a fraction of the sum of all n eigenvalues, g_n, describe the fraction of the total variance associated with its corresponding eigenvector. It is possible to use these quantities to identify and reduce the effects of degenerate parameters and statistical noise by selecting a threshold for the fractional eigenvalue, α, below which the eigenvalue-vector pairs are removed, and the covariance matrix is reconstructed.

$$g_n = \sum_{k=1}^{n}\lambda_k \tag{4.6}$$

$$\left(\frac{\lambda_k}{g_n} < \alpha \rightarrow \lambda_k = 0\right) \forall\ k \leq n \tag{4.7}$$

For this analysis, all positive, real eigenvalues were kept, while negative eigenvalues corresponding to statistical noise were discarded. A modified covariance matrix, $\mathbf{V}'_{PC}$, is constructed using the remaining eigenvalues.

$$\mathbf{V}'_{hp} = \begin{bmatrix}\hat{\mathbf{u}}_1 & \cdots & \hat{\mathbf{u}}_n\end{bmatrix}\begin{bmatrix}\lambda_1 & \cdots & 0 & 0\\ \vdots & \ddots & 0 & 0\\ 0 & \cdots & 0 & 0\\ 0 & \cdots & 0 & 0\end{bmatrix}\begin{bmatrix}\hat{\mathbf{u}}_1 & \cdots & \hat{\mathbf{u}}_n\end{bmatrix}^{-1} \tag{4.8}$$

4.1.2 Methods to Estimate the Uncertainties from Beamline Mismodeling and Variations in Operating Conditions

To estimate the uncertainty due to focusing of the NuMI beam, statistically independent samples of the neutrino flux were produced according to the parameterization specified

in the NOνA third analysis [23]. Appendix J contains a complete description of each sample. Additional datasets to study the impact of Earth's magnetic field were also considered. The effect was found to be consistent with the statistical uncertainties; thus it was not to include it in the flux systematic uncertainties. Details of this analysis can be found in Appendix D.

The difference in flux between each Run 8 – 32 and the nominal sample (Run 15) was calculated, and a covariance matrix was constructed according to eq. 4.4, where n is taken to be $n \in \{\phi_i^+, \phi_i^{\text{nom}}, \phi_i^-\}$ and $\overline{\phi}_i \to \phi_i^{\text{nom}}$. ϕ_i^{nom} represents the nominal flux in i^{th} bin of neutrino energy and flavor, and $\phi_i^{\pm}$ is the flux for the $\pm 1\sigma$ variant. It was discovered that large statistical fluctuations were present in the samples, hindering interpretation of systematic effects. To compensate, smoothing of the statistical fluctuations was accomplished by applying a median filter, implemented in the ROOT function `TH1::Smooth()` [29], to the fractional flux differences, eq. 4.9.

$$\frac{\Delta\phi_k^i}{\phi_{nom}^i} = \frac{\left(\phi_k^i - \phi_{nom}^i\right)}{\phi_{nom}^i} \tag{4.9}$$

A smoothed version of the absolute flux differences was calculated by multiplying through by the nominal flux. Smoothed and non-smoothed absolute flux differences were compared against the statistical uncertainty of the nominal sample to discriminate true systematic effects. Additionally, Run 30, i.e., a constantly applied magnetic field in the decay medium, is used as a benchmarking sample. As demonstrated in Sec. 3.6, decays of neutrino parent particles occur before the decay pipe, therefore observed effects in Run 30 are purely statistical in origin. Beamline samples or portions thereof that did not meet the following criteria were removed from the final covariance calculation:

(i) $\Delta\phi_k \geq \sigma_{stat}$ (see (2.3))
(ii) $\Delta\phi_k$ exhibits similar trends between smoothed and non-smoothed spectra
(iii) Minimal presence of large statistical fluctuations
(iv) Dissimilar from Run 30

Examples of samples which did and did not meet the criteria are shown in figures 4.1a and 4.1b, respectively. The remaining spectra have been included in Appendix K. Finally, covariance matrices were calculated once again using the samples that passed the selection process. The total systematic effect due to beam focusing is calculated from the addition of each individual covariance matrix, $\mathbf{V}_x$, to yield a total:

$$\mathbf{V}_{\text{beam}} = \sum \mathbf{V}_x. \tag{4.10}$$

4.1.3 Combining Uncertainties From All Sources

Finally, the total uncertainty on the flux prediction is fully represented by adding together the hadron covariance matrix, $\mathbf{V}_{\text{hp}}$, the beam focusing matrix, $\mathbf{V}_{\text{beam}}$, a covariance matrix characterizing the differences between the older and updated beam

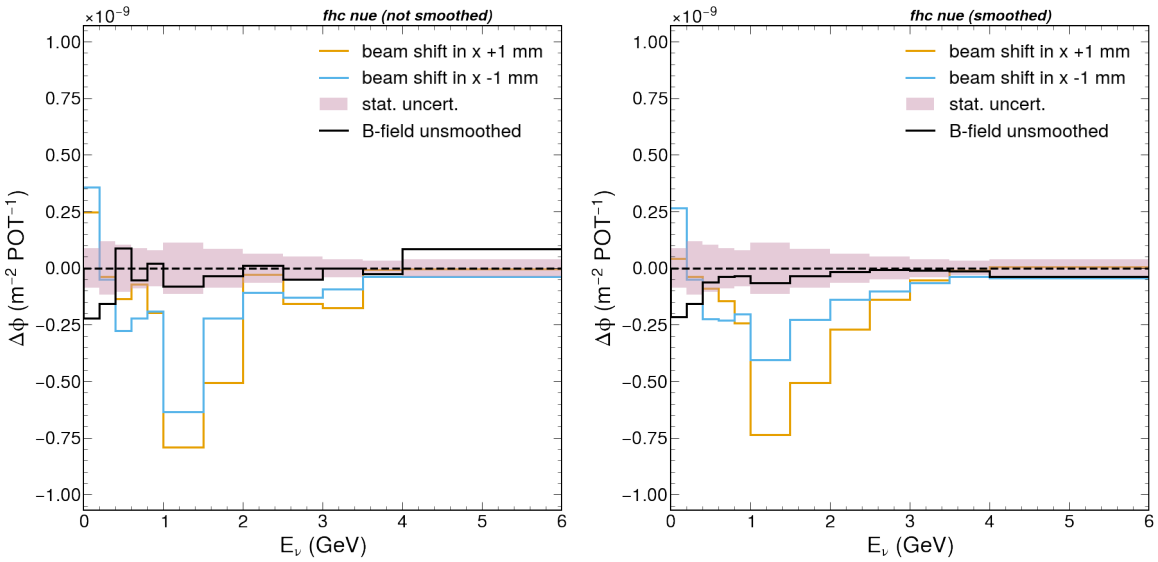

(a) The effect of shifting the x-position of the NuMI beam is significant between $0.6 \leq E_\nu \leq 3.6$GeV and is present between both smoothed and non-smoothed spectra. Therefore, this sample was kept for the analysis.

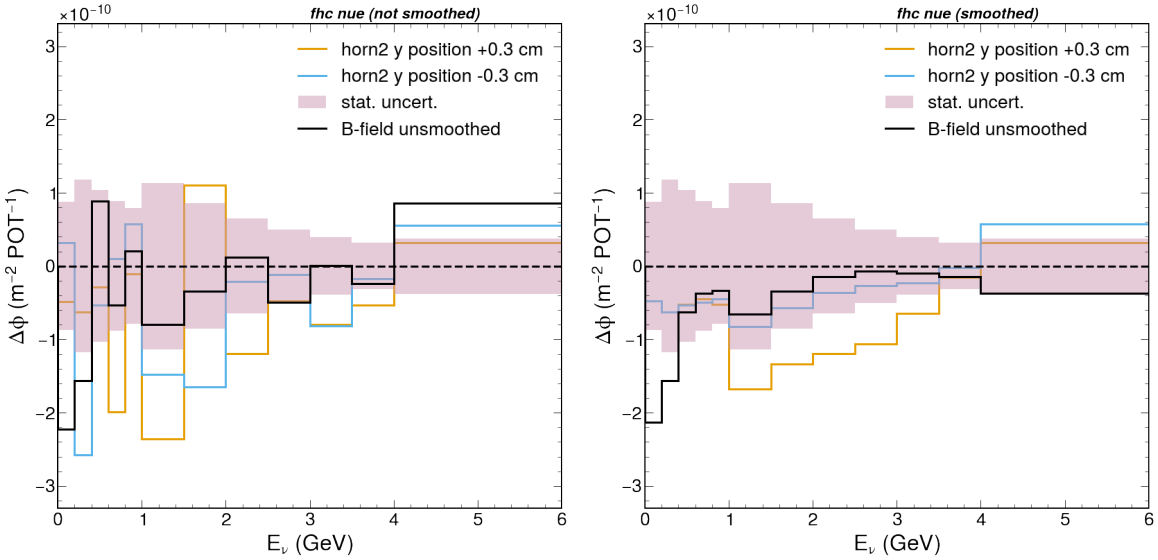

(b) Y-positioning of NuMI's second horn was excluded due to the presence of large statistical fluctuations, especially for E_ν up to 2 GeV.

Figure 4.1: Smoothed and non-smoothed flux comparison for forward horn current ν_e, demonstrating examples of samples selected for inclusion in (4.1a) and rejection from (4.1b) this analysis.

geometry, $\mathbf{V}_{\text{geom}}$[2], and a diagonal matrix containing the statistical uncertainty on each neutrino energy-flavor bin, Σ_{stat}.

$$\mathbf{V}_{\text{tot}} = \mathbf{V}_{\text{hp}} + \mathbf{V}_{\text{beam}} + \mathbf{V}_{\text{geom}} + \Sigma_{\text{stat}}. \tag{4.11}$$

Since the variances are being added, this is equivalent to a quadrature sum of the correlated 1σ uncertainties. The full covariance matrix is used to calculate the total uncertainty on the flux for various combinations and ratios of the four neutrino modes according to the formula described in Appendix E. Both the total uncertainties and each contribution are included in the analysis data products so that analyzers can use and manipulate the components as needed, or use the total for simpler use cases.

4.1.4 Flux Binning Scheme

By default, PPFX output flux histograms with 100 MeV-wide bins spanning 0–20 GeV of neutrino energy. A lower-resolution, variable bin scheme was adopted to suppress the large statistical fluctuations present in the nominal flux (Run 15). The fluctuations are especially noticeable where the total flux is relatively small, e.g., the ν_e and the ν_μ flux in the high-energy tail. Bin widths were chosen to be monotonically increasing, doubling approximately where the bin-to-bin flux dropped off by a factor of 2 or more. Care was taken to avoid creating large bins in regions where the flux rapidly increases or decreases. The binning scheme is outlined in Table 4.1, and will be used for plots binned in E_ν for the remainder of the Note. Additionally, Table 4.2 details how these bins are organized within covariance matrices presented in this note.

4.1.5 Validating the Suitability of the Chosen Number of PPFX Universes

For this analysis, PPFX was configured to generate 100 flux universes. To assess the normality of the distribution of flux universes, a fit to a Gaussian function was applied to a histogram of the universes, for each bin of neutrino energy and flavor. In addition, the Shapiro-Wilk (SW) test and a quantile comparison of the universe distribution with a Gaussian was performed for each bin. An example of one such fit is shown in Fig. 4.2. The least Gaussian E_ν bins were the first and second ($0 < E_\nu < 200$ MeV and $200 < E_\nu < 400$ MeV, respectively) across every neutrino mode. 91% of bins were found to have an SW p-value > 0.05, consistent with a Gaussian structure. Fitting Gaussian functions to the distributions revealed a difference in the estimated mean of less than 1%, on average, across all neutrino modes, an average 7% difference in the distribution width, a mean χ^2/ndf of 0.98, and also followed a linear trend in the quantile comparisons. See Appendix F for results of the normality study in each bin. These findings indicate that the PPFX universes are normally distributed, and therefore the hadron interaction correction to the NuMI flux is accurately represented by the universes' mean, and the systematic uncertainty by the distribution width.

[2]Refer to Sec. 4.2.4 for more details.

Table 4.1: The neutrino energy binning scheme applied to this analysis with the PPFX-corrected NuMI neutrino flux in the corresponding bin. This binning was selected using a heuristic approach in order to enhance energy resolution while simultaneously minimizing the effects of statistical fluctuations present in the flux simulation. *Note that the 12.0–20.0 GeV bin is removed in the case of both ν_e and $\bar{\nu}_e$ spectra, as this bin was consistently found to be empty across both horn operating modes.

		Flux [$m^{-2}GeV^{-1}POT^{-1}$]							
		FHC				RHC			
Bin	Interval [GeV]	ν_e $\times 10^8$	$\bar{\nu}_e$ $\times 10^8$	ν_μ $\times 10^6$	$\bar{\nu}_\mu$ $\times 10^6$	ν_e $\times 10^8$	$\bar{\nu}_e$ $\times 10^8$	ν_μ $\times 10^6$	$\bar{\nu}_\mu$ $\times 10^6$
1	[0.0, 0.2)	1.417	0.595	1.975	1.304	0.667	1.140	1.179	1.842
2	[0.2, 0.4)	1.861	0.877	1.949	0.779	1.049	1.412	0.752	1.848
3	[0.4, 0.6)	1.566	0.871	0.769	0.364	1.022	1.153	0.379	0.714
4	[0.6, 0.8)	1.462	0.820	0.322	0.218	0.937	1.078	0.238	0.285
5	[0.8, 1.0)	1.374	0.727	0.192	0.151	0.833	1.018	0.173	0.157
6	[1.0, 1.5)	2.693	1.383	0.304	0.248	1.590	2.000	0.292	0.230
7	[1.5, 2.0)	1.417	0.833	0.255	0.149	0.969	1.089	0.181	0.171
8	[2.0, 2.5)	0.603	0.483	0.205	0.089	0.578	0.496	0.112	0.134
9	[2.5, 3.0)	0.296	0.283	0.086	0.049	0.347	0.248	0.065	0.057
10	[3.0, 3.5)	0.165	0.169	0.039	0.030	0.224	0.136	0.042	0.027
11	[3.5, 4.0)	0.092	0.114	0.023	0.021	0.147	0.080	0.030	0.017
12	[4.0, 6.0)	0.114	0.155	0.038	0.042	0.238	0.103	0.068	0.026
13	[6.0, 8.0)	0.014	0.023	0.008	0.015	0.037	0.016	0.026	0.006
14	[8.0, 12.0)	0.003	0.005	0.002	0.005	0.007	0.003	0.008	0.002
15*	[12.0, 20.0]	0	0	9.9e-5	3.36e-4	0	0	4.89e-4	7.7e-5

4.2 Flux Uncertainties

4.2.1 PPFX Corrections and Uncertainties

The total corrected flux in each E_ν bin is determined from the mean of the 100 flux universes. Fig. 4.3 shows the flux after PPFX corrections were applied. The breakdown of the flux by neutrino parent particle is also shown to help decipher the impact of the various hadronic interaction channels on the systematic uncertainty.

For each interaction channel described in Sec. 2.4.1, the universes were used to calculate a covariance matrix according to Eq. 4.4. Figure 4.4 shows the total covariance matrix. Boxes along the diagonal represent the covariance for a particular neutrino flavor in a specific running mode. Off-diagonal boxes in the upper-right (RHC) and lower-left (FHC) quadrants give the covariance between flavors in the same running

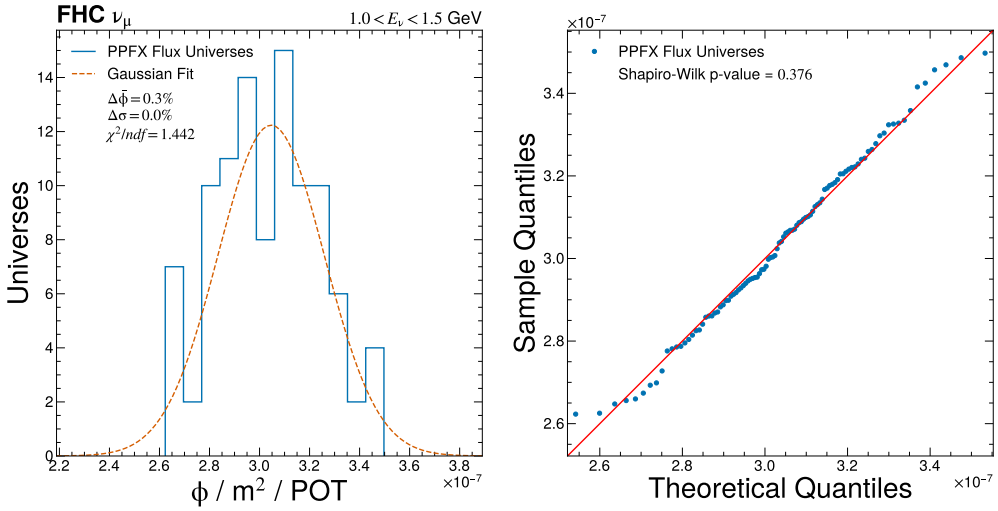

Figure 4.2: An example distribution of muon neutrino PPFX flux universes (blue) in the 1.0–1.5 GeV, demonstrating normal behavior. From the Gaussian fit (left), the mean and width of the distribution are consistent with the fit at the sub-percent level. On the right, the Shapiro-Wilk p-value is well beyond a 0.05 significance, and the quantile comparison tracks linearly. Taken collectively, this evidence supports that the flux universes in this bin are approximately normally distributed.

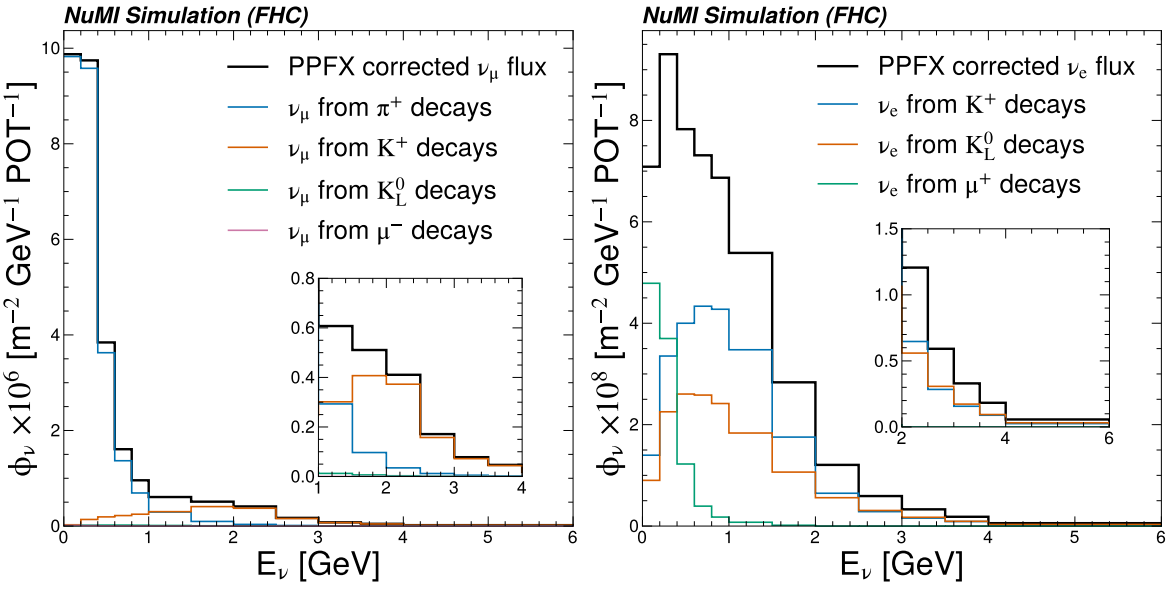

Figure 4.3: Corrected flux spectra for FHC muon (left) and electron (right) neutrinos with the contributions from the decays of their parent particle.

Table 4.2: Horn-flavor-energy element ordering for covariance matrices, read from left to right (columnwise), or bottom to top (row-wise). Refer to Table 4.1 for the E_ν bin stops of each neutrino species.

Row/Column No.	Horn Current	Neutrino Flavor	E_ν Range [GeV]
1–14	FHC	ν_e	[0, 12]
15–28	FHC	$\bar{\nu}_e$	[0, 12]
29–43	FHC	ν_μ	[0, 20]
44–58	FHC	$\bar{\nu}_\mu$	[0, 20]
59–72	RHC	ν_e	[0, 12]
73–86	RHC	$\bar{\nu}_e$	[0, 12]
87–101	RHC	ν_μ	[0, 20]
102–116	RHC	$\bar{\nu}_\mu$	[0, 20]

mode. The upper-left and lower-right quadrants give the covariance between flavors across the two different running modes.

As can be seen in the small boxes, strong positive bin-to-bin correlations were found for neighboring and near-neighboring bins across all flavors in both running modes. The strength of the correlations tends to diminish as the distance between bins increases, and there is almost no correlation between the highest energy bins and the lower energy bins. Regions of stronger correlation tend to be defined by the transitions between where different parent particles dominate the neutrino production.

This trend is also seen for neutrinos of the same flavor produced in different running modes, and to a lesser degree for off-diagonal boxes that give correlations for either neutrino-neutrino pairs, or antineutrino-antineutrino pairs. This is likely due to the fact that neutrinos are mostly produced by positive particles, while antineutrinos are mostly produced by negatively charged particles. Off-diagonal boxes that give correlations between neutrino-antineutrino pairs have the weakest correlations, and even exhibit negative correlations in high-energy bins. Individual covariance matrices for each interaction channel have been included in Appendix G.

The variance of the flux as a function of E_ν is extracted from the diagonals of each component covariance matrices to compute the contributions of each systematic effect to the total. Figure 4.5 shows the fractional contribution of each interaction channel to the systematic uncertainty for both FHC electron and muon neutrinos. Appendix H contains fractional uncertainty contributions to the remaining neutrino modes. The total ν_μ systematic uncertainty is largest in the lower-energy regions of the spectra, where decays from high angle pions dominate. Low energy kaons, many of which undergo secondary interactions on materials other than carbon (see Fig. 3.10) also contribute. For ν_e the lowest energy bins are dominated by neutrinos from muon decays, but above 500 MeV the kaon induced contribution begins to dominate. The uncertainty peaks at 15% (11%) for muon (electron) neutrinos in the 0–200 MeV bin, and is lowest at the 5% level in the 1.5–2.0 GeV bin. From this study, it was found

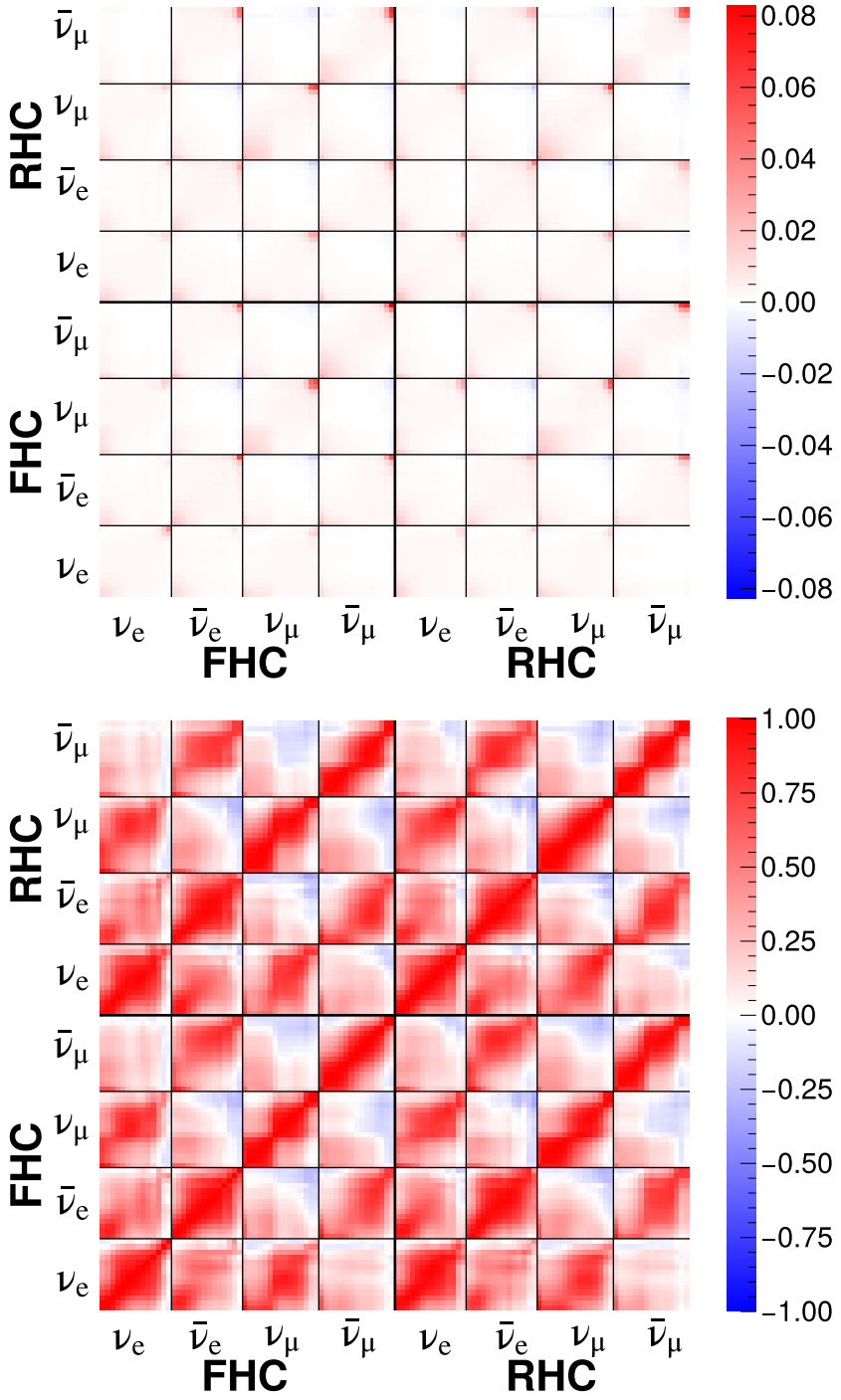

Figure 4.4: Hadron interaction covariance (upper) and correlation (lower) matrix. Each bin in the 2D histogram represents the correlation between corresponding energy bins of fluxes, for a given pair of neutrino modes. Positive correlations are present between the majority of bin pairs, while anti-correlations can be found in the 6–20 GeV region for certain neutrino-antineutrino bins. Refer to Tables 4.1 and 4.2 for the identities of each matrix row/column.

that the dominant contribution to the uncertainty is the incident meson channel. The remaining uncertainty comes from multiple channels at 1–3% level.

As described in Sec. 3.4, hadrons produced in the NuMI beam may interact multiple times before decaying to a neutrino that arrives at ICARUS. Light meson interaction channels are not well-supported by data, therefore these multiply interacting hadrons are subject to the conservatively assigned 40% uncertainty at each step of the chain. Figure 4.6 further decomposes the inclusive meson channel according to the projectile (Fig. 4.6a) and target particle (Fig. 4.6b). The contributions from individual mesons track with the expected flux composition, i.e., for ν_μ, charged pions contribute more significantly at lower values of E_ν, while kaons contribute at higher E_ν. The crossover between uncertainty contributions is consistent with the crossover point between hadron parents. Additional details on the meson incident channels and their contribution to the flux uncertainties can be found in Appendix B.2.

4.2.2 Principal Component Analysis of the Total Hadron Production Covariance Matrix

The PCA of the hadron covariance matrix yielded 116 components, in accordance with the dimensions of the matrix:

$$\begin{aligned} N_{\text{PC}} &= N_{\text{Modes}} \times \left(N_{\nu_\text{e}\ \text{bins}} + N_{\bar{\nu}_\text{e}\ \text{bins}} + N_{\nu_\mu\ \text{bins}} + N_{\bar{\nu}_\mu\ \text{bins}} \right) \\ &= 2 \times (14 + 14 + 15 + 15) \\ &= 116, \end{aligned} \tag{4.12}$$

where each PC is represented by a linear combination of all 116 horn-flavor-energy bins. Eigenvalues associated with components 108–116 were found to be negative, where the largest of these 8 eigenvalues ($\approx -2.90 \times 10^{-17}$) was 16 orders of magnitude smaller than the largest positive eigenvalue (≈ 0.33). Negative eigenvalues of this scale are likely artifacts of floating-point arithmetic, and, for this reason, these 8 eigenvalues were considered to be consistent with 0 and discarded. The remaining eigenvalues and their corresponding explained variances, in the fractional scale, are given in Figure 4.7. It was found that 99% of the variance in the matrix can be described by the first 15 components, while the remaining 85 components encode the final 1%. Regardless, all PCs are retained in an output file, which gives analyzers freedom to adjust the number of PCs used. To demonstrate the features identified by the PCA, Fig. 4.8 shows how some components can follow the trends of the individual channels shown in Fig. 4.5. Appendix I contains the complete PCA results.

The PCA description of the hadron production uncertainties has distinct advantages in analyses. Since the PCs are not correlated with each other, see Fig. 4.9, there is no need to invert a matrix to compute a penalty term for a test statistic. The small cost is that each parameter now adjusts the weights of events across the full E_ν spectrum, and the correct weights in each bin need to be stored and applied correctly.

4.2.3 Uncertainty Due to Focusing of the NuMI Beam

Figure 4.10 shows the fractional uncertainties due to each "beam focusing" systematic as extracted from the diagonals of the corresponding covariance matrices, while Fig. 4.11 shows the correlation matrix accounting for all systematic effects. The remaining covariance and correlation matrices have been included in Appendix L. For muon neutrino modes, the error lies at the 1–2% level for E_ν below 1 GeV, and 3–4% for $1 < E_\nu < 3$ GeV. For electron neutrinos, the uncertainty starts at the 2–3%, but quickly rises to 8% for $E_\nu \geq 3$ GeV. The total beamline systematic uncertainty in the electron neutrino samples is, in general, higher than that of the muon neutrino samples, especially at larger values of E_ν. Estimation of the beamline systematic uncertainties is limited by the relatively low statistics, especially for ν_e and at higher energies where the flux is low. Given that the samples are statistically independent, each included systematic carries some random fluctuations at the level of the sample statistical uncertainties, inflating the estimates in the low statistics regions. Due to the limitations of the characterization of the beamline systematics presented, here, the recommended action is to reproduce the altered geometry samples with higher statistics and using the updated 1 MW beam geometry.

4.2.4 Difference Between the 700 kW and 1 MW Beam Geometries

As discussed in Sec. 2.2, a study was performed to estimate effects on the flux as a result of the 1 MW upgrade to the NuMI Beam. The differences for FHC ν_μ and ν_e are shown in Fig. 4.12, while the remaining neutrino modes have been included in Appendix M. It was found that the differences are small relative to the statistical uncertainty, especially in the RHC operating mode, where there is a factor 10 fewer statistics available for the 1 MW beam geometry. However, there are regions of neutrino energy where the differences at the 2–3% level are statistically significant. So, while it is clear that the upgraded beamline infrastructure changes the flux, the uncertainties on those changes, as extracted by this analysis, are large compared to the size of the effects. Therefore, the flux differences between the two beam configurations is treated as an additional source of systematic uncertainty. Similar to the set of focusing uncertainties, the flux difference can be applied using via E_ν-flavor bins with a covariance matrix, or with a single parameter that adjusts the weights for each bin E_ν-flavor bin according to a vector encoding the flux ratios.

The current analysis should suffice for the current (as of Summer 2023) FHC data sets. However, after summer 2023 the run plan includes significant RHC running and authors recommend, at the very least, creating more RHC flux MC for the nominal configuration of that 1 MW simulation to reduce the propagated statistical uncertainty. Even better would be to move to a full 1 MW simulation across the board. This requires generating a full suite of high statistics NuMI beam MC files using the 1 MW configuration, including all relevant focusing systematics geometry alterations.

4.3 Flux Prediction and Integrated Flux Uncertainty

The complete flux prediction for ν_μ and ν_e in the forward horn operating mode is given in Fig. 4.13. The remaining spectra can be found in Appendix N.1, and a table of the predicted neutrino flux at the geometrical center, top, and bottom of the ICARUS active volume can be found in Section N.3. The total uncertainty on the NuMI neutrino flux was calculated for various neutrino modes, as well as the flux ratio. Table 4.3 contains a selection of the total uncertainties integrated over the full $0 < E_\nu < 20\,\text{GeV}$ range, while a more complete tabulation can be found in Appendix O. These results demonstrate that hadron production systematic uncertainties are greater than or equal to the NuMI focusing uncertainties across the regions of interest. Large flux correlations between flavors (e.g., ν_e/ν_μ or $\bar{\nu}/\nu$) would favor analyses that measured the ratios between interaction processes of the correlated flavors. The correlations would lead to cancellations in the total flux error used in the cross section extraction. Given the low levels of flavor to flavor correlations the uncertainty on the flux ratio is not found to be particularly advantageous, (7.1 and 7.0% for FHC and RHC, respectively), compared to the other flux modes. In fact, anti-correlations found in the covariance matrix will tend to drive the ratio uncertainty upward. Integration of new hadronic interaction data into PPFX from NA61/SHINE and EMPHATIC has the potential to strengthen correlations and reduce uncertainties on ratio measurements.

Table 4.3: Uncertainties on the integrated flux in the 0–20 GeV range. Hadron production uncertainties dominate, with all other effects contributing to sub-percent increases to the quadrature sum. FHC and RHC fractional uncertainties are similar, as are right-sign and wrong-sign errors within the same beam mode. The flux uncertainties on the sum of right and wrong-sign components are less than the uncertainties on either contribution due to mild (strong) off-diagonal flavor-to-flavor regions of the hadron production (beamline focusing) correlation matrices. The uncertainty on the $\nu_e + \bar{\nu}_e$ to $\nu_\mu + \bar{\nu}_\mu$ flux ratio offers little advantage over the standalone $\nu_e + \bar{\nu}_e$ flux due to the lack of strong flavor-to-flavor correlations between the $\nu_e + \bar{\nu}_e$ and $\nu_\mu + \bar{\nu}_\mu$ components.

	Uncertainty (%)						
Horn Mode	ν_e	$\bar{\nu}_e$	$\nu_e + \bar{\nu}_e$	ν_μ	$\bar{\nu}_\mu$	$\nu_\mu + \bar{\nu}_\mu$	$\frac{\nu_e + \bar{\nu}_e}{\nu_\mu + \bar{\nu}_\mu}$
Hadron							
FHC	6.63	5.84	5.76	11.32	10.19	9.08	6.83
RHC	5.86	6.76	5.77	10.74	11.27	9.45	6.92
Beamline							
FHC	1.23	1.49	0.82	1.12	2.37	1.42	1.47
RHC	2.60	1.48	2.15	1.35	1.40	0.88	1.40
Beam Power Upgrade							
FHC	2.42	1.13	0.52	1.37	1.45	0.35	0.87
RHC	0.67	2.12	1.19	1.56	2.28	0.18	1.37
Statistical							
FHC	0.26	0.24	0.18	0.09	0.06	0.05	0.18
RHC	0.21	0.29	0.17	0.06	0.09	0.05	0.18
Total							
FHC	7.17	6.13	5.85	11.45	10.56	9.20	7.04
RHC	6.45	7.24	6.27	10.94	11.58	9.50	7.20

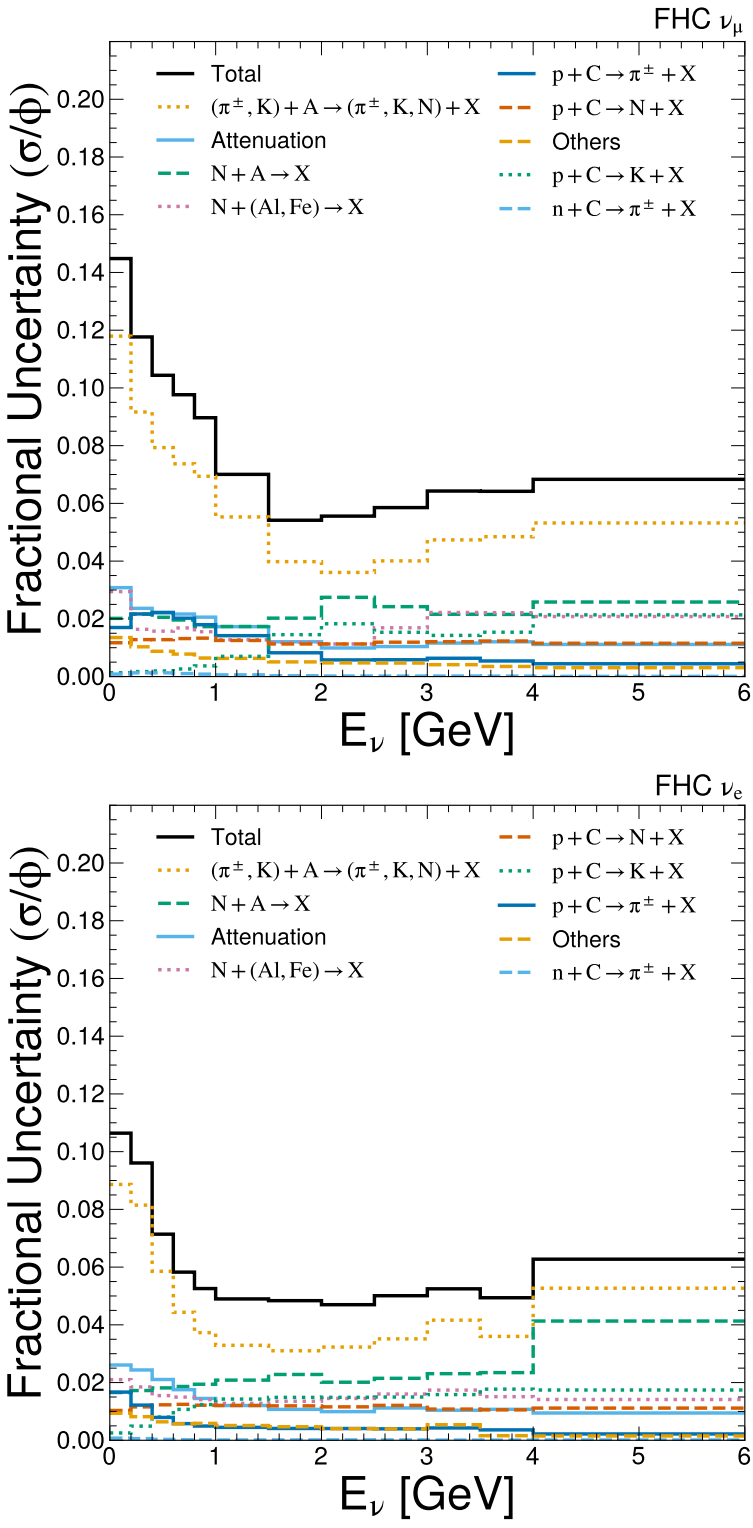

Figure 4.5: Hadron interaction fractional uncertainties for muon (top) and electron (bottom) neutrinos. Re-interacting mesons constitute the largest source of uncertainty. Note that the legend is ordered according to the contribution to the total uncertainty within the displayed range of neutrino energy.

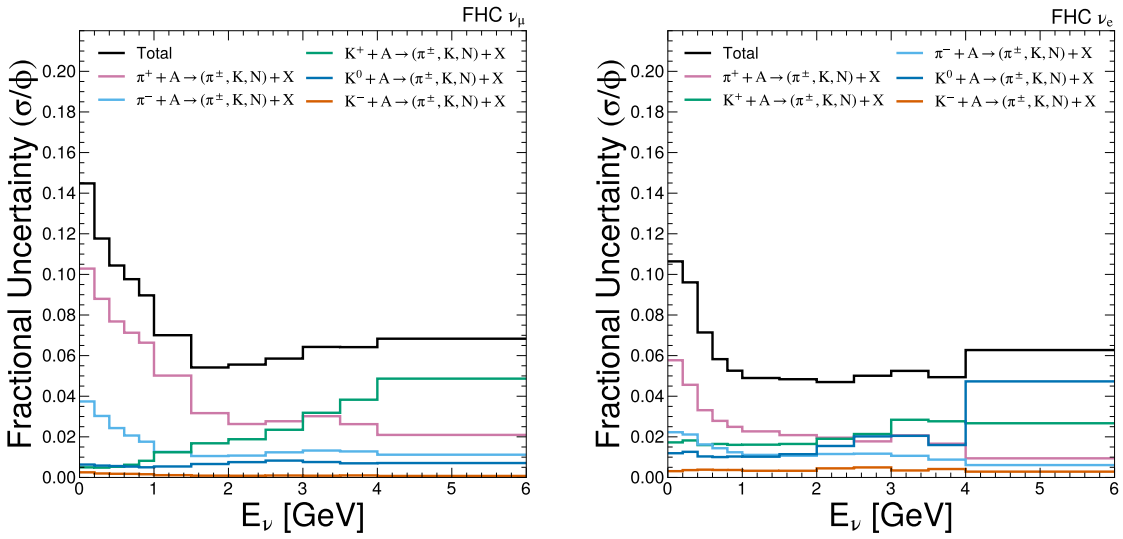

(a) Uncertainty contribution by incoming meson.

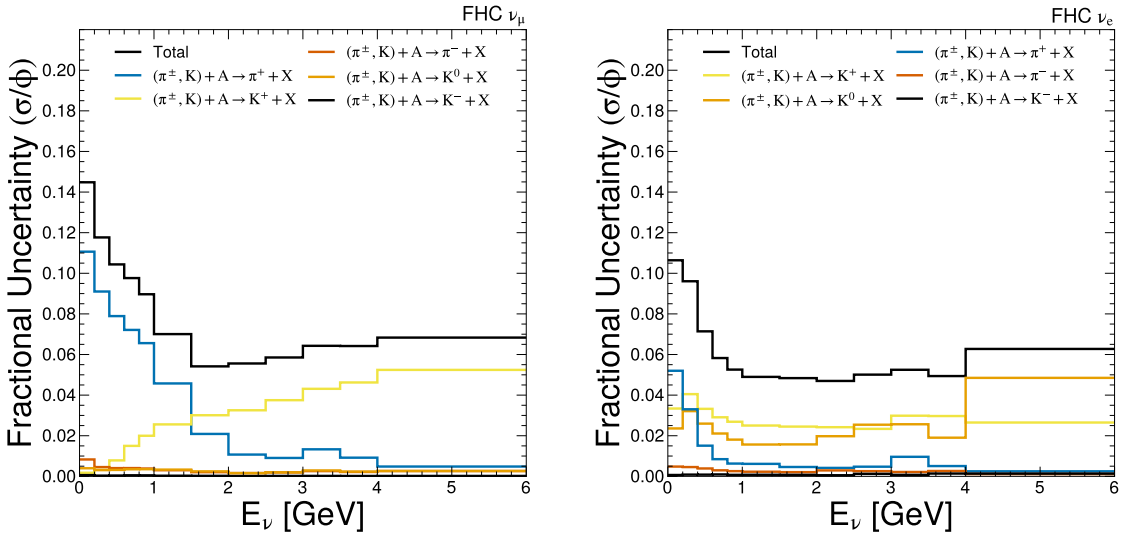

(b) Uncertainty contribution by outgoing meson.

Figure 4.6: Uncertainty contributions to the meson-incident channel, grouped by the incoming meson flavor (a) and the outgoing meson flavor (b). For elastic collisions the categorization is the same, however inelastic collision can change the flavor of the incoming particle, or produce multiple outgoing particles.

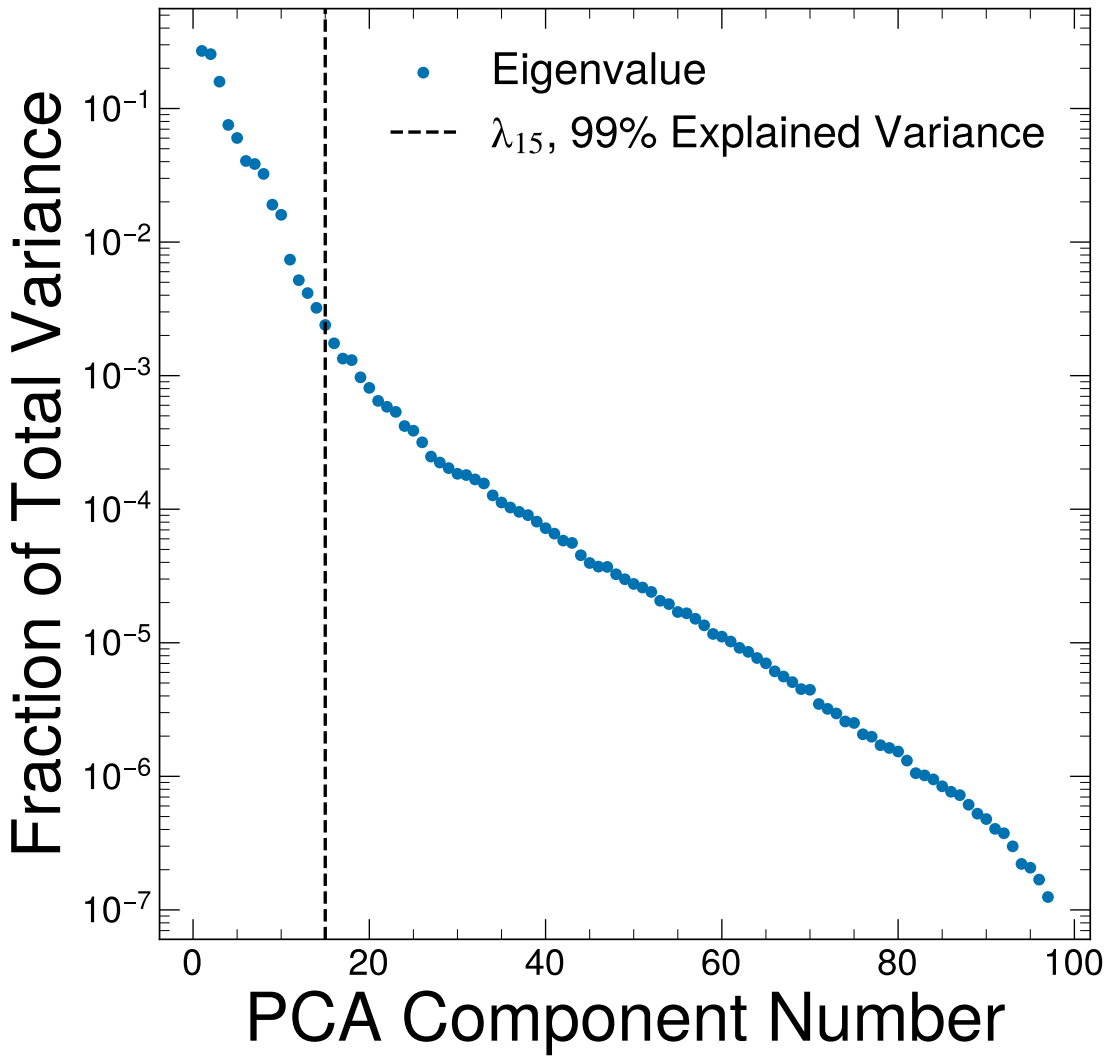

Figure 4.7: Scree plot from the PCA of the hadron covariance matrix. As an example, a dashed line is drawn to demonstrate a threshold eigenvalue, λ_{15}, to the left of which 99% of the variance is described, cumulatively.

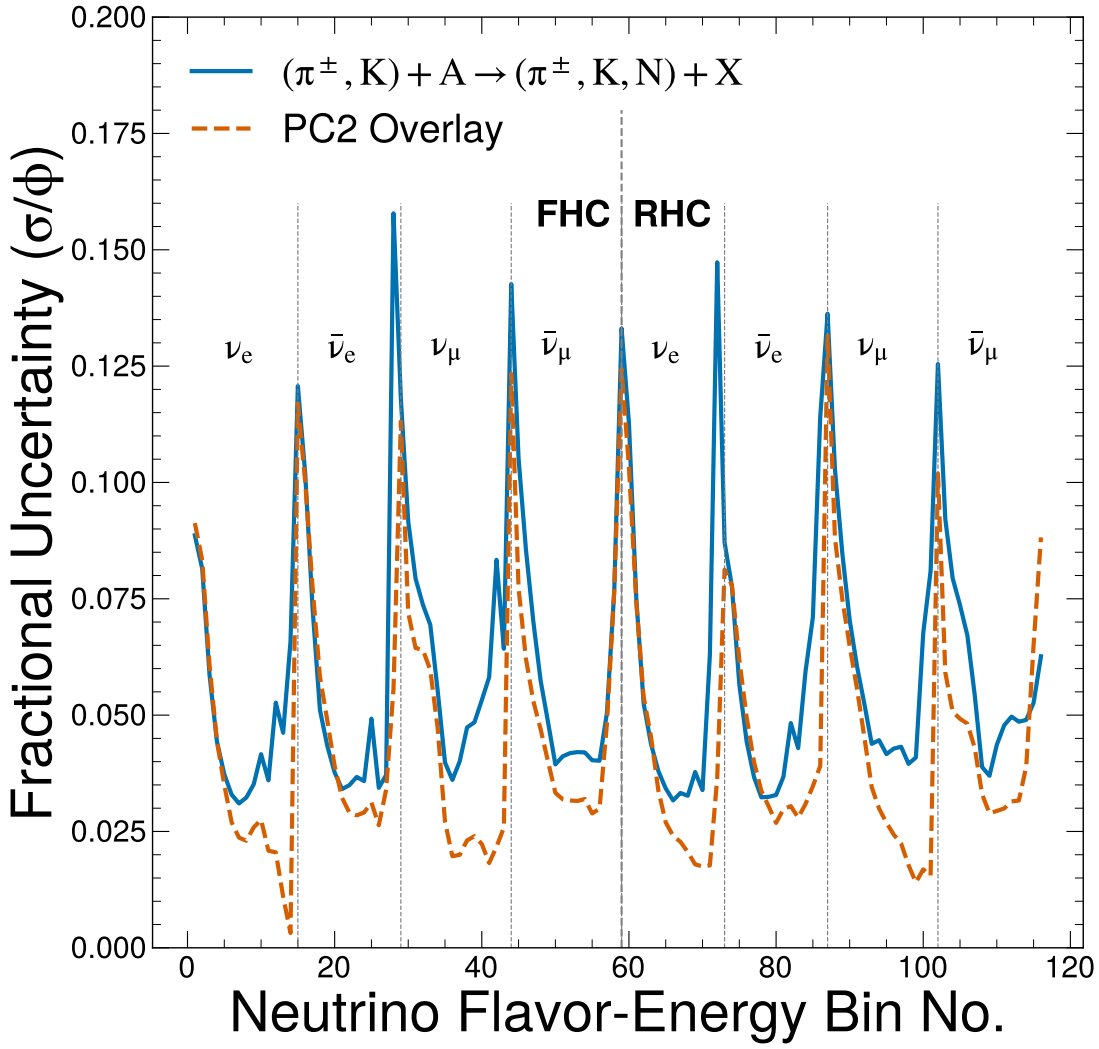

Figure 4.8: Uncertainty due to meson interactions (blue) transposed from bins of neutrino energy and flavor to component numbers. An overlay of the second component (orange) indicates this component captures much of the low-energy variance related to meson interactions. Refer to Tables 4.1 and 4.2 for more details about bin numbering scheme.

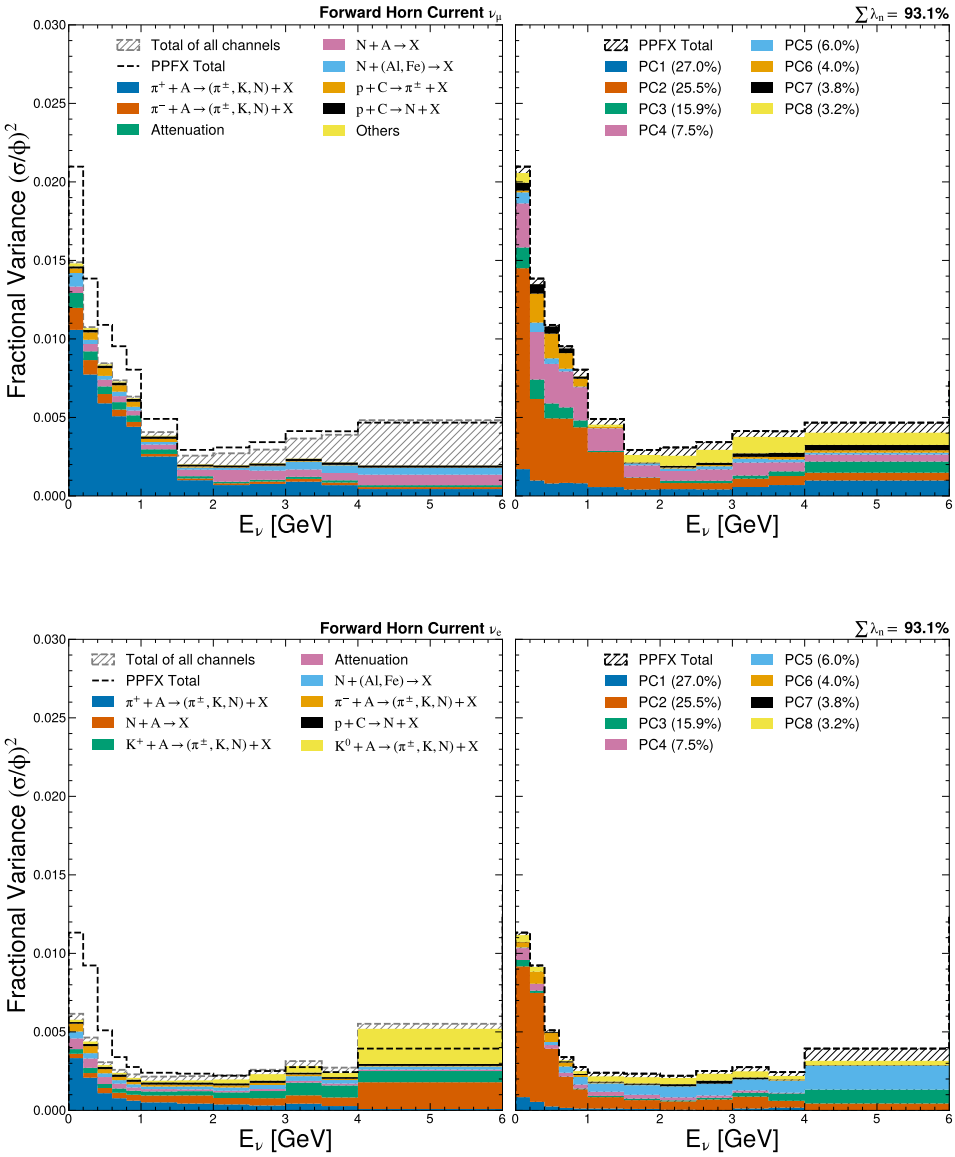

Figure 4.9: Variance contributions from the top 8 Hadron Production Channels (HPCs, left), and top 8 principal components (PCs, right) for FHC ν_μ (top) and ν_e (bottom). The "PPFX Total" represents the variance across universes, which correctly accounts for correlations across the HPCs, and thus matches between the HPCs and PCs. The "Total of all channels" is the sum of the variances of each individual HPCs, which does not properly account for correlations between HPCs. In contrast, the right-hand plots, demonstrate that, because of their linear independence, the PCs fully describe the total variance in the flux from hadron model uncertainties. The discrepancy between these two quantities highlights how channel-to-channel correlations affect bin-to-bin correlations in E_ν. One can also compare the HPC effects with the PCs to estimate which physical effects are captured by each of the PCs and where strong correlations between HPCs allow them to be grouped into a single PC.

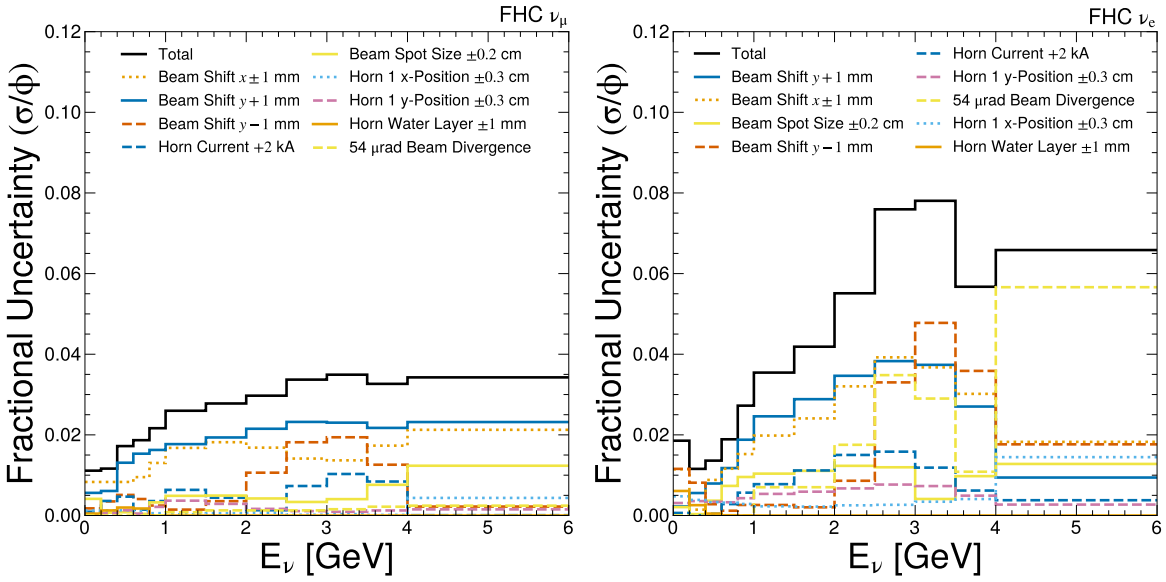

Figure 4.10: Beamline focusing fractional uncertainties for both FHC electron and muon neutrino modes. In both cases, shifting of the proton beam spot on the target in the x/y direction constitutes the largest contribution to the total beamline uncertainty.

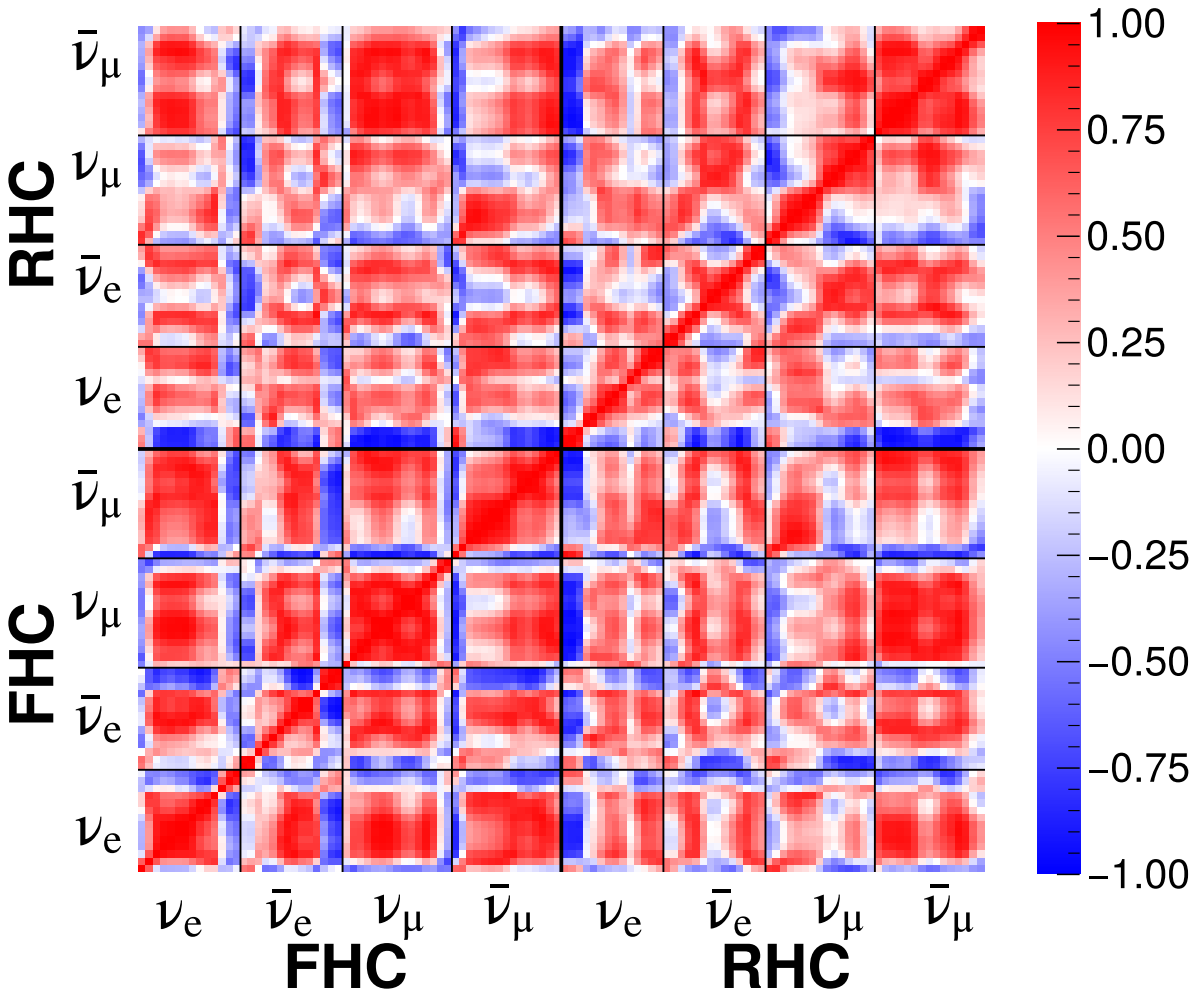

Figure 4.11: Beamline focusing correlation matrix, incorporating all systematic effects. Strong positive correlations are found between most neighboring bins. Strong positive correlations are most prevalent in the lowest energy (~0–0.5 GeV), medium energy (~0.5– 3.5 GeV) and high energy (~5.5–20 GeV) regions. Correlations between these regions tend to be small or negative. Significant negative correlations are also found between the low energy RHC ν_e bins and nearly all other neutrino flavor-energy bins. The RHC $\bar{\nu}_e$ flux exhibits interesting behavior and correlations with other flux components.

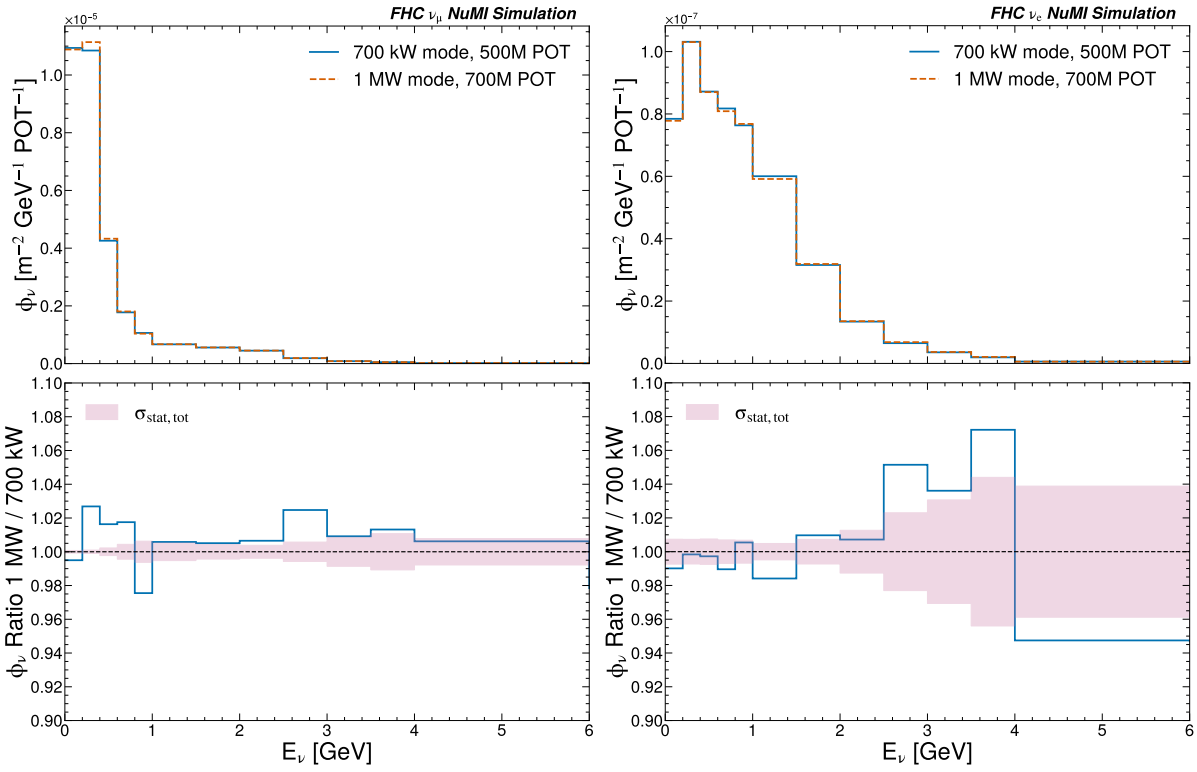

Figure 4.12: Comparison of neutrino flux with 700 kW beamline geometry NuMI simulation (used in this note), and newer 1 MW beamline geometry simulation for ν_μ (*left*) and ν_e (*right*).

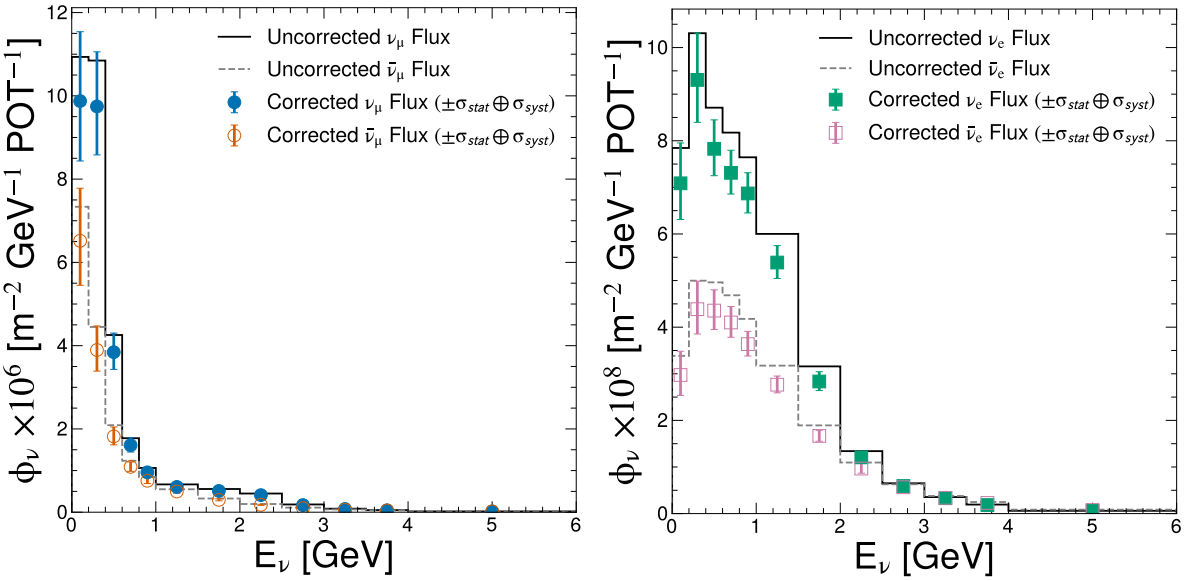

(a) ν_μ and $\bar{\nu}_\mu$

(b) ν_e and $\bar{\nu}_e$

Figure 4.13: The NuMI flux spectra in the forward horn operating mode expected at ICARUS with full uncertainties accounting for hadron production, beam focusing, and statistical effects. In panel (a), the unweighted ν_μ ($\bar{\nu}_\mu$) flux is shown in black (gray), while the PPFX corrected flux with total uncertainties is shown in blue (orange). In panel (b), the unweighted ν_e ($\bar{\nu}_e$) flux is shown in black (gray), while the PPFX corrected flux with total uncertainties is shown in green (pink).

5 CONCLUSION

This note contains a characterization of the NuMI flux simulation for the ICARUS detector. Monte Carlo simulation of the NuMI flux, originally prepared by NOνA, were studied using information stored in the dk2nu format and with PPFX.

5.1 The NuMI Beam Simulation Dataset

No obvious shortcomings of the simulated NuMI geometry were found. However, the simulation may benefit from the addition of the presently unmodeled structures around Horn 1, but the effect might be small, see Sec. 3.5. The 500M POT sample was sufficient to study the impact of hadron model uncertainties, but sample statistics limited the capability to study the beamline uncertainties, especially above 3 GeV. That analysis would benefit from higher statistics; however, a conservative approach was taken to estimate the uncertainties, see Sec. 4.2.3. The simulation was performed for the 700 kW NuMI configuration used between 2014–2018. Since 2019, the NuMI beam is operated in a 1 MW configuration. A preliminary study did not reveal substantial differences, but a new set of 1 MW files, including FHC and RHC files along with the full suite of beamline/focusing systematically altered geometries should be generated for the future studies. Experimental uncertainties on the POT counting (Main Injector beam intensity measurements) are not covered by the simulation and must be included separately in the analysis based on POT counting uncertainties from beamline operations.

5.2 Characteristics of High Off-axis Angle Neutrino Beam

The ICARUS detector location in NuMI coordinates [25] was revised and corrected. A non-negligible flux dependence on the vertical coordinate was discovered, see Sec. 3.2. It was determined that more than 70% of neutrinos above 0.5 GeV travelling to ICARUS originate from decays very close to the NuMI target, see Sec. 3.6. The Earth's magnetic field does not have a significant impact on the flux, see Sec. D. Hadrons undergo significantly more interactions before decaying to neutrinos travelling to ICARUS, in comparison to on-axis experiments, making the flux more sensitive to hadron model uncertainties, see Sec. 3.4. Significant contribution of the wrong sign neutrino flux is present in ICARUS in both forward and reverse horn current configurations, see Sec. 3.3.

5.3 Hadron Model Uncertainties

The NuMI neutrino flux systematic uncertainties are currently driven by hadron interaction uncertainties, as discussed in section 4.1.5. The dominant contribution to the hadron model uncertainties were found to be the interactions of kaons and charged pions at 5–40 GeV/c on carbon, aluminum and iron. This contribution is the leading source of uncertainties for the on-axis experiments as well [12]. Improvements to the underlying hadron interaction modeling are expected as a result of measurements being made by NA61/SHINE and EMPHATIC.

The flux of ν_e, $\bar{\nu}_e$, ν_μ and $\bar{\nu}_\mu$ in ICARUS from the NuMI beam line in forward and reverse horn current polarities was estimated. An analysis of the uncertainties related to modeling of hadron interactions and the beamline, as well as correlations between the flux of the various neutrino modes, was performed. The total uncertainty on the flux, accounting for statistical and systematic effects, was found to be 11.5% and 7.0% for focused ν_μ and ν_e, respectively. The uncertainty on the flux ratio was also studied and calculated as 7.1% in the forward horn operation, and 7.0% in the reverse horn operation. As such, performing ratio measurements of the neutrino interaction cross section on argon nuclei does not grant a significant advantage over other methods. However, the integrated uncertainty due to hadron interaction modeling was discovered to be lower than initially expected. See Ref. [28, 30] to access the analysis code and a file containing these results.

A Flux File README

GitHub Repository https://github.com/woodtp/flux-tool

This package reads neutrino flux universes produced by Package to Predict the Flux (PPFX), and extracts a neutrino flux prediction with corresponding uncertainties. All analysis products are output to a .root file specified in a config.toml. The package will also produce figures as pdf, png, and a .tex, for the majority of the products stored in the ROOT file.

A.1 Prerequisites

Before you begin, make sure you have the following prerequisites installed:

- Python 3.11 or later: Visit the official Python website at https://www.python.org/downloads to download and install the latest version of Python.
- ROOT 6.28 or later: **Flux-Tool** requires ROOT/PyROOT version 6.28 or later. You can obtain ROOT from the official ROOT website at https://root.cern/install.

A.2 Installation

Flux-Tool is available for installation from PyPI, the Python Package Index. Follow the steps below to install the project from the terminal:

1. Create a virtual environment (optional but recommended):

```
$ python -m venv myenv
```

2. Activate the virtual environment:

```
$ source myenv/bin/activate
```

3. Install Flux-Tool using pip:

```
$ pip install flux-tool
```

A.3 Usage

```
$ flux_tool -h
usage: flux_uncertainties [-h] [-c CONFIG] [-p PRODUCTS_FILE] [-v] [-z]

This package coerces PPFX output into a neutrino flux prediction
with uncertainties, and stores various spectra related to the flux,
e.g., fractional uncertainties, covariance matrices, etc.

options:
  -h, --help            show this help message and exit
```

```
  -c CONFIG, --config CONFIG
                        specify the path to a toml configuration file
  -p PRODUCTS_FILE, --plots-only PRODUCTS_FILE
                        Specify path to an existing ROOT file for which
                        to produce plots
  -v, --verbose
  -z, --enable-compression
                        Enable compression of the output plots directory
```

Alternatively, this package can be imported directly into an existing python script:

```
import flux_tool
```

A.3.1 Example config.toml

```
# flux_tool configuration file

output_file_name = "out.root"
sources = "/path/to/directory/containing/input/histograms"

[Binning]
# Histogram bin edges for each neutrino flavor.
# Accepts:
#    1. an integer number of bins (between 0 and 20 GeV)
#    2. An array of bin edges (NOTE: they can be variable bin widths,
#       but must be monotonically increasing)
#    3. If unspecified, then fixed bin widths of 100 MeV is applied along
#       the [0, 20] GeV interval.
nue = 200
nuebar = [
  0.0,
  0.2,
  0.4,
  0.6,
  0.8,
  1.0,
  1.5,
  2.0,
  2.5,
  3.0,
  3.5,
  4.0,
  6.0,
  8.0,
  12.0,
```

```
]
numu = []
numubar = [
  0.0,
  0.2,
  0.4,
  0.6,
  0.8,
  1.0,
  1.5,
  2.0,
  2.5,
  3.0,
  3.5,
  4.0,
  6.0,
  8.0,
  12.0,
  20.0
]

  [PPFX]
# enable/disable specific PPFX reweight categories from
# appearing in the fractional uncertainty directory
# true = included, false = excluded
[PPFX.enabled]
attenuation = true
mesinc = true
mesinc_parent_K0 = true
mesinc_parent_Km = true
mesinc_parent_Kp = true
mesinc_parent_pim = true
mesinc_parent_pip = true
mesinc_daughter_K0 = true
mesinc_daughter_Km = true
mesinc_daughter_Kp = true
mesinc_daughter_pim = true
mesinc_daughter_pip = true
mippnumi = false
nua = true
pCfwd = false
pCk = true
pCpi = true
pCnu = true
pCQEL = false
```

```
others = true
thintarget = false

[Plotting]
draw_label = true # whether or not to draw the experiment label,
                  # e.g., ICARUS Preliminary
experiment = "ICARUS"
stage = "Preliminary"
neutrino_energy_range = [0.0, 6.0] # horizontal axis limits in [GeV]

[Plotting.enabled]
# Enable/disable specific plots from the visualization output
uncorrected_flux = true
flux_prediction = true
flux_prediction_parent_spectra = true
flux_prediction_parent_spectra_stacked = true
ppfx_universes = true
hadron_uncertainties = true
hadron_uncertainties_meson = true
hadron_uncertainties_meson_only = true
pca_scree_plot = true
pca_mesinc_overlay = true
pca_top_components = true
pca_variances = true
pca_components = true
hadron_covariance_matrices = true
hadron_correlation_matrices = true
beam_uncertainties = true
beam_covariance_matrices = true
beam_correlation_matrices = true
beam_systematic_shifts = true
```

A.4 Contents of the Output ROOT File

- beam_samples If provided to flux_tool, copies of the systematically altered neutrino flux samples, including the nominal, are stored here.
- beam_systematic_shifts Fractional shifts from the nominal, calculated for each flux sample in beam_samples.
- covariance_matrices Contains all covariance and correlation matrices, organized into two subdirectories: one for hadron effects and another for beam effects (if applicable). Each covariance matrix is stored in 2 forms:
  (i) `TH2D` (prefixed hcov_ or hcorr_)
  (ii) `TMatrixD` (prefixed cov_ or corr_)

Covariance matrices with the _abs suffix are in absolute units of the flux, whereas those without the suffix are normalized the PPFX universe mean, in the case of hadron systematics, or to the nominal beam run, in the case of the beam line systematics. Each bin is labeled according to the combination of horn polarity, neutrino flavor, and energy bin number, e.g., fhc-nue-1.

- flux_prediction This directory holds a set of TH1D for each neutrino mode. The flux value is extracted as the PPFX mean, while the uncertainties incorporate statistical, hadron systematic, and beam line systematic (if applicable) uncertainties.
- fractional_uncertainties This directory contains two subdirectories, beam and hadron, containing the fractional contributions to the flux uncertainty for each effect.
- pca This directory houses the outputs of the Principal Component Analysis of the hadron covariance matrix.
  - `eigenvectors/hevec_*` Unit eigenvectors
  - `principal_components/hpc_*` principal components scaled by the square root of the corresponding eigenvalue and transposed into bins of neutrino energy
  - `hcov_pca` reconstructed hadron covariance matrix used for validation purpose.
  - `heigenvals` Each bin of this histogram (TH2D) holds the eigenvalues extracted from the PCA
  - `heigenvals_frac` same as the previous, but each eigenvalue is divided by the sum of all eigenvalues such that each eigenvalue is represented as its contribution to the total variance.
- ppfx_corrected_flux Directory containing the PPFX-corrected neutrino spectra. These histograms are produced by calculating the means and sigmas of the flux distributions across the 100 universes contained in ppfx_output.
- ppfx_flux_weights Directory containing TH1D for each horn-neutrino flavor combination, the bins of which contain weights that can be used to apply the PPFX flux correction.
- ppfx_output Contains the original output received from PPFX, organized into two subdirectories corresponding to Forward Horn Current (FHC) and Reverse Horn Current (RHC). Each contains a nom subdirectory which holds the nominal (uncorrected) neutrino flux vs. energy spectrum, hnom_nu*, in addition to the PPFX central value, hcv_nu. Spectra broken down by parent hadron can be found under the parent subdirectory. The remaining subdirectories hold the universes for each hadron production systematic:
- statistical_uncertainties Directory containing statistical uncertainties for every horn-neutrino flavor combination. Histograms with the suffix _abs are in absolute units of the flux, and those without the suffix are in the fractional scale. The two matrices, hstatistical_uncertainty_matrix and statistical_uncertainty_matrix, are diagonal TH2D and TMatrixD, respectively, organizing the statistical uncertainties into a useful form to be added with covariance matrices.
- corr_total TMatrixD correlation matrix incorporating all sources of uncertainty

- cov_total_abs TMatrixD covariance matrix in units of the flux, incorporating all sources of uncertainty
- hcorr_total TH2D correlation matrix incorporating all sources of uncertainty
- hcov_total_abs TH2D covariance matrix in units of the flux, incorporating all sources of uncertainty
- matrix_axis TAxis with the binning and labels of all matrix axes
- xaxis_variable_bins TAxis containing the binning applied to all spectra w.r.t. E_ν in GeV.

B Meson interactions in PPFX

This section provides details on how PPFX calculates flux uncertainty related to interactions of mesons, which turns out to be the dominant contribution with the present estimates.

PPFX categorizes "meson incident" interactions by the flavor and kinematics (transverse momentum, p_T, and Feynman x, x_F) of the incoming meson, and the flavor of the outgoing hadron. A bug in the calculation of x_F led to events being grouped together incorrectly for the purpose of uncertainty propagation. The result was a overestimation of the normalization uncertainty of the inclusive "meson incident" channel, and a corresponding underestimation of the shape uncertainty. At the large 5.75° off-axis angle of ICARUS, the meson incident channel dominated the uncertainty budget, inviting additional scrutiny of the individual processes involved. Questions about the strongly correlated nature of the uncertainties in E_ν/flavor bins led to an investigation of the individual channels and the eventual discovery of the bug.

B.1 PPFX Procedure to Estimate Uncertainties Due to Meson Interactions

PPFX does not include any data for meson interaction channels, so there are no PPFX corrections based on data/MC differences. However, PPFX does estimate an uncertainty on these processes and propagates them to the neutrino flux. The process begins by binning each meson incident interaction process into x_F and p_T. PPFX considers five potential incoming mesons (π^+, π^-, K^+, K^-, K^0) and seven potential outgoing hadrons (π^+, π^-, K^+, K^-, K^0, p, n). This gives $5 \times 7 = 35$ p_T vs. x_F distributions. Each of them is broken into 4 bins that span the p_T range from 0 to 2 GeV/c, and split x_F into 4 evenly spaced ranges from 0 to 1. A small number of interactions falls outside this kinematic range, and an additional bin is used across all 35 spectra for these interactions. This leads to a total of $5 \times 7 \times 4 + 1 = 141$ bins.

In each flux universe, for each bin specified above, PPFX draws a random multiplicative weight from the normal distribution with mean equal 1 and σ equal 40%, to alter the corresponding meson interaction cross section. No correlations are considered for meson interactions.

B.2 The PPFX x_F Bug

PPFX characterizes the momentum vector of the produced hadrons using p_T and x_F. The transverse momentum refers to the component of the outgoing particle momentum perpendicular to the incoming participle direction. Feynman x is defined as:

$$x_F = \frac{p_L^{CMS}}{p_L^{CMS\ max}}\,, \tag{B.1}$$

where p_L^{CMS} is the longitudinal momentum of the produced particle in the system of the projectile particle and a nucleon of the target nucleus, and $p_L^{CMS\ max}$ is the maximum value this momentum could achieve within the kinematic limits. Typically in the literature it is estimated as:

$$p_L^{CMS\ max} = \frac{\sqrt{s}}{2c}\,, \tag{B.2}$$

where $\sqrt{s}$ is the energy in the center of mass of the projectile particle and the target nucleon, and c is the speed of light.

Feynman x is thus a dimensionless variable characterizing the longitudinal momentum, with the values ranging from -1 to $+1$. A value of -1 corresponds to particles produced in the most backward region in the center of mass (CoM) frame, while $+1$ indicates production in the most forward region in the CoM frame. A value of 0 indicates are particles produced in the transverse direction in the CoM frame. It was chosen to be used in PPFX as it allows an approximate interpolation between experimental spectra of the produced particles as a function of CoM collision energy.

PPFX follows the procedure described in Ref. [31] Sec 49.2, in particular, Eq. (49.3) to calculate x_F:

$$\sqrt{s} = \left(m^2_{\text{projectile}} + \boldsymbol{m}^{\mathbf{2}}_{\text{target}} + 2E_{\text{projectile}}\boldsymbol{m}_{\text{target}}\right)^{1/2}\,, \tag{B.3}$$

with Eq. (49.4) for the velocity of the center of mass:

$$\beta^{CoM} = \frac{p^{LAB}_{\text{projectile}}}{E^{LAB}_{\text{projectile}} + \boldsymbol{m}_{\text{target}}}\,, \tag{B.4}$$

where $p^{LAB}_{\text{projectile}}$ and $E^{LAB}_{\text{projectile}}$ are the momentum and the energy of the projectile in the laboratory frame. In the original code, the mass of the target m_{target} was erroneously substituted with the mass of the projectile particle $m_{\text{projectile}}$. This has no effect on interactions between nucleons (p+C, n+C, N+A, N+(Al,Fe)), since the mass of the projectile and the target are indeed the same. However, the masses of the most commonly interacting mesons: pions and kaons, are significantly lower than the mass of the nucleon. As a result, the assigned x_F in meson interactions was artificially shifted towards the negative values. Examples are shown in Fig. B.1 This does not affect the actual kinematics of the hadron interaction, as it is defined by the GEANT4 simulation, but it changes the bins PPFX uses to assign weights, and more importantly how it groups interactions assigned the same weight, when generating a flux universe.

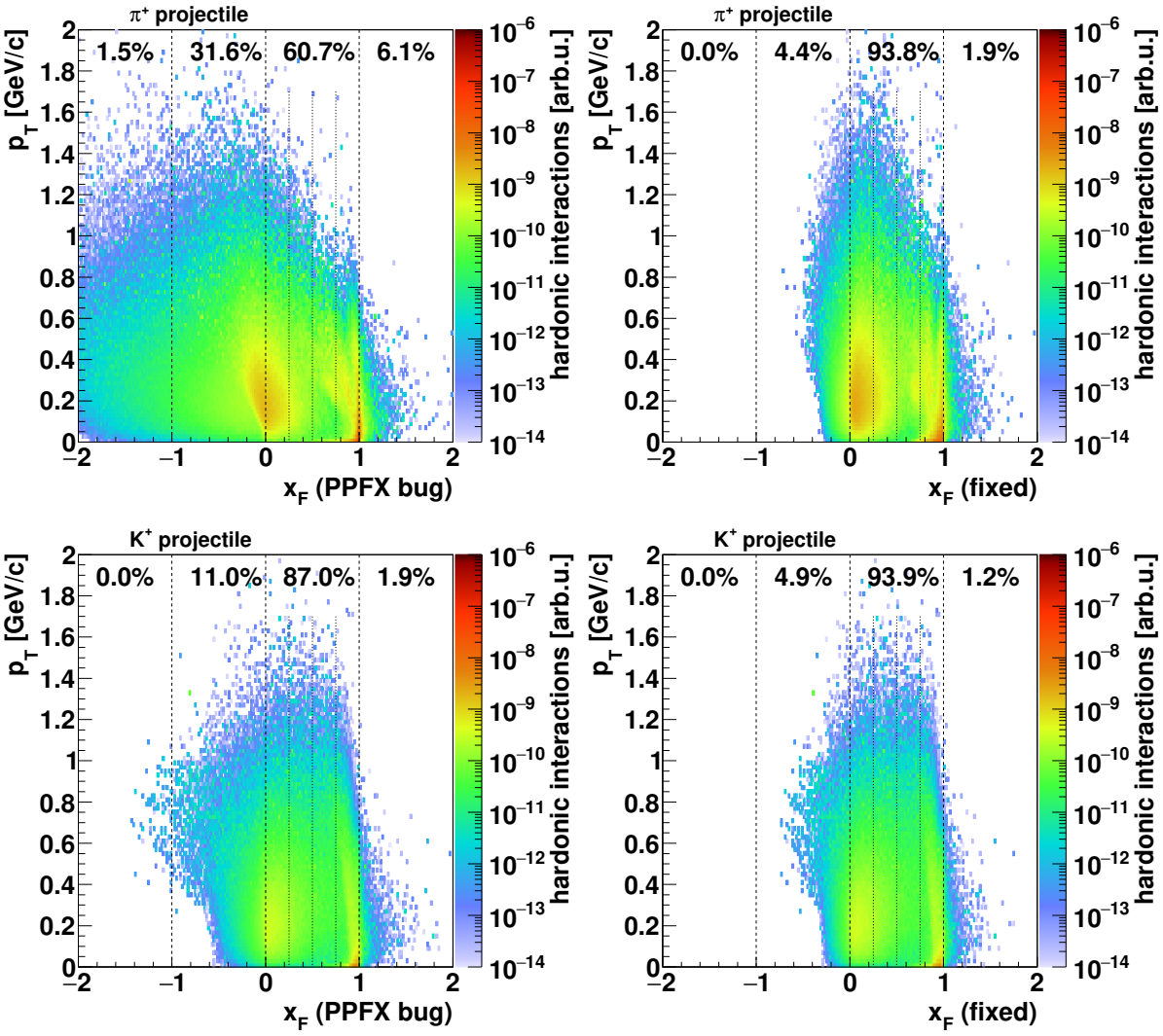

Figure B.1: Distributions of transverse momentum (p_{T}) and Feynman x (x_{F}) in interactions of π^+ and K^+ ancestors leading to production of neutrinos going to ICARUS, with x_{F} calculated with the bug, and with the bug fixed. Vertical dotted lines mark the PPFX x_{F} category boundaries (0–0.25–0.5–0.75–1), and physical x_{F} kinematic limits (±1). The top line lists statistics in the corresponding x_{F} ranges.

The large impact of the bug stems from the fact that many interactions were moved to the catchall "other" category, shared between all 35 meson incident channels. This leads to all the associated neutrinos being assigned the same weight, thus building large correlations into the assigned uncertainty. Figure B.2 shows an example distribution of the number of meson interactions per electron neutrino, calculated without and with the bug fix. As the average PPFX correction for meson interactions in all universes equals unity, the total number of meson interactions (sum of contributions from all categories) is the same in both plots. However, without the bug fix, only one out of 141 PPFX categories, "other", shown in black, covers a significant fraction of interactions spanning across a wide range of neutrino energies.

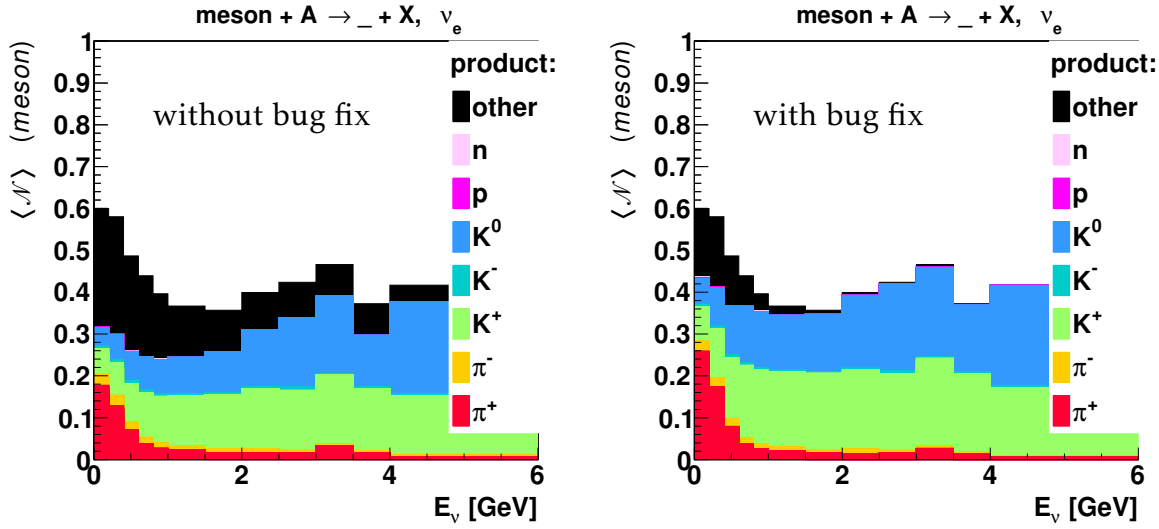

Figure B.2: Number of meson interaction per electron neutrino, broken down into PPFX categories (see text), without (*left*) and with (*right*) the bug fix. Each color band represents 20 categories (5 projectiles × 4 x_F bins) for a given produced particle, which for clarity, was not further broken down in this plot. The black band, represents the catchall "other" category, which includes all events from all meson incident interactions outside the $0 < x_F < 1$ and $0 < p_T < 2$ GeV kinematic range.

Given that each interaction channel bin has large relative uncertainty of 40%, the contributions from 141 independent universes will add in quadrature. When a large fraction of interactions is assigned to the "other" category, it tends to dominate the flux uncertainty. This resulted in the uncertainty related to meson interactions exceeding 20% at low energies, and a large contribution to correlations between the neutrino energy bins. The bug fix significantly decreases the normalization uncertainty on the flux energy/flavor spectrum at the expense of a similarly significant increase in the shape uncertainty.

The reason the bug affects the off-axis flux more than the on-axis flux is two-fold. First, highly off-axis neutrinos are more likely to have a meson interaction in their parent chain. Second, is that off-axis neutrinos originate from decays of hadrons of lower momenta. These hadrons have lower x_F at their production point. Low values of x_F are more likely to be pushed towards the negative range by the bug, causing them to shift into the "other" category.

B.3 Contribution of Meson Interactions to Flux Correlations

Figure B.3 and B.4 shows the number of meson interactions per neutrino. For simplicity, only outgoing mesons which have a large contribution to neutrino production are shown, i.e., π^+ and K^+ for ν_μ, and K^+ and K^0 and for ν_e. These mesons are not always the direct neutrino parents, as they may re-interact, but this does not make the plots less informative. The following meson interactions contribute the most to the meson production:

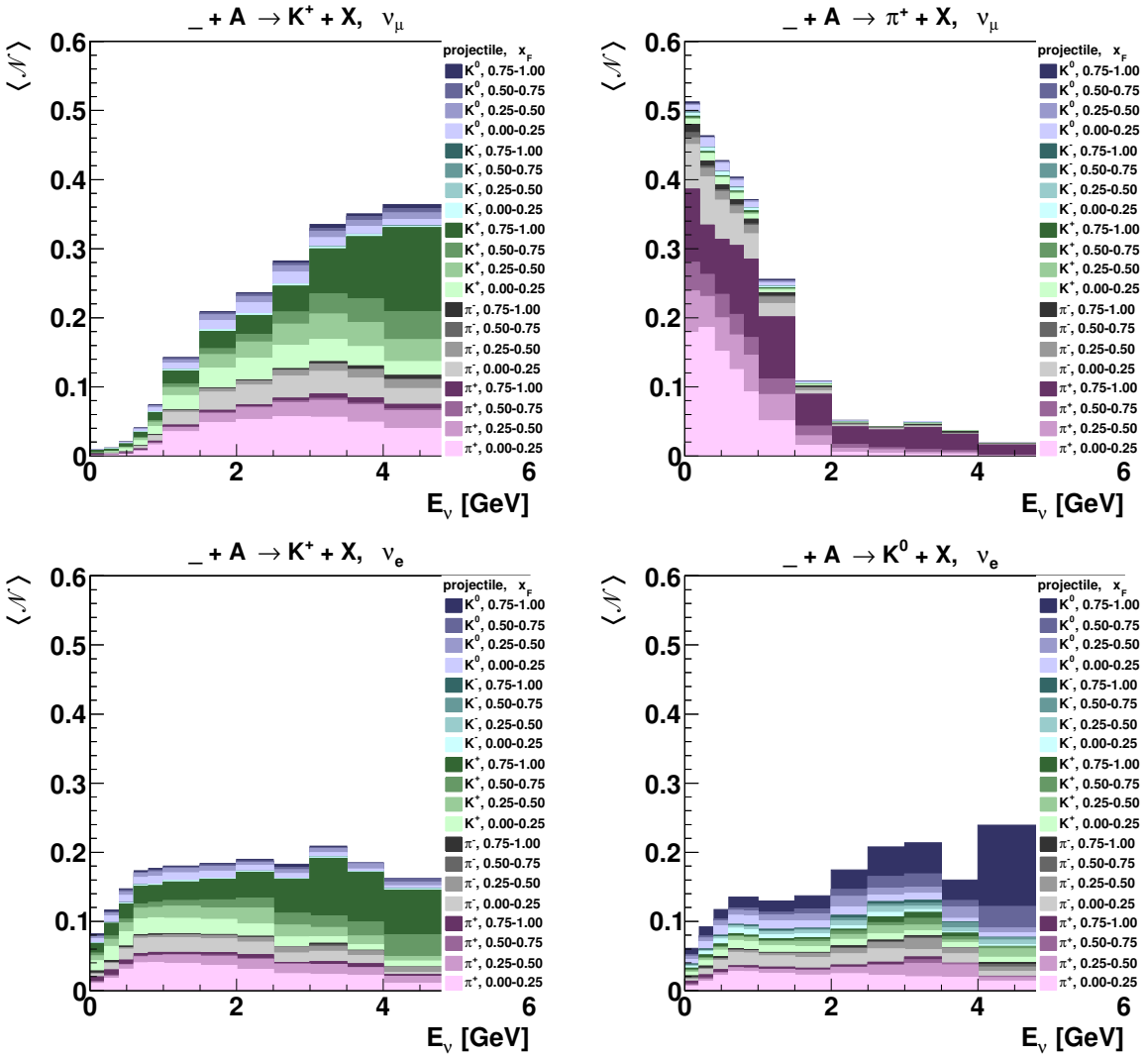

Figure B.3: Number of meson interactions leading to production of selected mesons, in interaction chains leading to **neutrino** production, as a function of **neutrino** energy. The *top* row shows K^+ (*left*) and π^+ (*right*) production in ν_μ chains. The *bottom* row shows K^+ (*left*) and K^0 (*right*) production in ν_e chains. The distribution is broken down according to PPFX meson interaction categories. Five hues correspond to possible meson projectiles: π^+ (pink), π^- (gray), K^+ (green), K^- (teal) and K^0 (violet). Four shades of each color correspond to the x_F bins of the produced mesons, from 0–0.25 (the lightest) to 0.75–1 (the darkest).

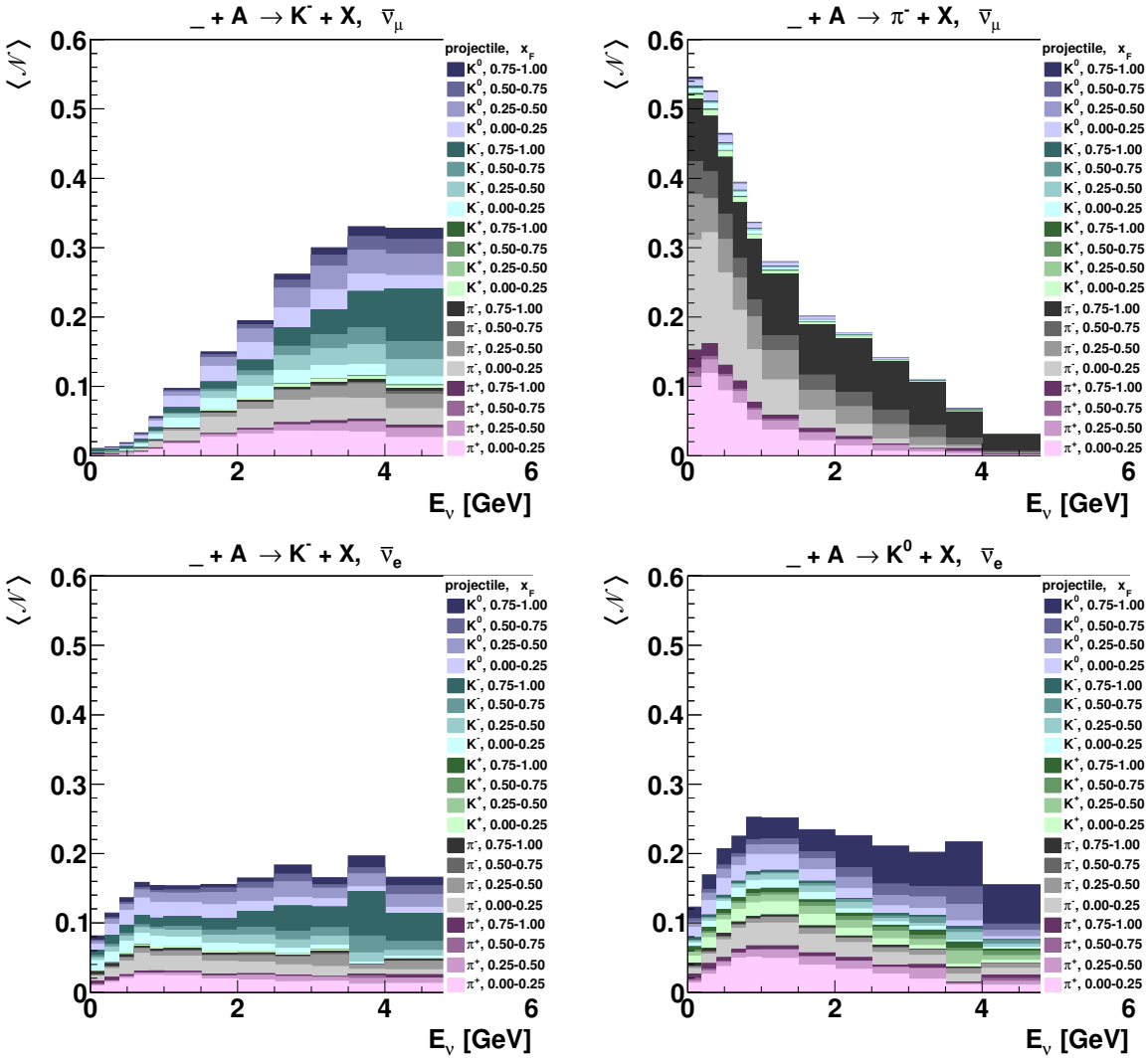

Figure B.4: Number of meson interactions leading to production of selected mesons, in interaction chains leading to **antineutrino** production, as a function of **antineutrino** energy. The *top* row shows K^- (*left*) and π^- (*right*) production in $\bar{\nu}_\mu$ chains. The *bottom* row shows K^- (*left*) and K^0 (*right*) production in $\bar{\nu}_e$ chains. The distribution is broken down according to PPFX meson interaction categories. Five hues correspond to possible meson projectiles: π^+ (pink), π^- (gray), K^+ (green), K^- (teal) and K^0 (violet). Four shades of each color correspond to the x_F bins of the produced mesons, from 0–0.25 (the lightest) to 0.75–1 (the darkest).

- ν_μ:
  - projectiles producing K^+: K^+ (high x_F) and π^+ (low x_F)
  - projectiles producing π^+: π^+ (whole x_F range),
- ν_e:
  - projectiles producing K^+: K^+ (high x_F) and π^+ (low x_F),
  - projectiles producing K^0: K^0 (high x_F) and π^+ (low x_F),
- $\bar{\nu}_\mu$:
  - projectiles producing K^-: K^- (high x_F) but also $\pi^\pm$ and K^0,
  - projectiles producing π^-: π^- (whole x_F range), also π^+ (low x_F),
- $\bar{\nu}_e$:
  - projectiles producing K^-: K^- (high x_F),
  - projectiles producing K^0: K^0 (high x_F) and π^+ (low x_F).

Hadron production measurements of the interactions listed above would contribute the most to reducing the NuMI flux uncertainty at ICARUS.

The neutrino energy distributions of each PPFX meson interaction category are wide: most of the 20 colored bands cover the whole energy range in similar proportions. As each category corresponds to a single random weight in each universe, this means that each weight contributes to the whole neutrino energy range. This introduces correlation between neutrino energy bins. So while the bug fix significantly reduced correlations in neutrino energy, large correlations still exist.

B.4 Summary of parametrization of meson interactions in PPFX

As presently PPFX uses no experimental data on meson interactions, the related flux uncertainty is calculated based on a number of choices:

- The uncertainty of the hadron production cross section is assumed as 40 %. This value is chosen based on differences between measured and simulated cross sections [11, 12].
- In PPFX universes, the hadron production cross sections are randomly modified, with $\sigma = 40\%$, independently in 4 bins of x_F. This represents the uncertainty of the shape of the hadron production spectrum which is broadly correlated errors across neighboring regions of the $x_F - p_T$ phase space. This creates broad regions that are correlated internally, but not highly correlated with each other. The choice of relatively large bins reflects these observations.
  Figures B.3 and B.4 show that various x_F bins contribute similarly to the whole range of neutrino energy. The random weights from the x_F bins average out. Thus, the larger number of x_F bins is used, the lower is the flux uncertainty prediction. However, as shown in Fig. B.1, the majority of contributing hadrons is in 0–0.25, and 0.75–0 x_F bins. Effectively, only those two bins contribute to the neutrino flux.
- PPFX assumes no correlation between hadron production cross sections in any of the 35 combinations of the projectile and the produced particle.

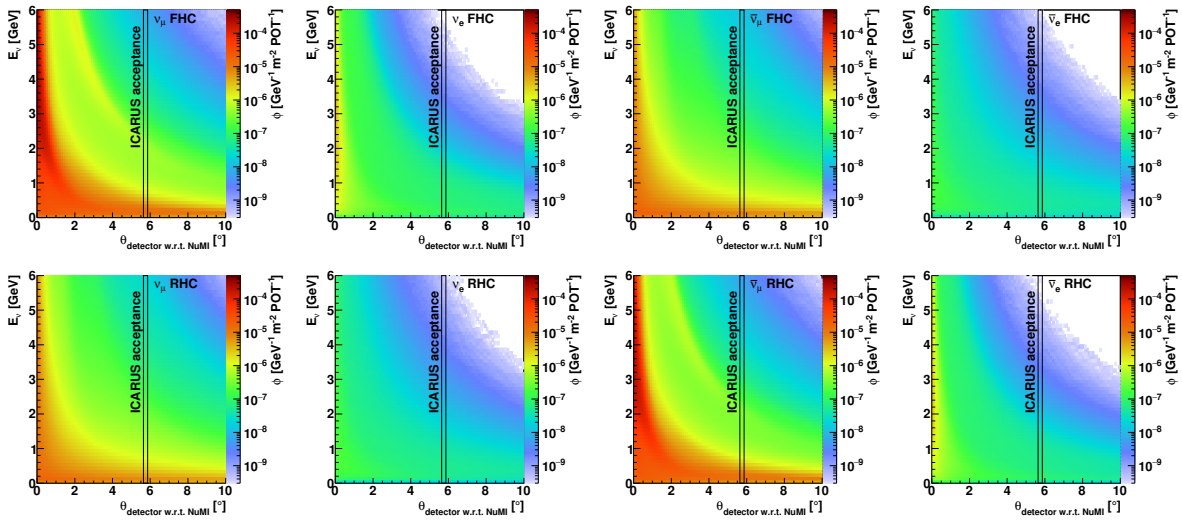

Figure C.1: Neutrino energy spectrum as a function of angle with respect to the NuMI beam axis, at the same distance (z coordinate) as ICARUS. Corresponding FHC neutrino plots are shown in Fig. 3.1.

While the choices are justified, the exact values are subjective, and affect the flux uncertainty prediction.

C Reverse Horn Current Plots for the NuMI Beam at ICARUS

This section presents additional variations of plots presented in Sec. 3, primarily for antineutrinos and reverse horn current.

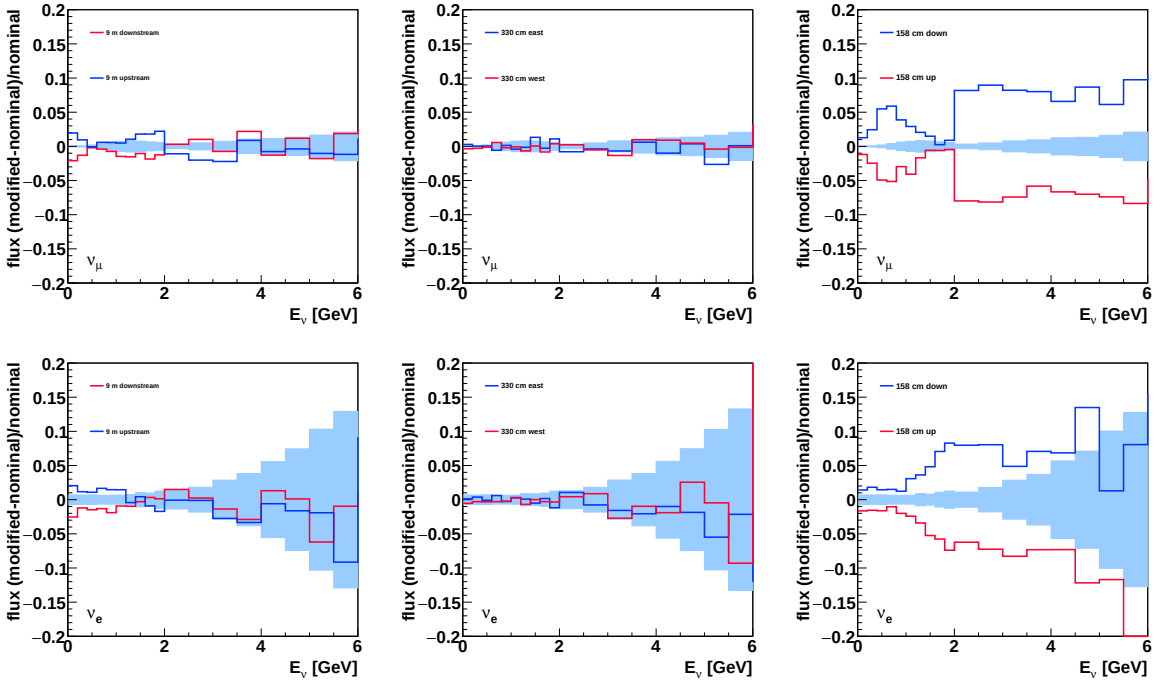

Figure C.2: Flux in ICARUS TPCs changes by ±10% along the vertical axis, and 2% along the horizontal axes. The blue band shows the statistical uncertainty. See Fig. 3.3.

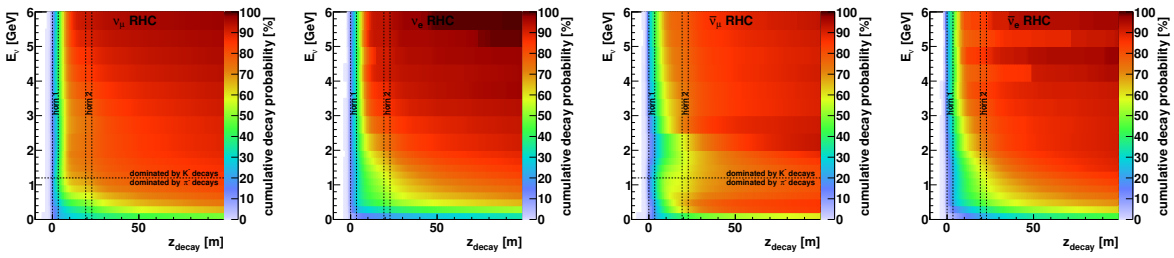

Figure C.3: Cumulative probability for a parent of a neutrino to decay along the beam line for various energy ranges. Vertical dashed lines mark horn positions. Horizontal dashed lines in ν_e figures separate the low energy neutrinos originating mostly from $\pi^{\pm}$ decays and high energy ones originating from $K^{\pm}$ decays. FHC plots can be found in Fig. 3.4

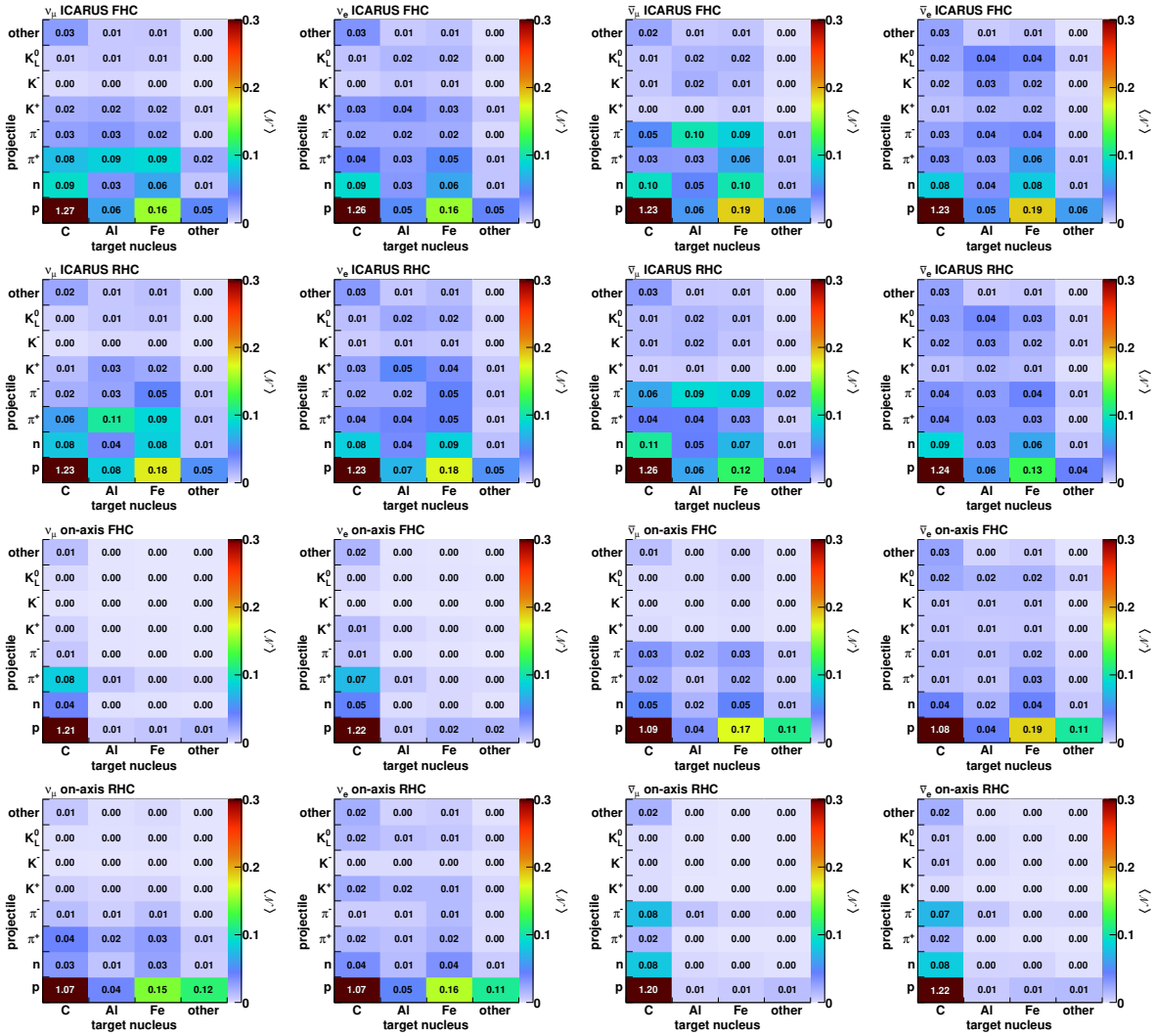

Figure C.4: Distribution of number of interactions $\langle \mathcal{N} \rangle$ of various projectiles on various nuclei leading to neutrino flux generation. These plots complement Fig. 3.9.

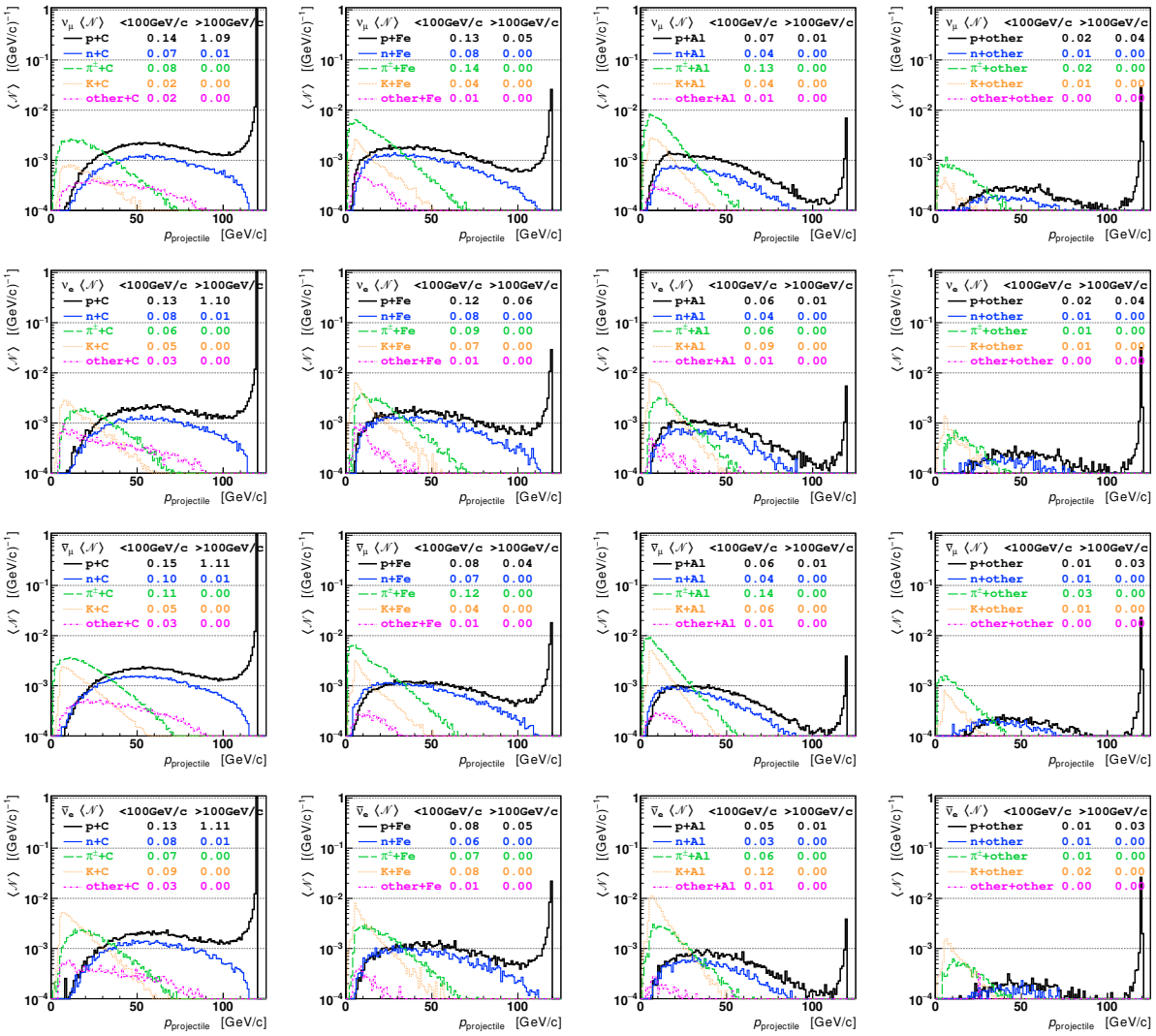

Figure C.5: Momentum distributions of hadron ancestors interactions contributing to NuMI flux in ICARUS. *Rows (top to bottom)*: ν_μ, ν_e, $\bar{\nu}_\mu$, $\bar{\nu}_e$. *Columns (left to right)*: target C, Fe, Al and other materials. Colored lines distinguish hadron projectiles: p (thick black), n (solid blue), $\pi^\pm$ (dashed green), K (dotted orange) and other (dash-dotted magenta). Legend shows the number of interactions per neutrino ($\langle\mathcal{N}\rangle$) integrated separately below and above 100 GeV/c. Only neutrinos with $E_\nu > 400$ MeV are plotted. The plots complement Fig. 3.10.

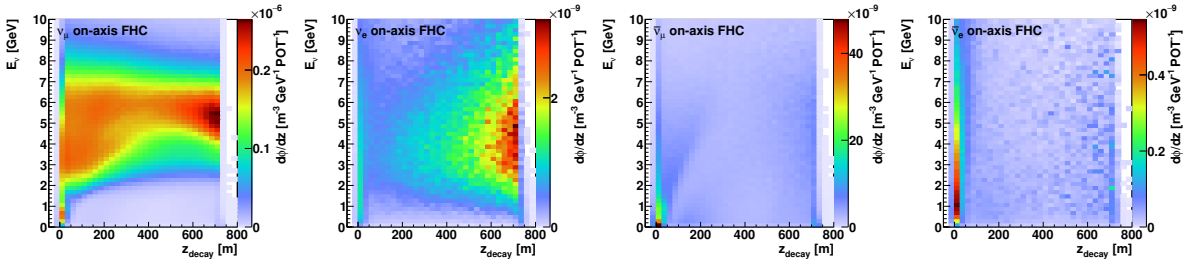

Figure C.6: Distribution of neutrino energy as a function of the decay position along the NuMI beam line. These plots complement Fig. 3.12.

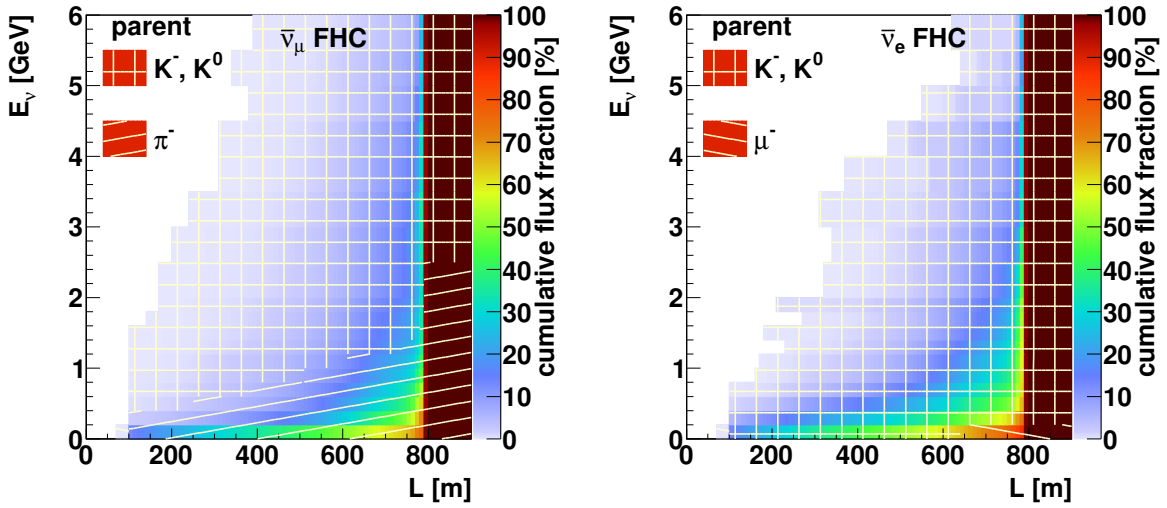

Figure C.7: Distribution of neutrino energy as a function of neutrino flight path from the decay point to the geometrical center of ICARUS, for $\bar{\nu}_\mu$ (*left*) and $\bar{\nu}_e$ (*right*). The plots are cumulative along the horizontal axis, and normalized to 100% in each E_ν bin. The baseline of 100 m corresponds to decays in the beam dump, and 800 m to the target area. The hatched areas show the identity of neutrino parent particles contributing the most to the cumulative distribution in those bins. Corresponding neutrino plots can be found in Fig. 3.14.

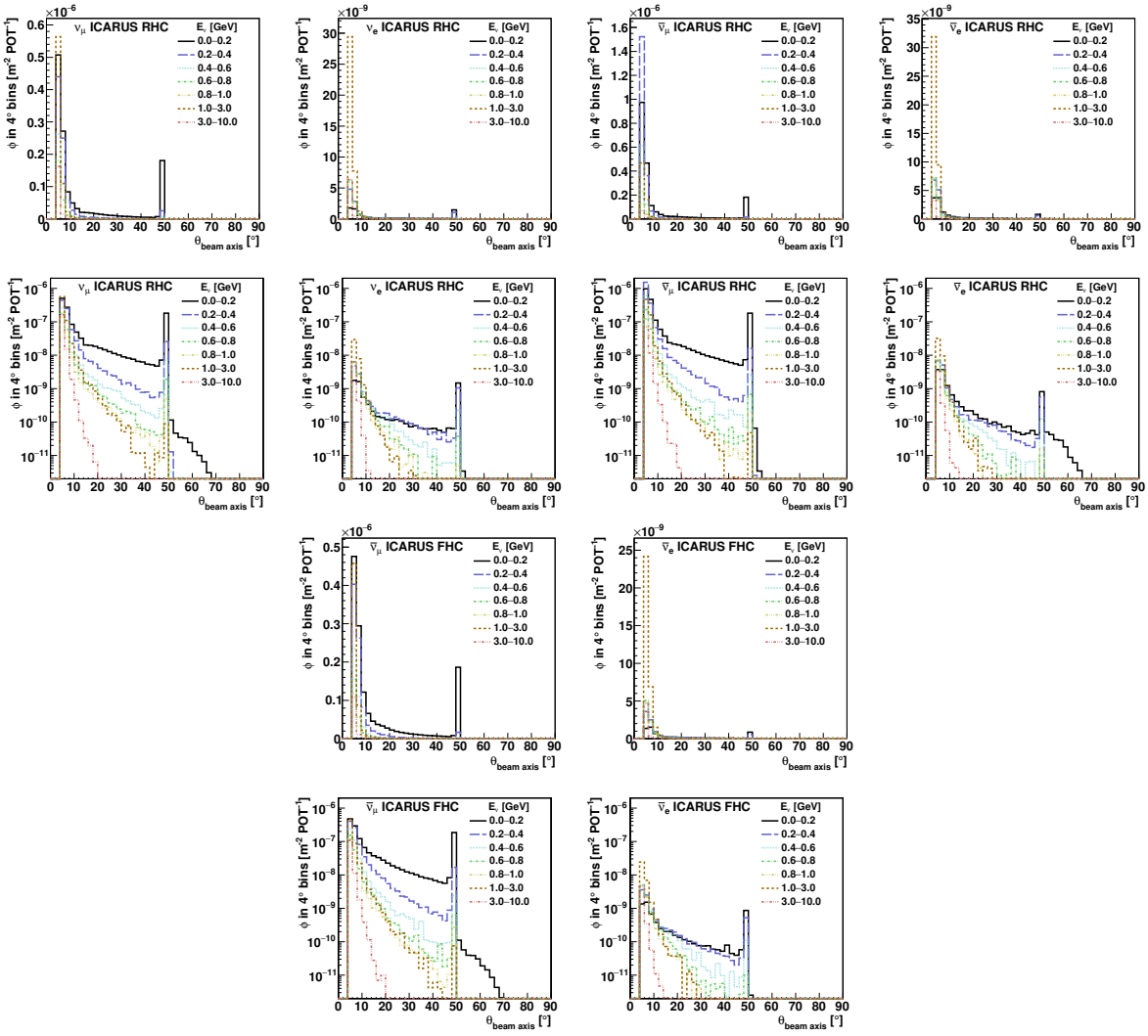

Figure C.8: Distribution of neutrino angle w.r.t. the NuMI beam axis. The plots complement Fig. 3.16.

D Effects Due to the Earth's Magnetic Field

In the datasets used in the main body of this note, the Earth's Magnetic field was disabled. In order to study its impact on the flux, several additional datasets with realistic and exaggerated values of the field in the decay pipe [32] were analyzed.

Figure D.1 shows a comparison of flux predicted with various Earth magnetic field settings. The differences seem consistent with statistical uncertainty. The magnetic field affects the longest hadron tracks passing through the whole length of the decay pipe. As shown in Sec. 3.6, the majority of neutrinos traveling to ICARUS originate

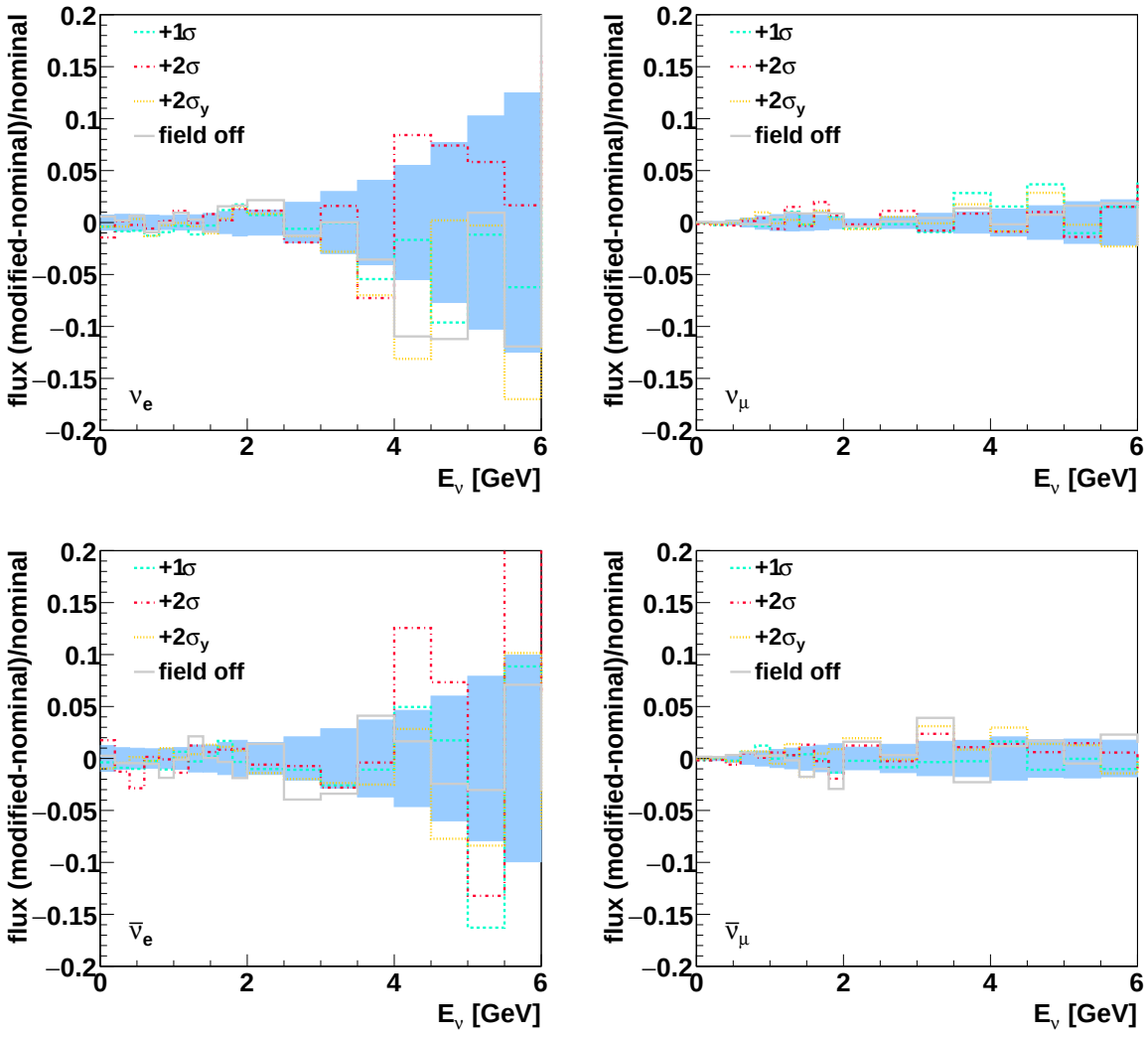

Figure D.1: Ratio of flux simulated with exaggerated Earth magnetic field and disabled field to the flux simulated with the nominal Earth field $(0.1, -0.3, -0.07) \pm 0.10$ G for ν_e (*top left)* and ν_μ (*top right*) and corresponding anti-neutrinos (*bottom*). The blue band shows statistical uncertainty.

from decays in the upstream part of the decay pipe. As the path travelled by the parent hadrons is very short, they are not affected significantly by the Earth's magnetic field.

E Uncertainty Propagation

The energy-averaged interaction cross-section can be measured as

$$\sigma_x = \frac{N^x_{\text{int}} - B^x}{\varepsilon^x M} \cdot \frac{1}{\sum_{i=1}^{n} \phi^x_i} = \frac{N^x_{\text{int}} - B^x}{\varepsilon^x M \Phi_x}, \tag{E.1}$$

where

- N^x_{int} is the measured number of interactions for neutrino ν_x,
- B^x is the predicted number of background events,
- ε^x is the exposure measured in POT,
- M is the detector mass (number of targets),
- ϕ^x_i is the predicted flux of neutrino ν_x, expressed in $\text{m}^{-2}\text{POT}^{-1}$, in energy bin i, out of total n bins,
- $\Phi_x \equiv \sum_{i=1}^{n} \phi^x_i$ is the flux integrated over energy.

The ratio of cross-sections of two neutrinos ν_x and ν_y is:

$$R_{xy} = \frac{\sigma_x}{\sigma_y} = \frac{N^x_{\text{int}}}{N^y_{\text{int}}} \cdot \frac{\varepsilon^y}{\varepsilon^x} \cdot \frac{\Phi_y}{\Phi_x}, \tag{E.2}$$

where the ratio $\varepsilon^y/\varepsilon^x$ may not equal 1 if measurements of ν_x and ν_y come from different data sets (e.g. forward and reversed horn current runs).

Partial derivatives of R are

$$\frac{\partial R}{\partial \phi^x_k} = -\frac{R}{\Phi_x}; \quad \frac{\partial R}{\partial \phi^y_k} = \frac{R}{\Phi_y}. \tag{E.3}$$

Following the uncertainty propagation formula yields

$$\begin{aligned} \delta^2_R &= \sum_{i=1}^{n}\sum_{j=1}^{n}\left[\frac{\partial R}{\partial \phi^x_i}\frac{\partial R}{\partial \phi^x_j}\text{cov}_{\phi^x_i\phi^x_j} + \frac{\partial R}{\partial \phi^y_i}\frac{\partial R}{\partial \phi^y_j}\text{cov}_{\phi^y_i\phi^y_j} + 2\frac{\partial R}{\partial \phi^x_i}\frac{\partial R}{\partial \phi^y_j}\text{cov}_{\phi^x_i\phi^y_j}\right] \\ &= R^2 \cdot \sum_{i=1}^{n}\sum_{j=1}^{n}\left[\frac{1}{\Phi^2_y}\cdot\text{cov}_{\phi^x_i\phi^x_j} + \frac{1}{\Phi^2_x}\cdot\text{cov}_{\phi^y_i\phi^y_j} - \frac{2}{\Phi_x\Phi_y}\cdot\text{cov}_{\phi^x_i\phi^y_j}\right], \end{aligned} \tag{E.4}$$

where $\text{cov}_{\phi^x_i\phi^y_j}$ is covariance between fluxes ϕ^x and ϕ^y in energy bins i and j. Refer to Eq. 4.4 for more information. As the last term in the formula has negative sign, positive covariance decreases the total uncertainty.

F PPFX Universe Normality Study

F.1 Forward Horn Current

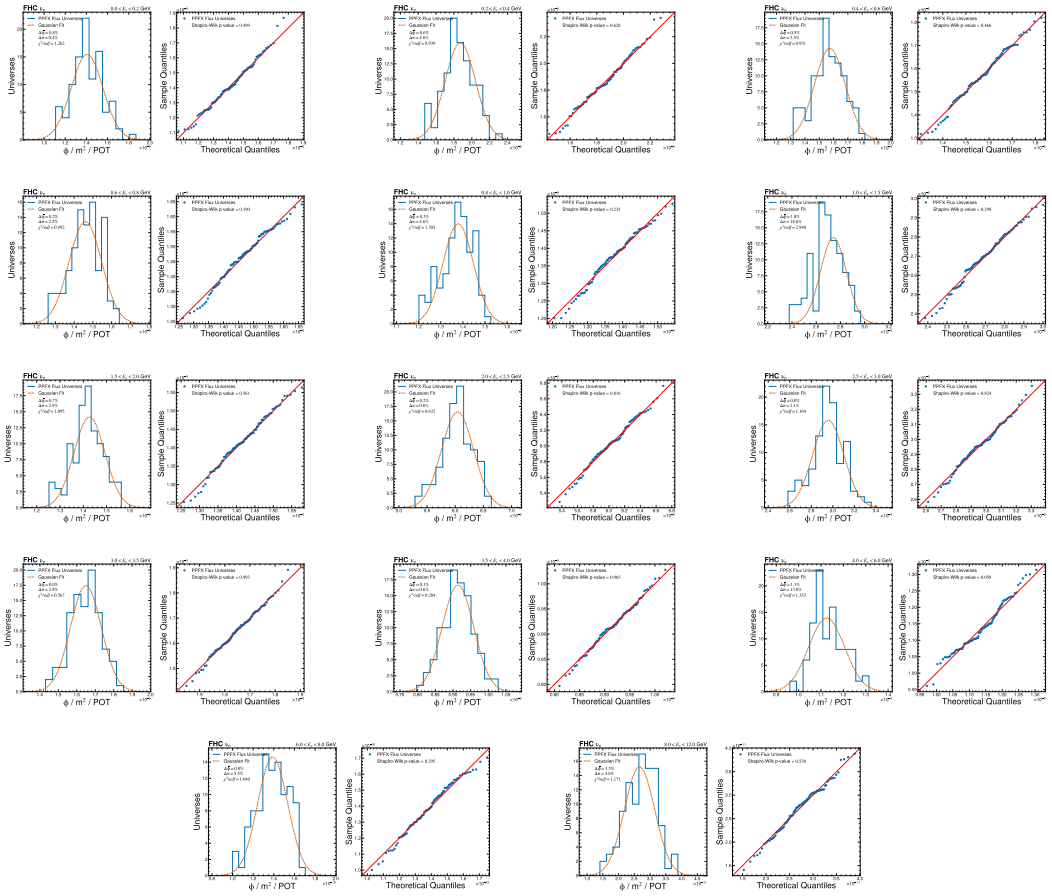

Figure F.1: Distribution of PPFX universes for ν_e.

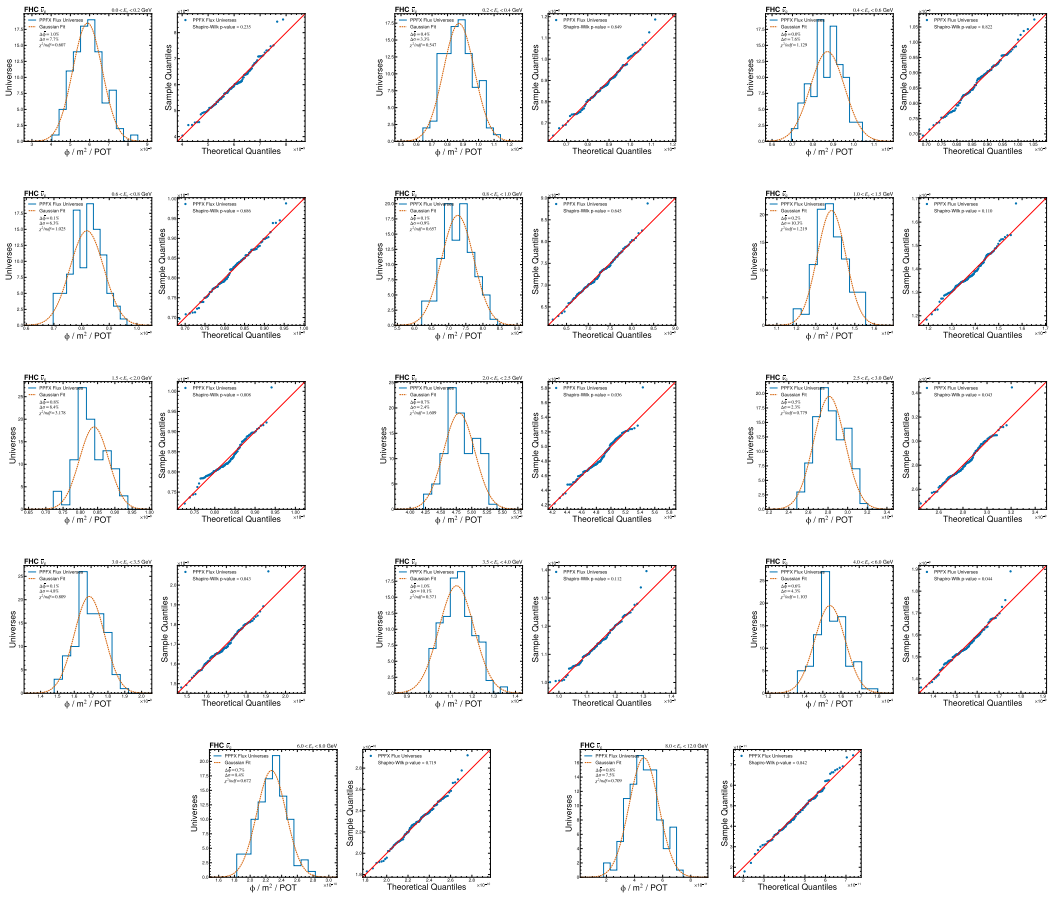

Figure F.2: Distribution of PPFX universes for $\bar{\nu}_e$.

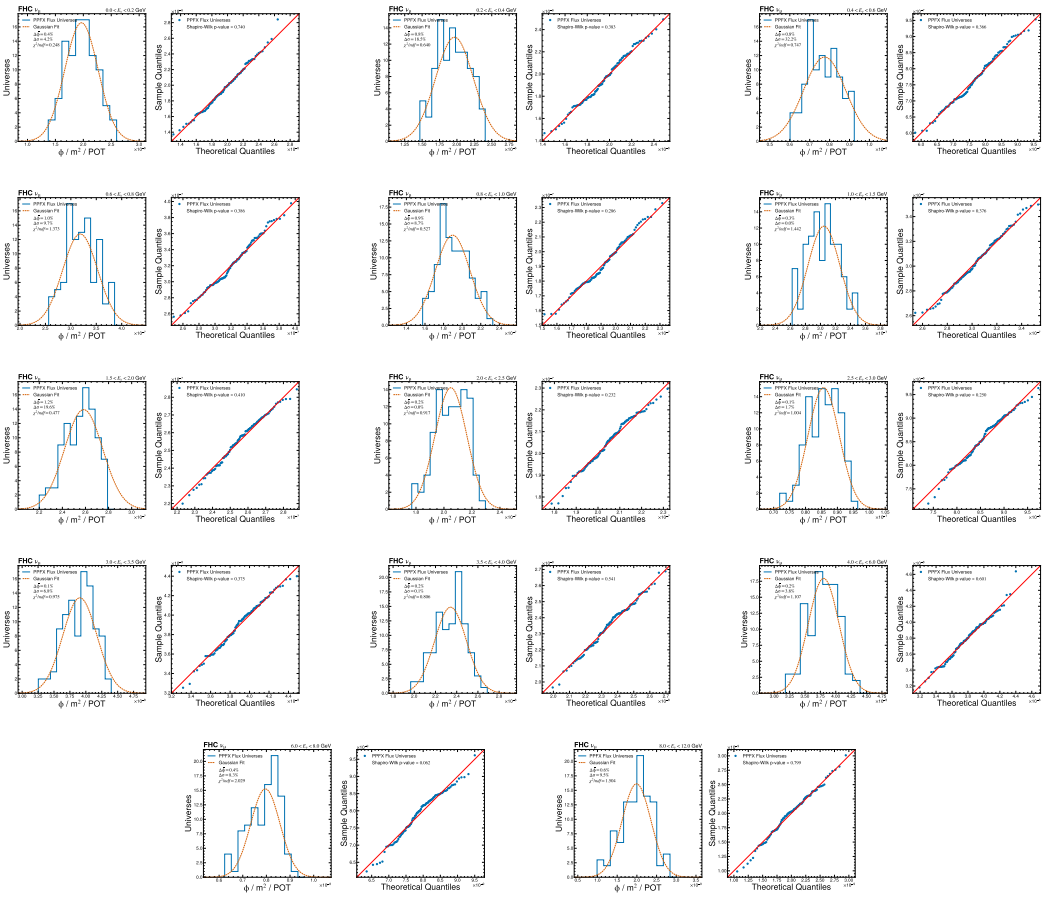

Figure F.3: Distribution of PPFX universes for ν_μ.

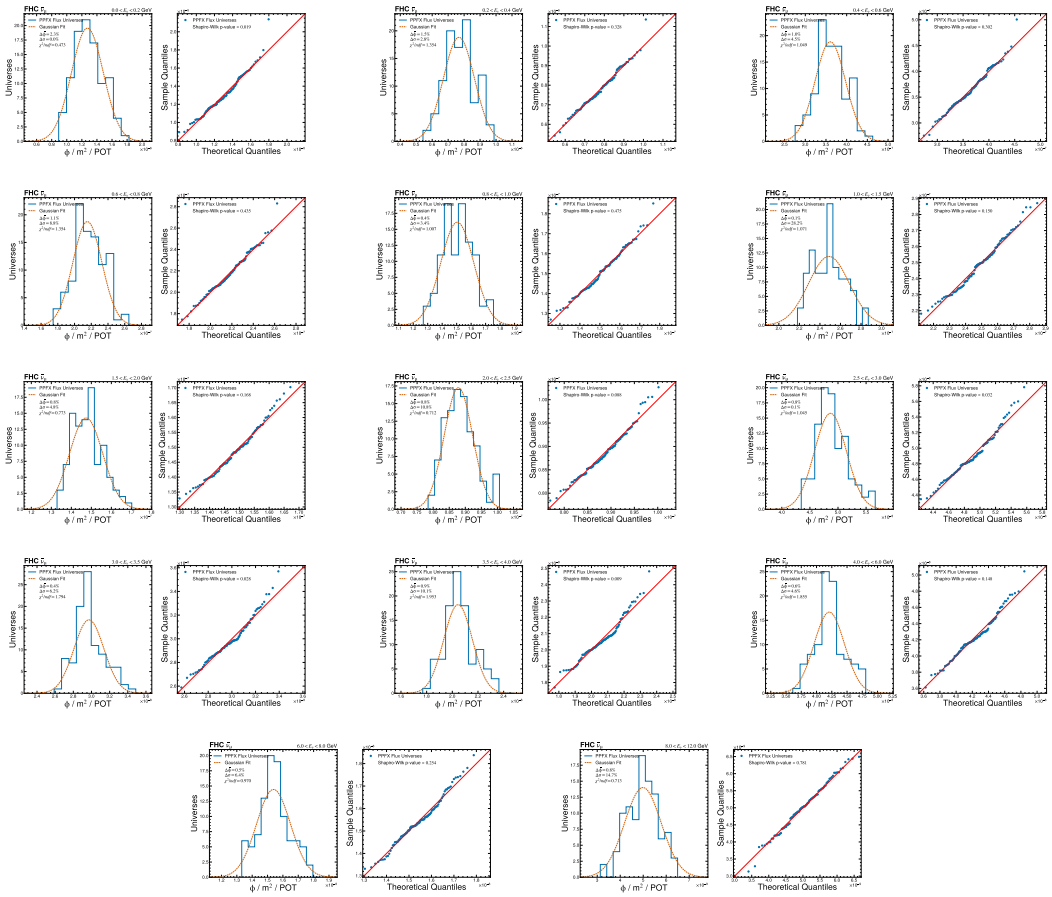

Figure F.4: Distribution of PPFX universes for $\bar{\nu}_\mu$.

F.2 Reverse Horn Current

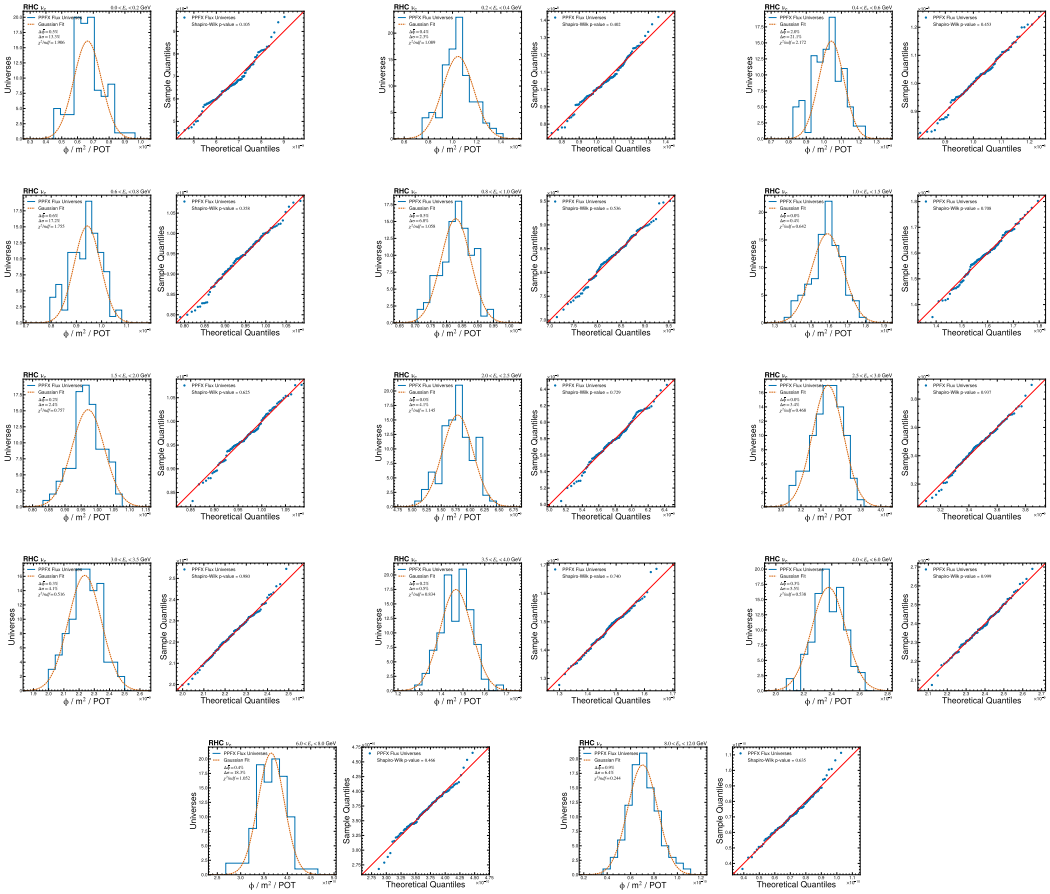

Figure F.5: Distribution of PPFX universes for ν_e.

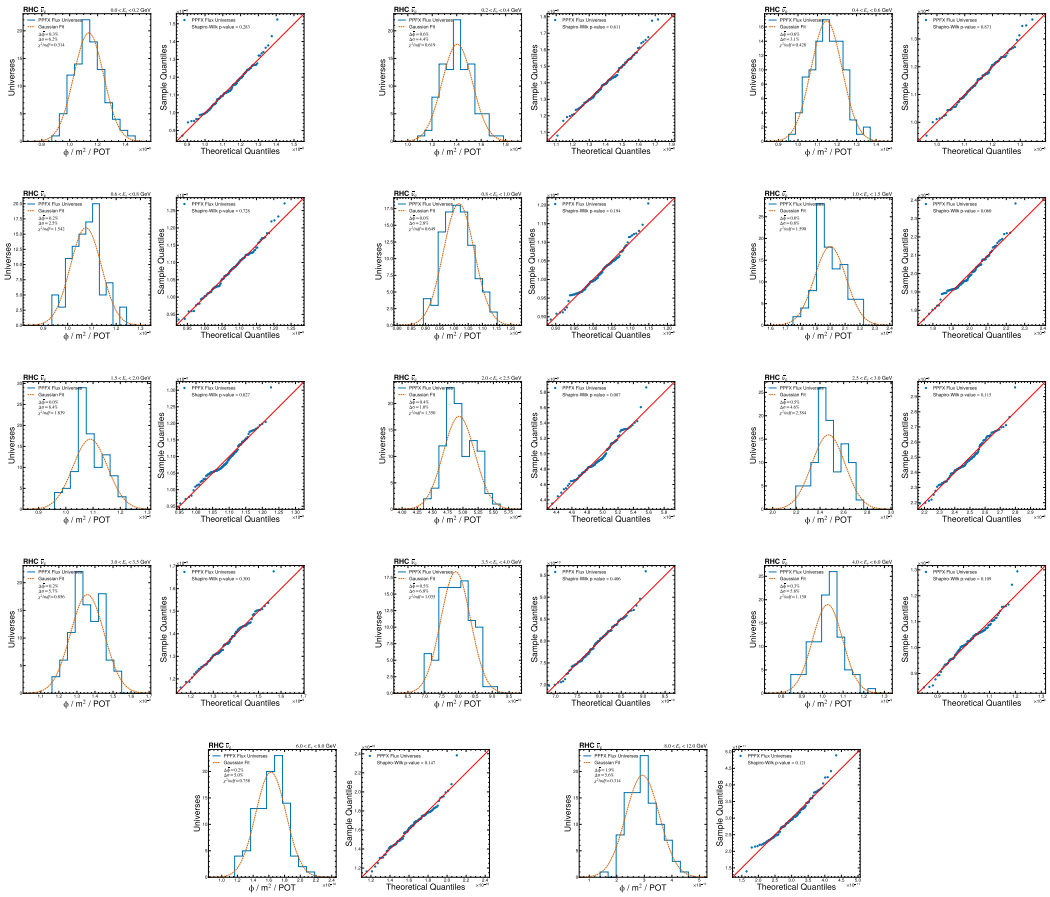

Figure F.6: Distribution of PPFX universes for $\bar{\nu}_e$.

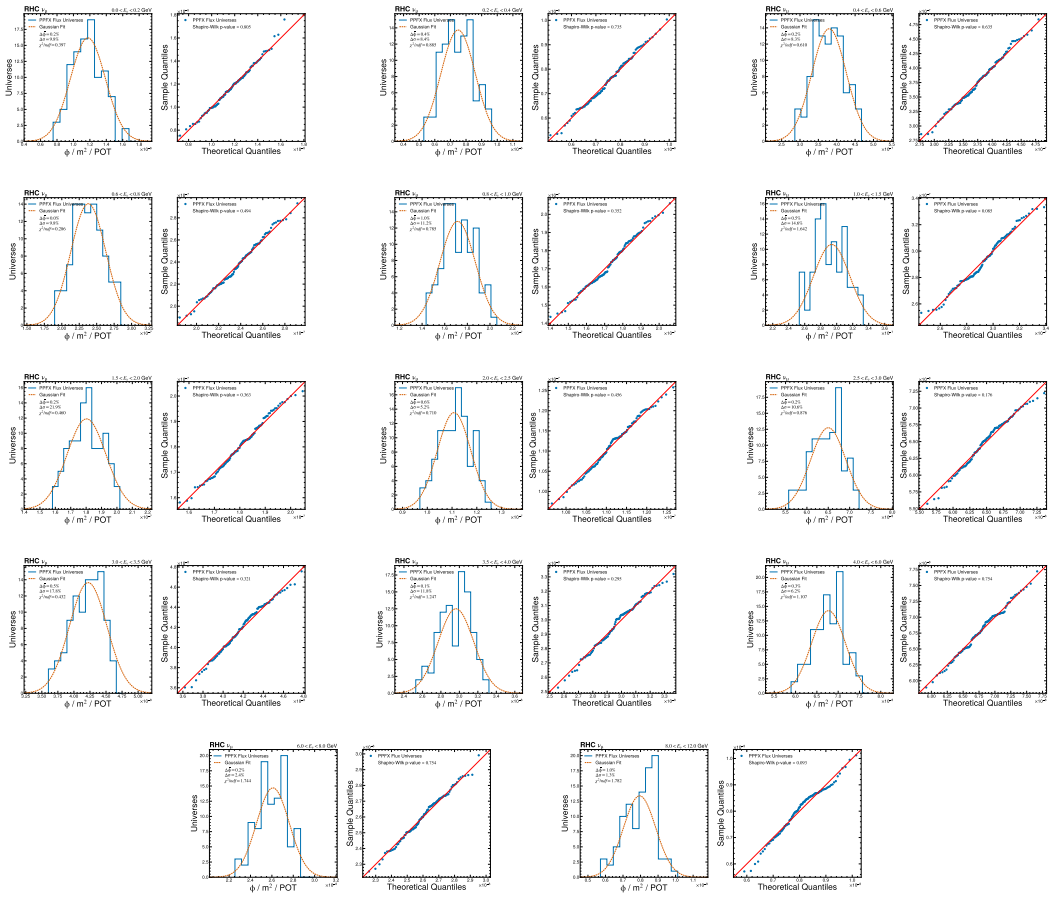

Figure F.7: Distribution of PPFX universes for ν_μ.

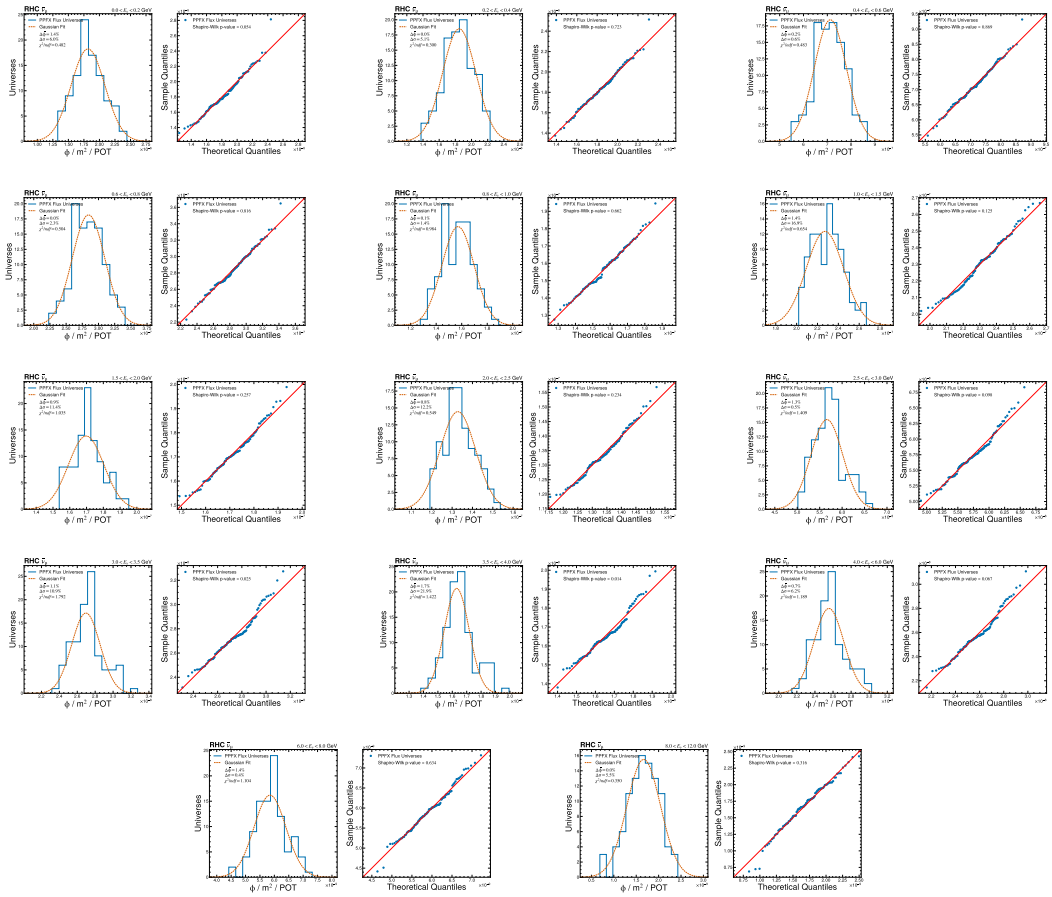

Figure F.8: Distribution of PPFX universes for $\bar{\nu}_\mu$.

G Hadron Production Matrices

G.1 Covariance Matrices

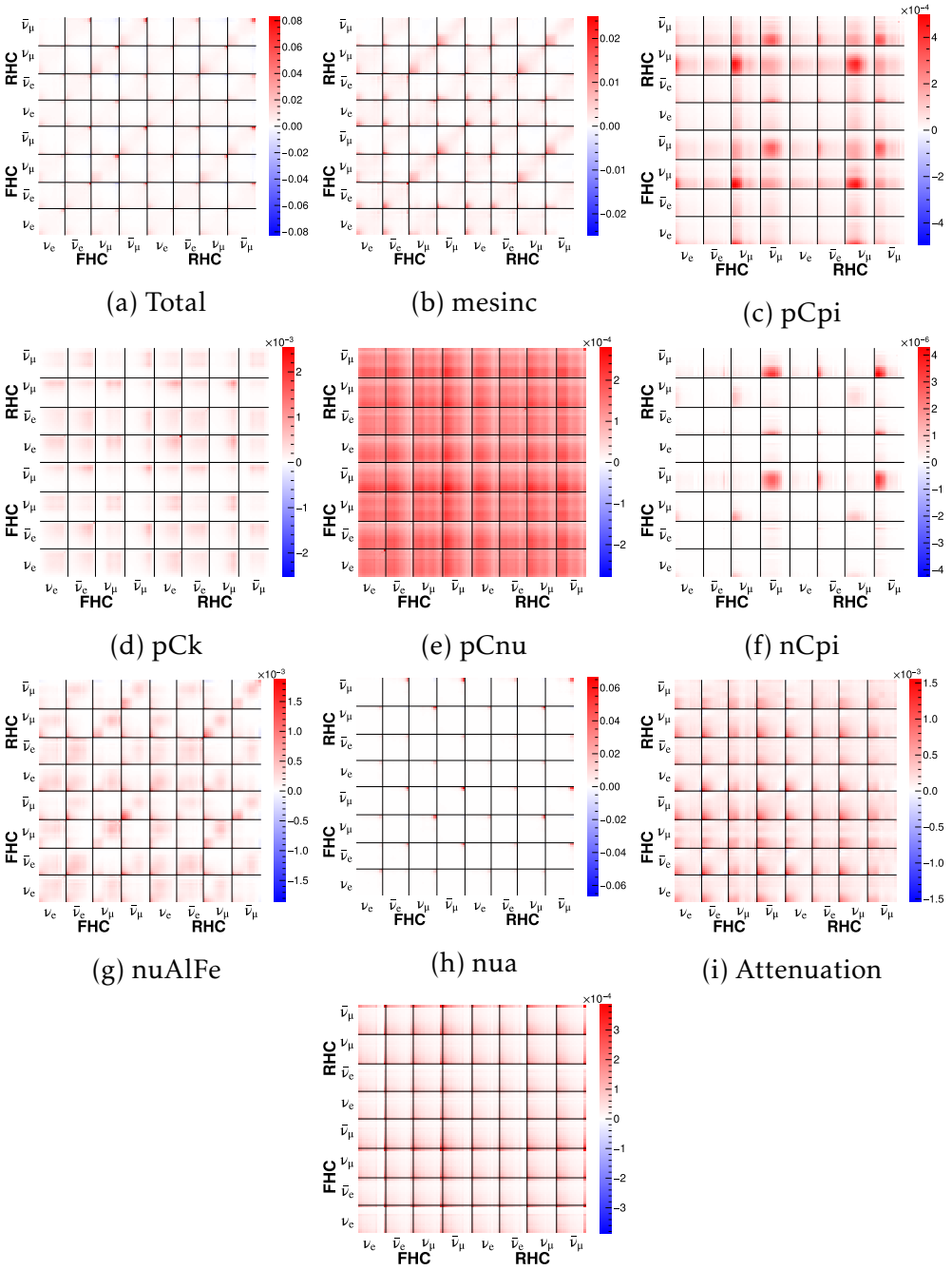

(a) Total (b) mesinc (c) pCpi

(d) pCk (e) pCnu (f) nCpi

(g) nuAlFe (h) nua (i) Attenuation

(j) Others

Figure G.1: All hadron production covariance matrices.

G.2 Correlation Matrices

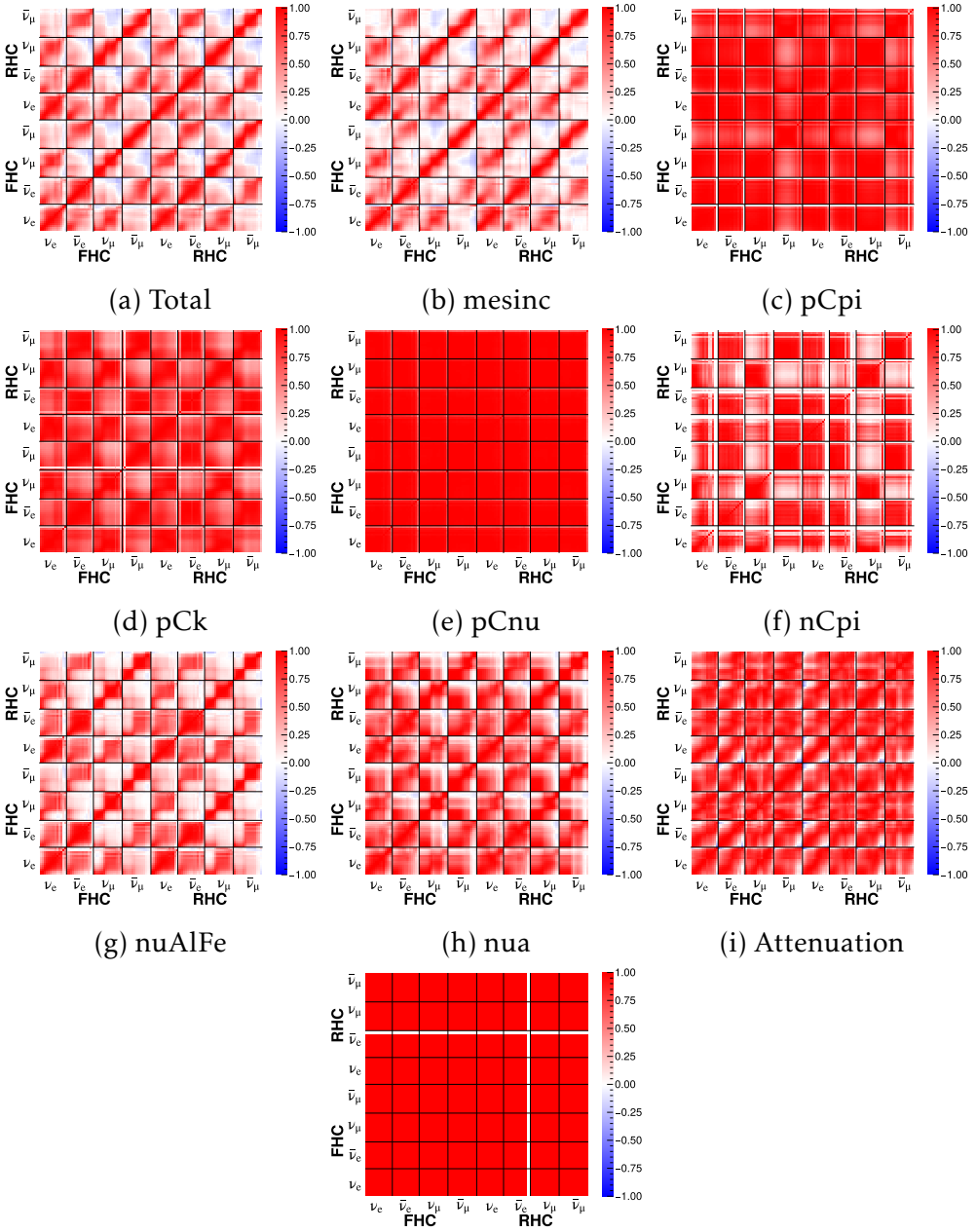

(a) Total (b) mesinc (c) pCpi

(d) pCk (e) pCnu (f) nCpi

(g) nuAlFe (h) nua (i) Attenuation

(j) Others

Figure G.2: All hadron production correlation matrices.

H Hadron Production Systematic Uncertainties

H.1 Forward Horn Current

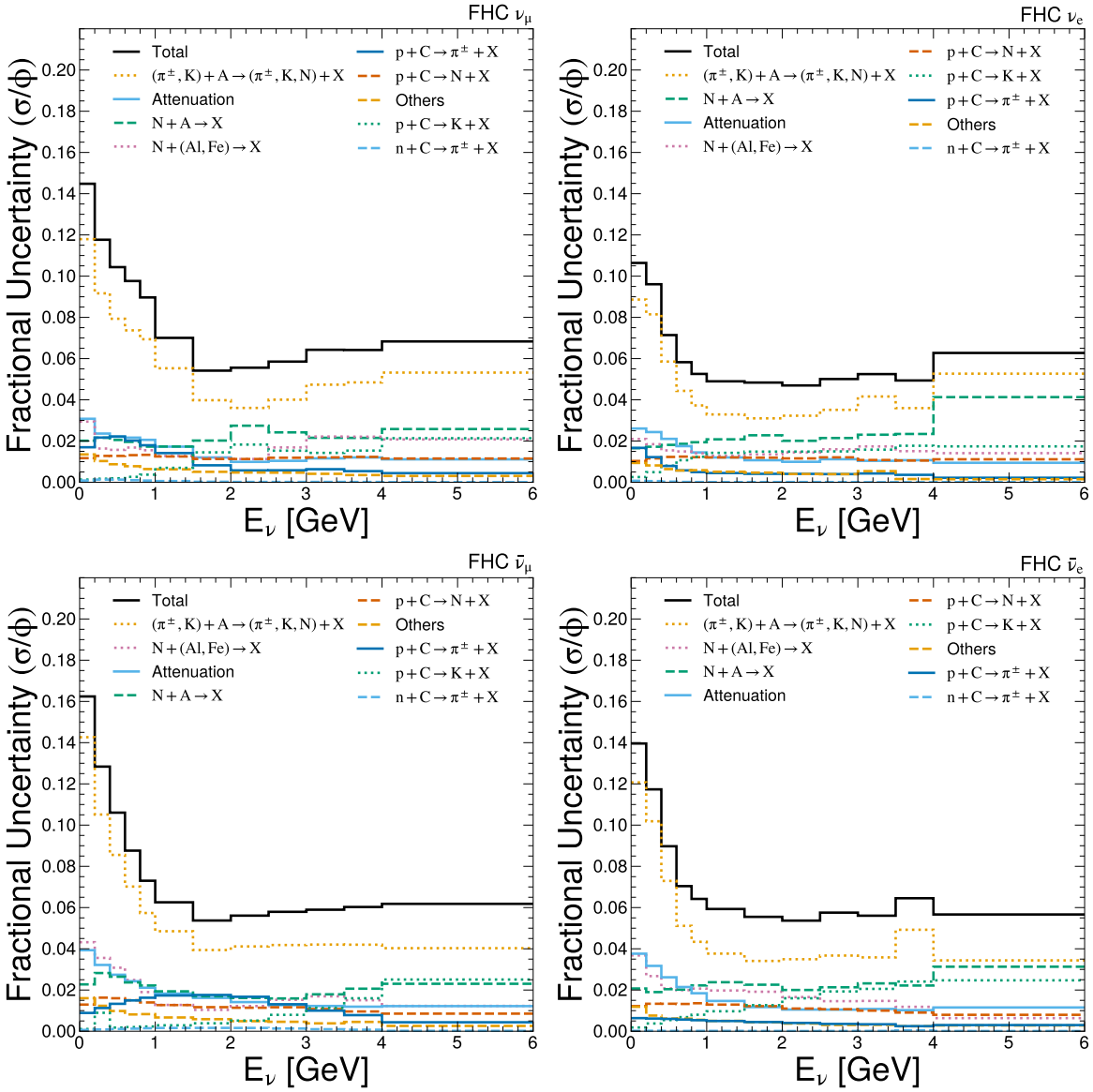

Figure H.1: Hadron interaction systematic uncertainties for all neutrino modes in the forward horn current beam configuration.

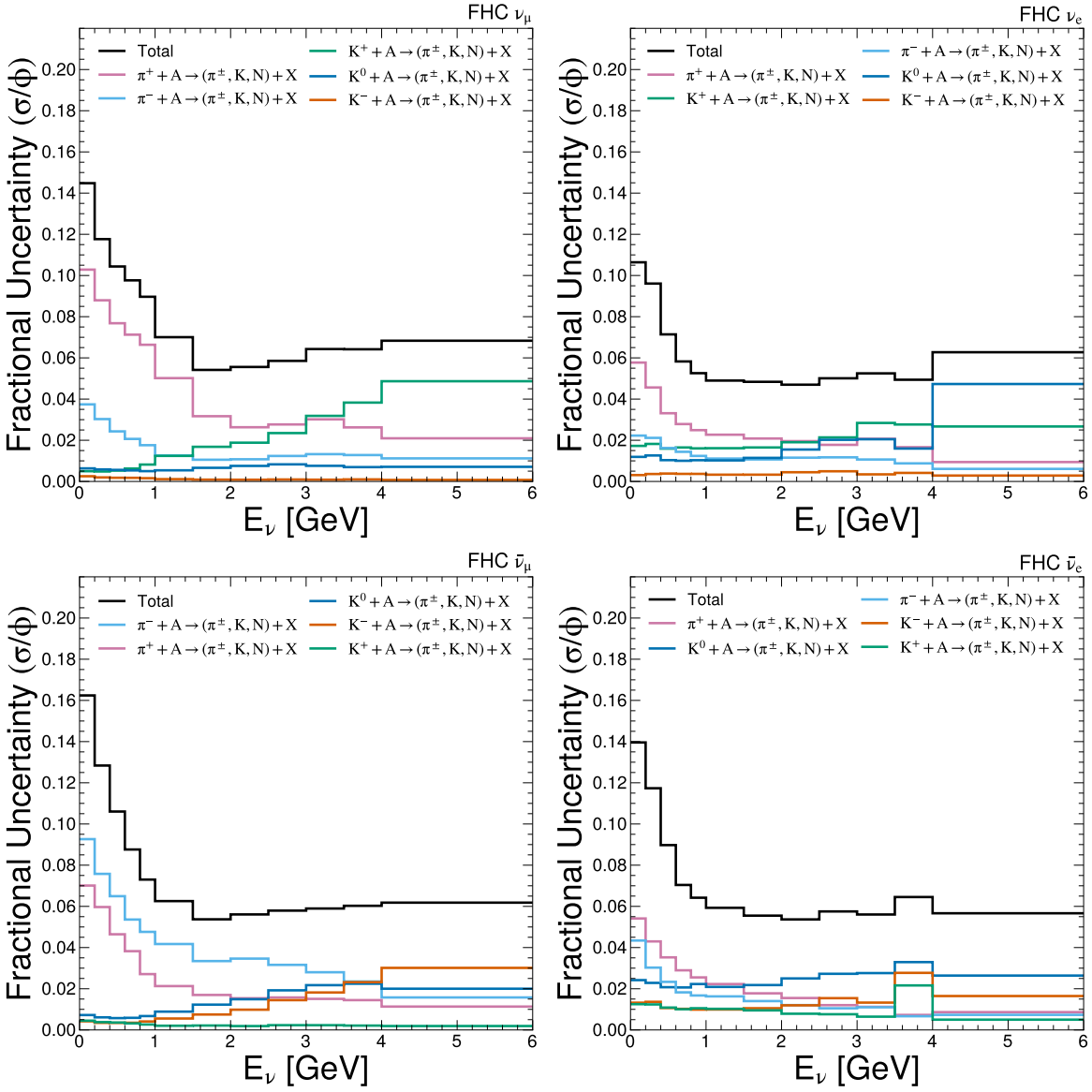

Figure H.2: Contribution to the uncertainty by incoming meson.

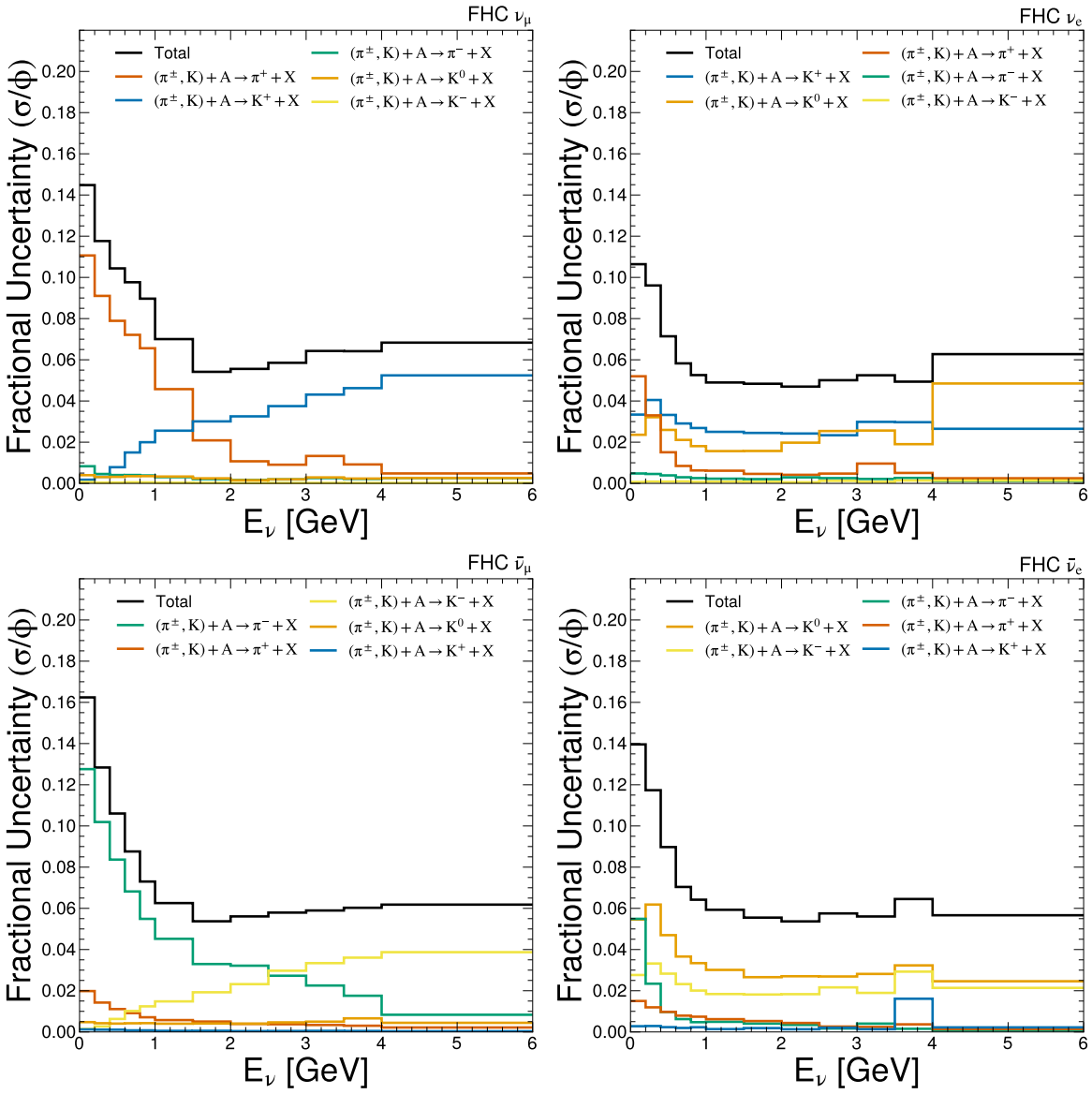

Figure H.3: Contribution to the uncertainty by outgoing meson.

H.2 Reverse Horn Current

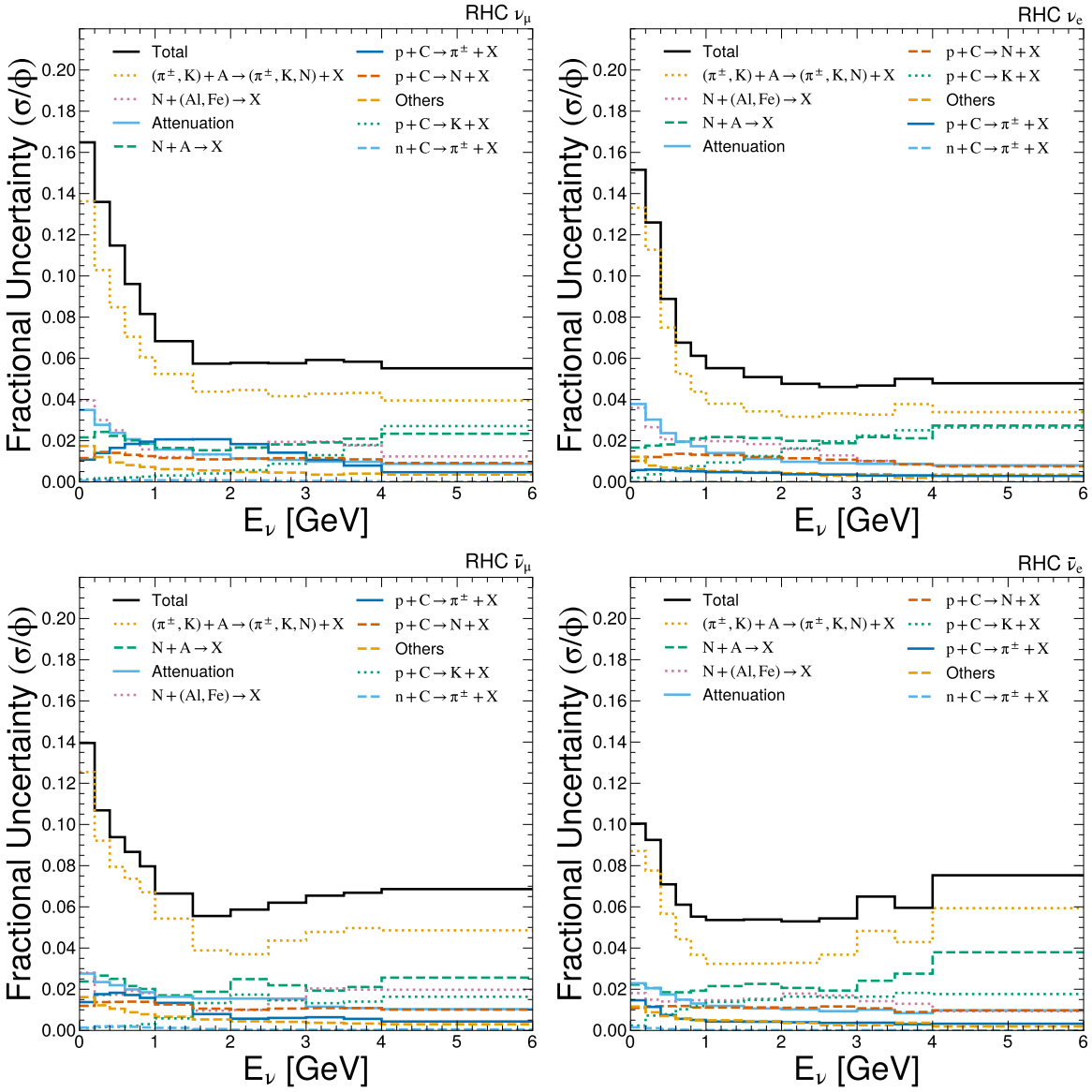

Figure H.4: Hadron interaction systematic uncertainties for all neutrino modes in the forward horn current beam configuration.

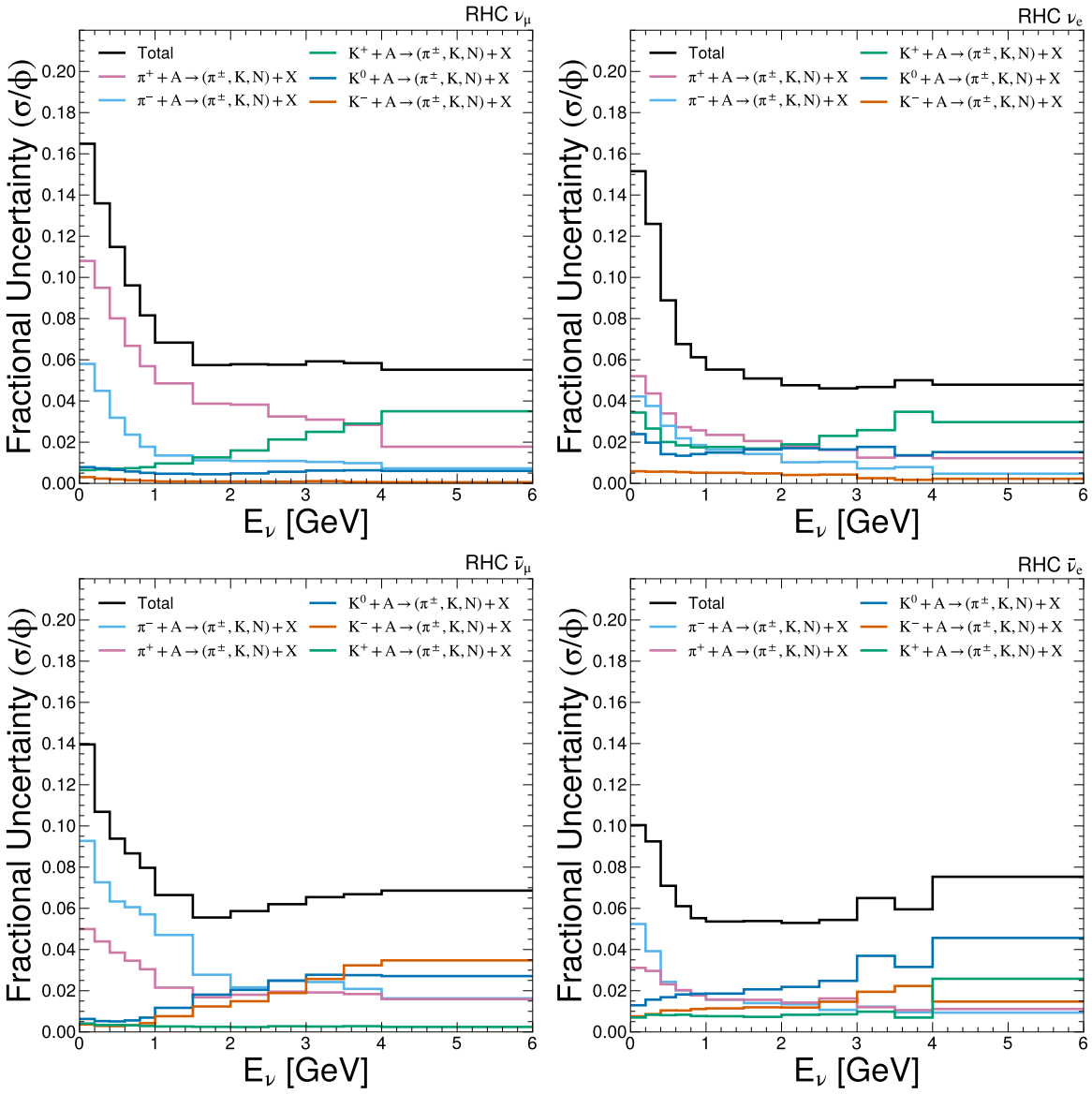

Figure H.5: Contribution to the uncertainty by incoming meson.

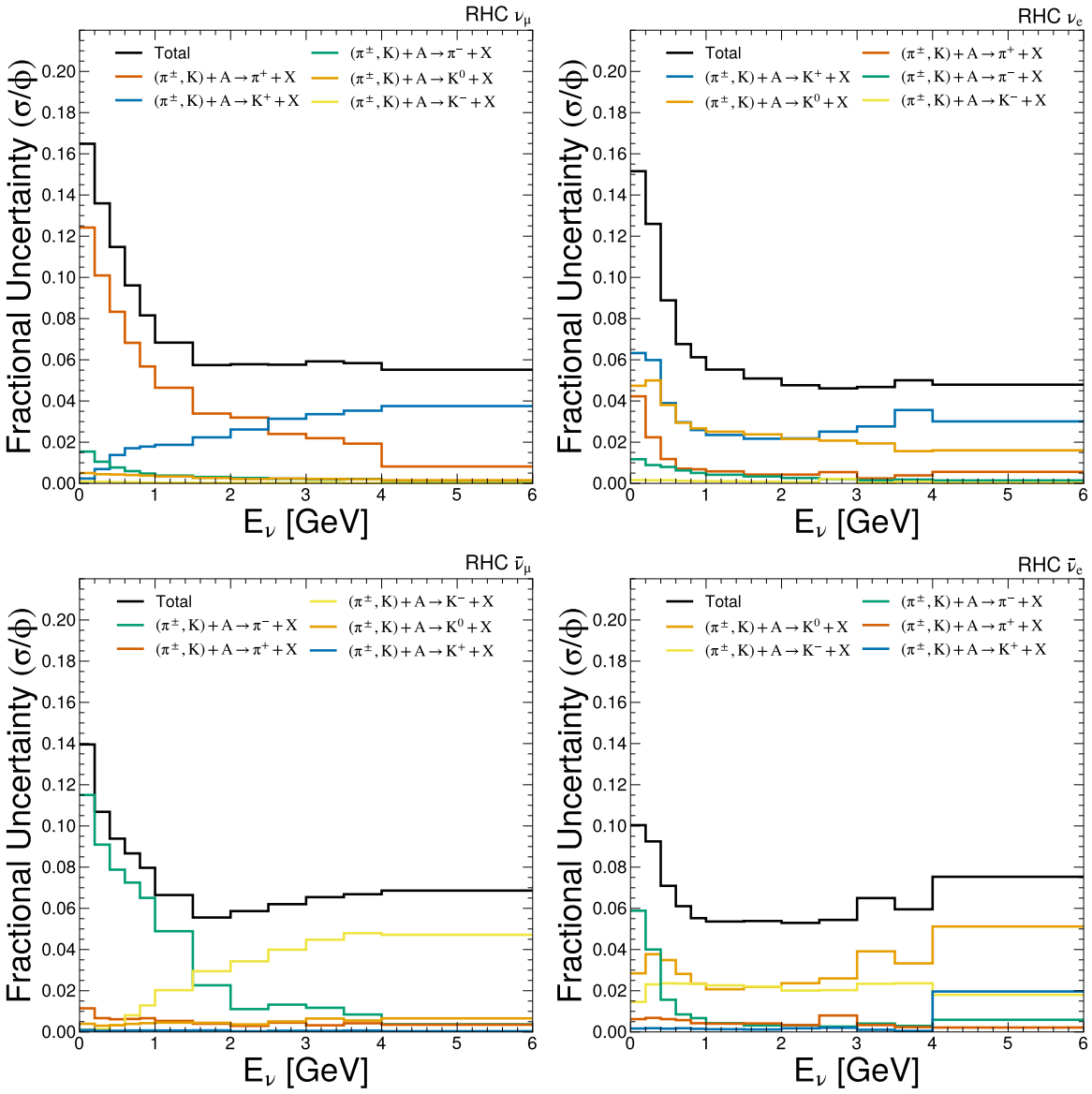

Figure H.6: Contribution to the uncertainty by outgoing meson.

I PCA

I.1 Top Four Principal Components

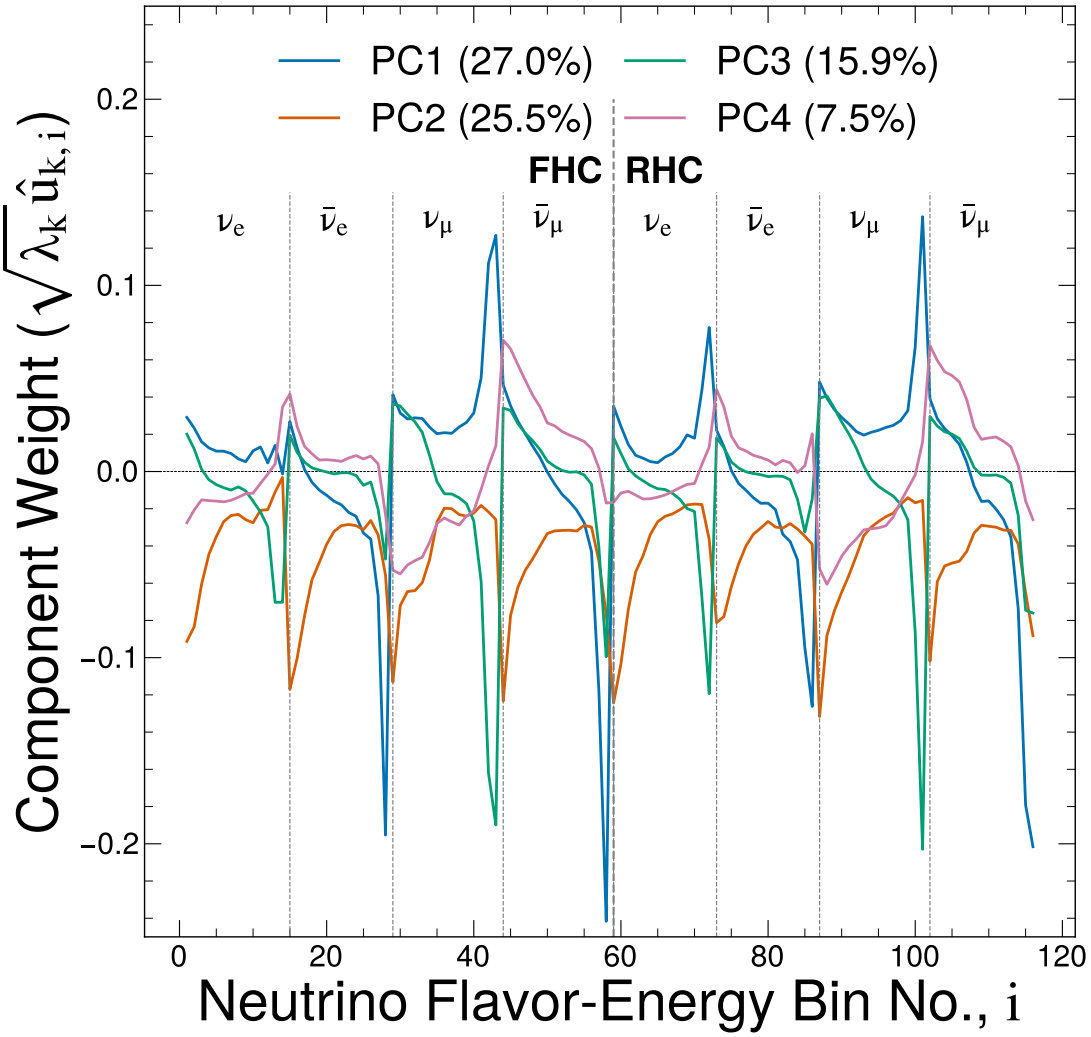

Figure I.1: The top four principal components with the largest contributions to the total variance of the Hadron Production Covariance Matrix. The first two PCs contribute comparable amounts to the total variance, with PC1 describing more of the uncertainty in the HE flux tail, and PC2 the LE regions of the flux.

I.2 Physics vs. PCA Variance Comparison

I.2.1 Forward Horn Current

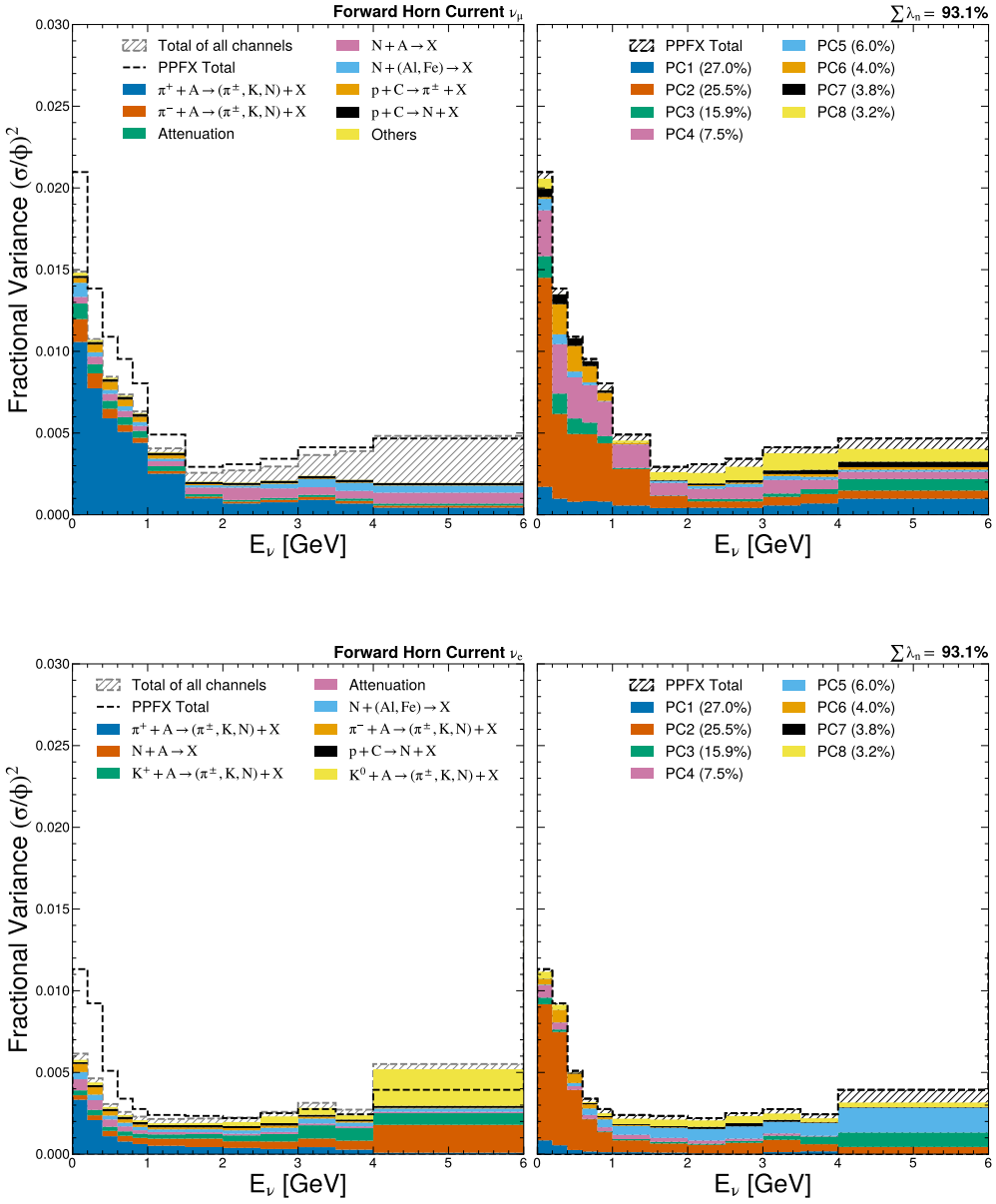

Figure I.2: Fractional variance comparison between physics and PCA descriptions by incoming meson (FHC, ν).

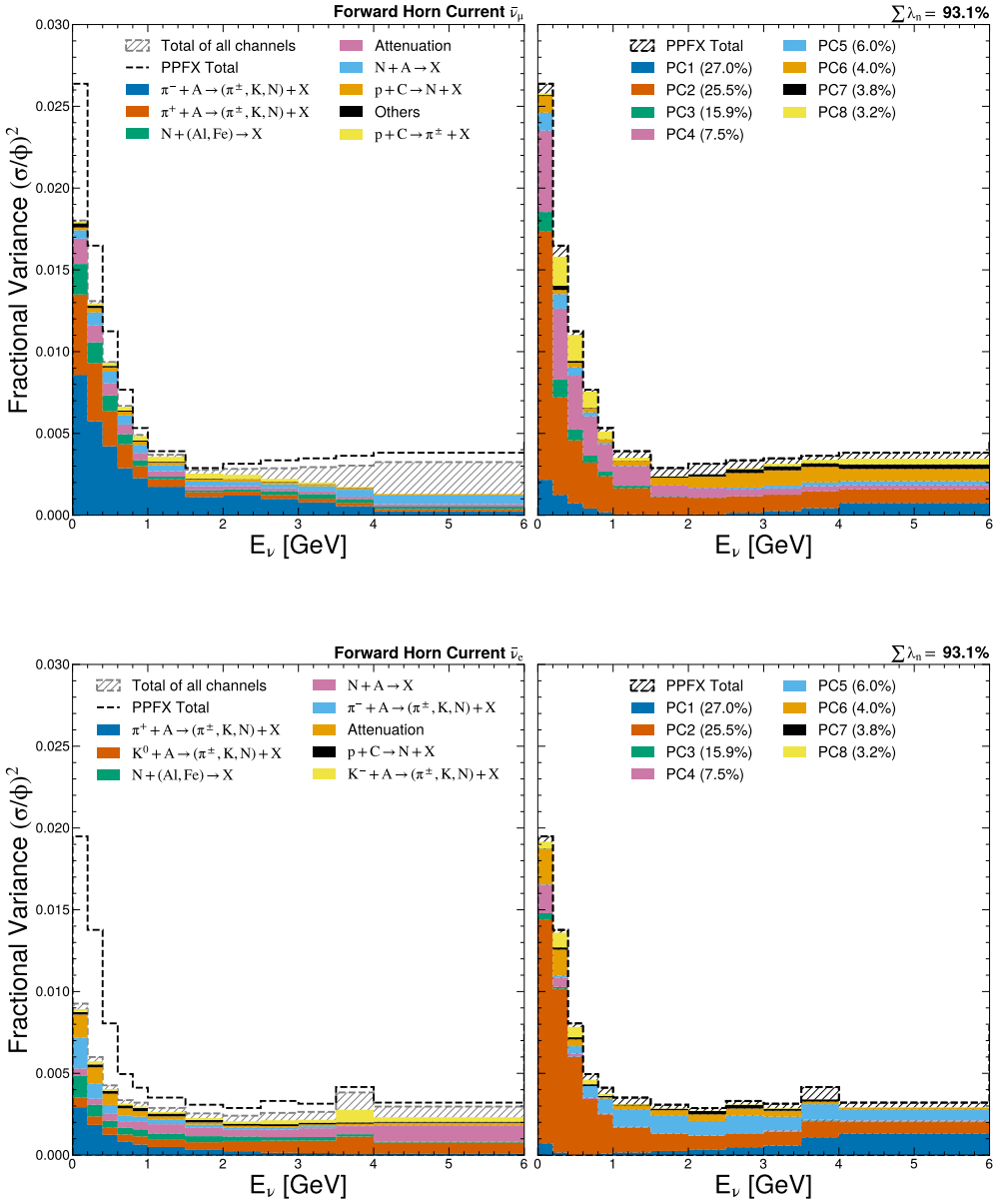

Figure I.3: Fractional variance comparison between physics and PCA descriptions by incoming meson (FHC, $\bar{\nu}$).

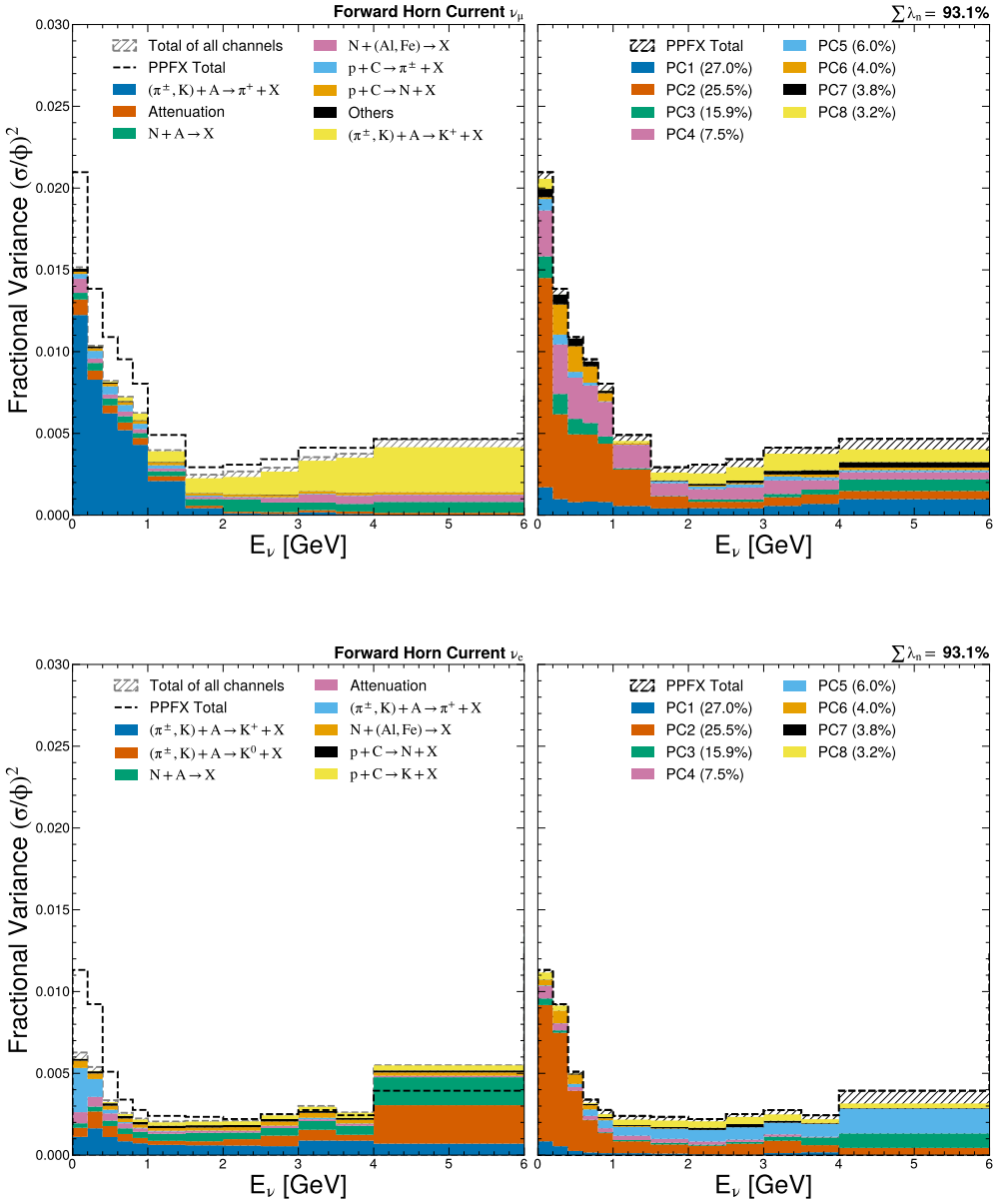

Figure I.4: Fractional variance comparison between physics and PCA descriptions by outgoing meson (FHC, ν).

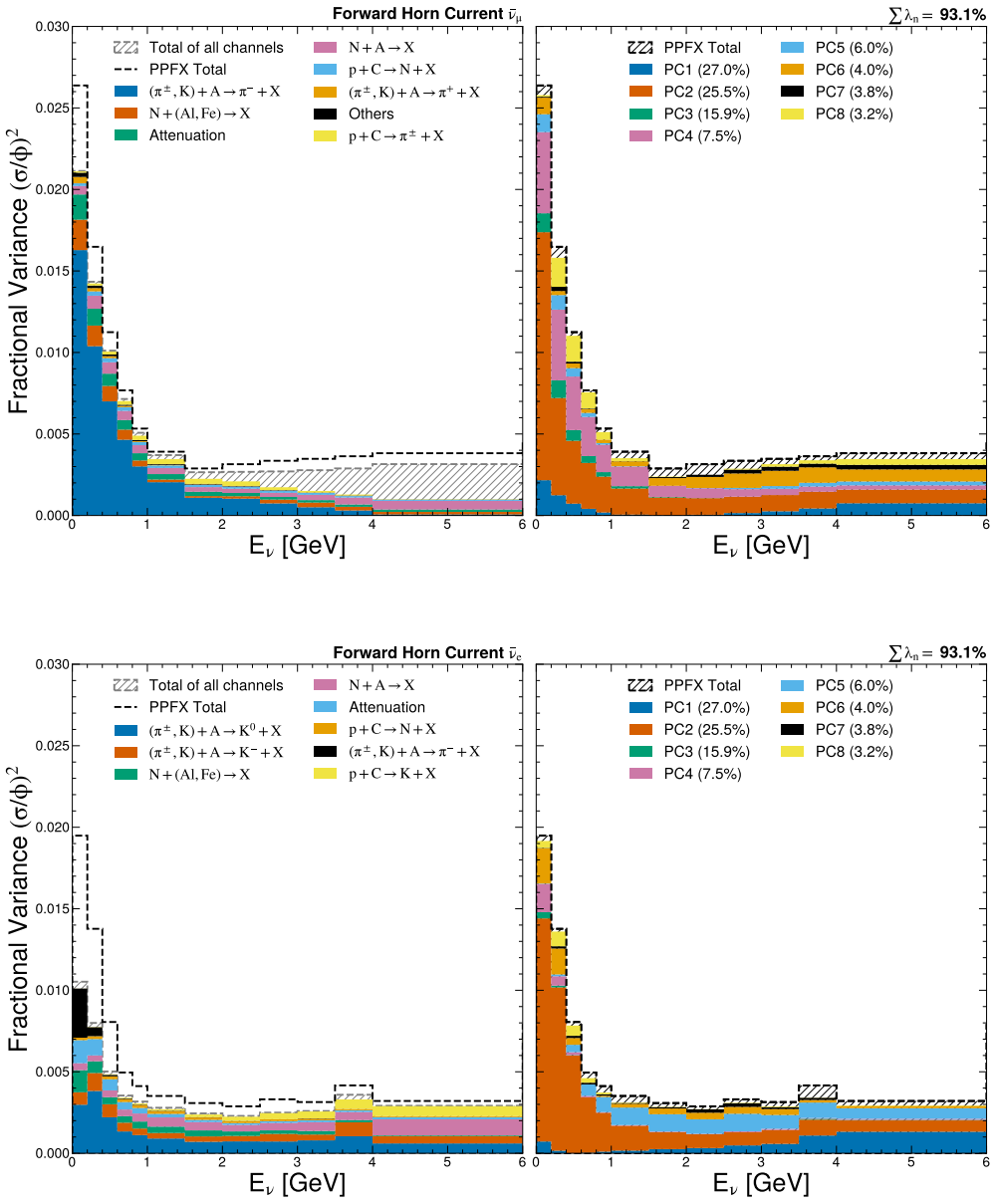

Figure I.5: Fractional variance comparison between physics and PCA descriptions by outgoing meson (FHC, $\bar{\nu}$).

I.2.2 Reverse Horn Current

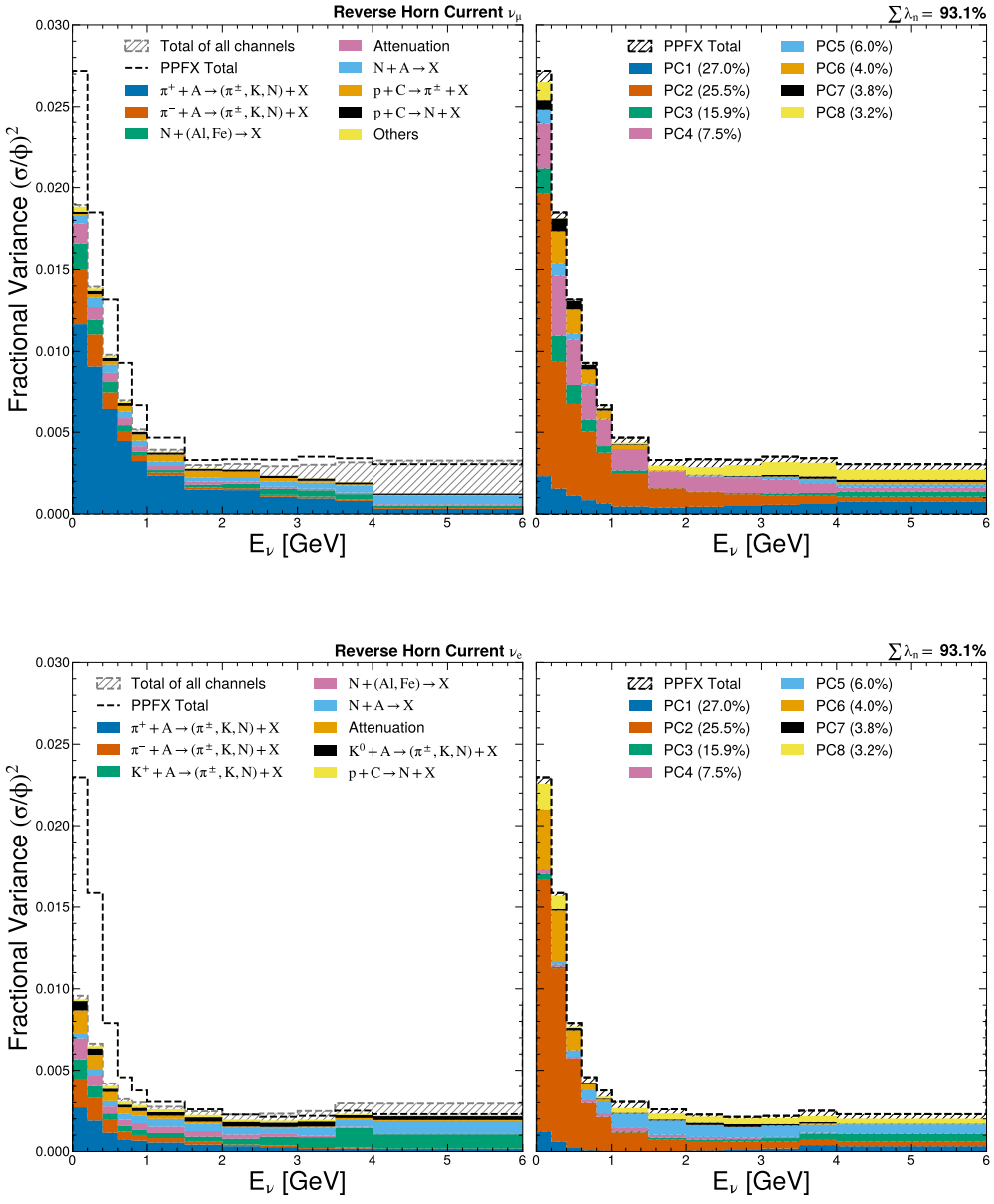

Figure I.6: Fractional variance comparison between physics and PCA descriptions by incoming meson (RHC, ν).

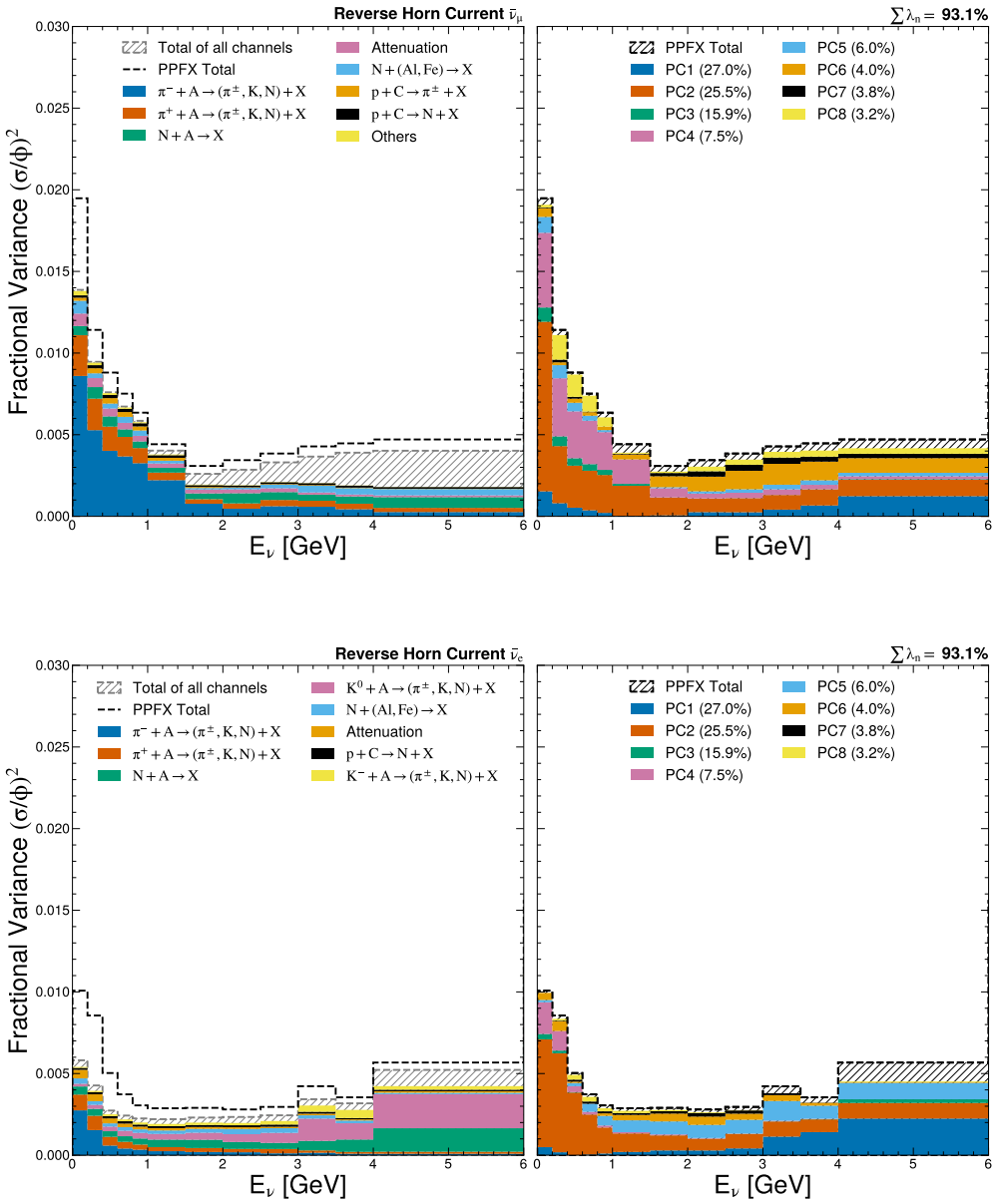

Figure I.7: Fractional variance comparison between physics and PCA descriptions by incoming meson (RHC, $\bar{\nu}$).

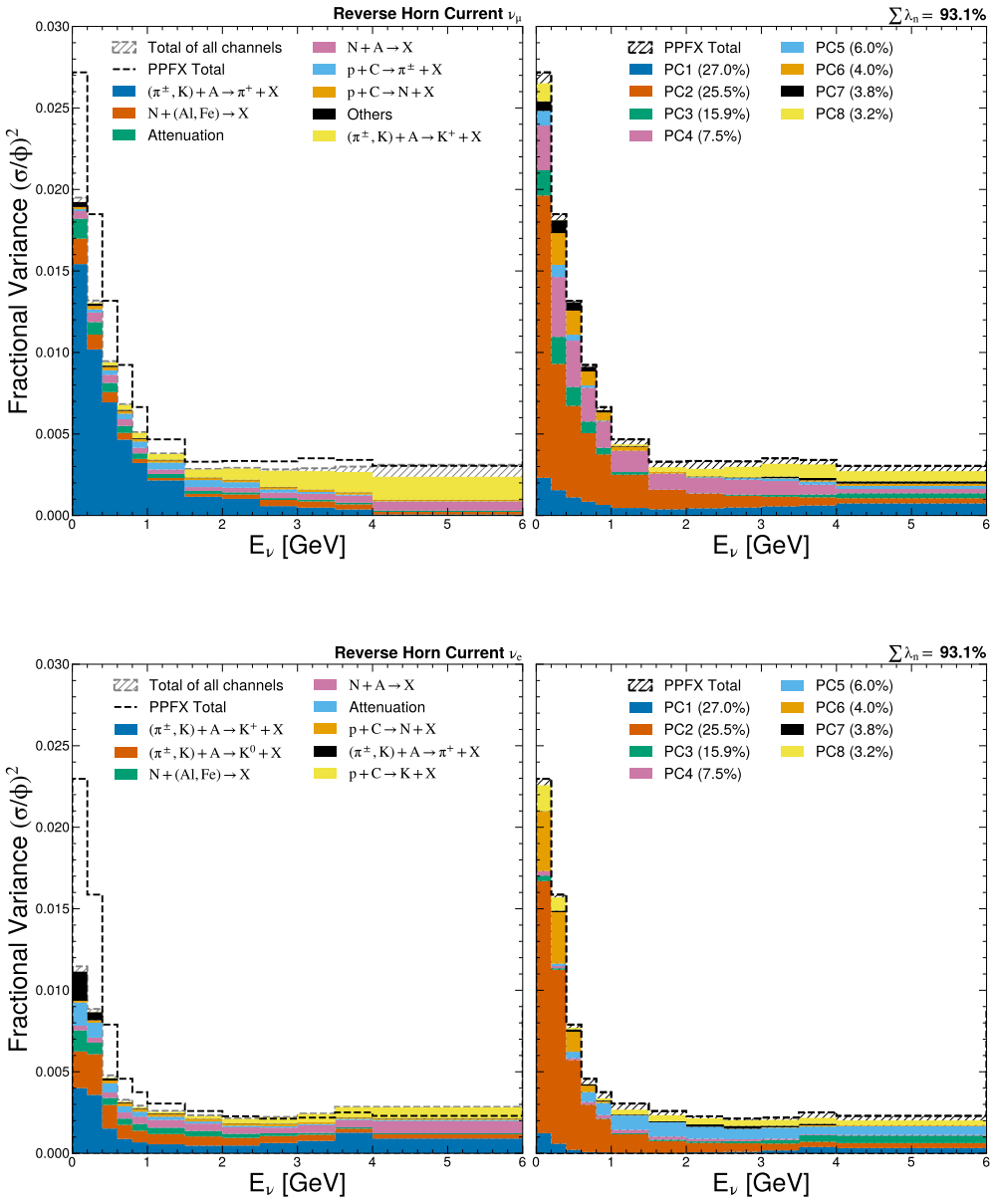

Figure I.8: Fractional variance comparison between physics and PCA descriptions by outgoing meson (RHC, ν).

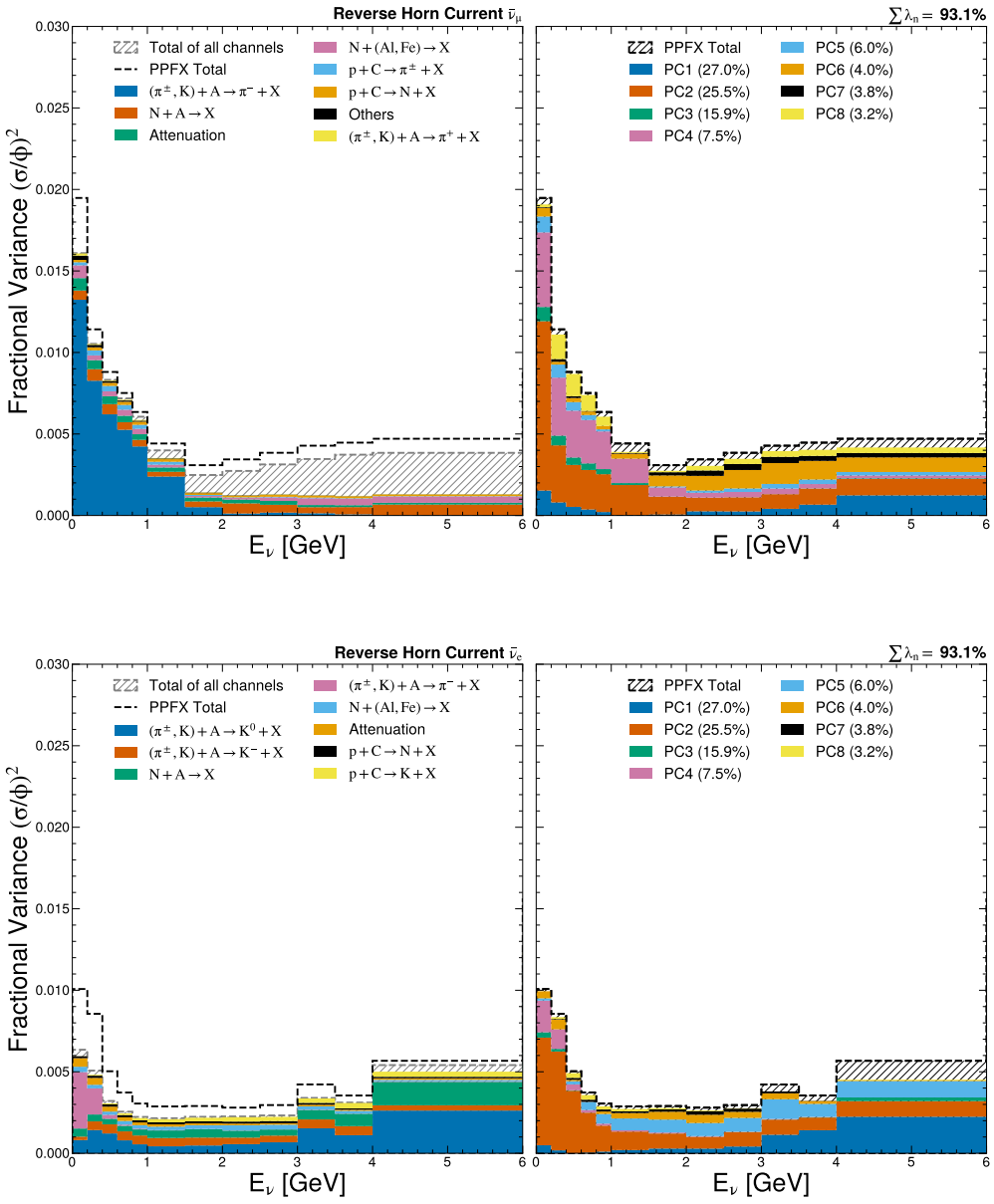

Figure I.9: Fractional variance comparison between physics and PCA descriptions by outgoing meson (RHC, $\bar{\nu}$).

J NuMI Beamline Monte Carlo Samples

Run 15 (nominal)	
Beam spot sigma	1.3 mm
Horn current	±200 kA
Horn water layer	1 mm
Target z-position	−143.3 cm
Decay pipe B-field	none

Table J.1: NuMI Monte Carlo simulation nominal configuration

Run ID	Description	Inclusion Status
8	horn current +2 kA	included
9	horn current −2 kA	excluded
10	horn1 position $x + 0.3$ cm	included
11	horn1 position $x - 0.3$ cm	included
12	horn1 position $y + 0.3$ cm	included
13	horn1 position $y - 0.3$ cm	included
14	beam spot size +0.2 cm	included
15	nominal	included
16	beam spot size −0.2 cm	included
17	horn2 position $x + 0.3$ cm	excluded
18	horn2 position $x - 0.3$ cm	excluded
19	horn2 position $y + 0.3$ cm	excluded
20	horn2 position $y - 0.3$ cm	excluded
21	horn water layer +1 mm	included ($E_\nu \leq 1$ GeV)
22	horn water layer −1 mm	included ($E_\nu \leq 1$ GeV)
24	beam shift $x + 1$ mm	included
25	beam shift $x - 1$ mm	included
26	beam shift $y + 1$ mm	included
27	beam shift $y - 1$ mm	included
28	target position $z + 7$ mm	excluded
29	target position $z - 7$ mm	excluded
30	B-field in decay pipe	excluded
32	beam divergence 54 µrad	included ($E_\nu \geq 1$ GeV)

Table J.2: Tabulation of the NuMI beamline focusing samples and their inclusion status in this analysis. Samples marked as "excluded" were consistent with statistical fluctuations present in the nominal sample.

K Beam Focusing Flux Fractional Shifts

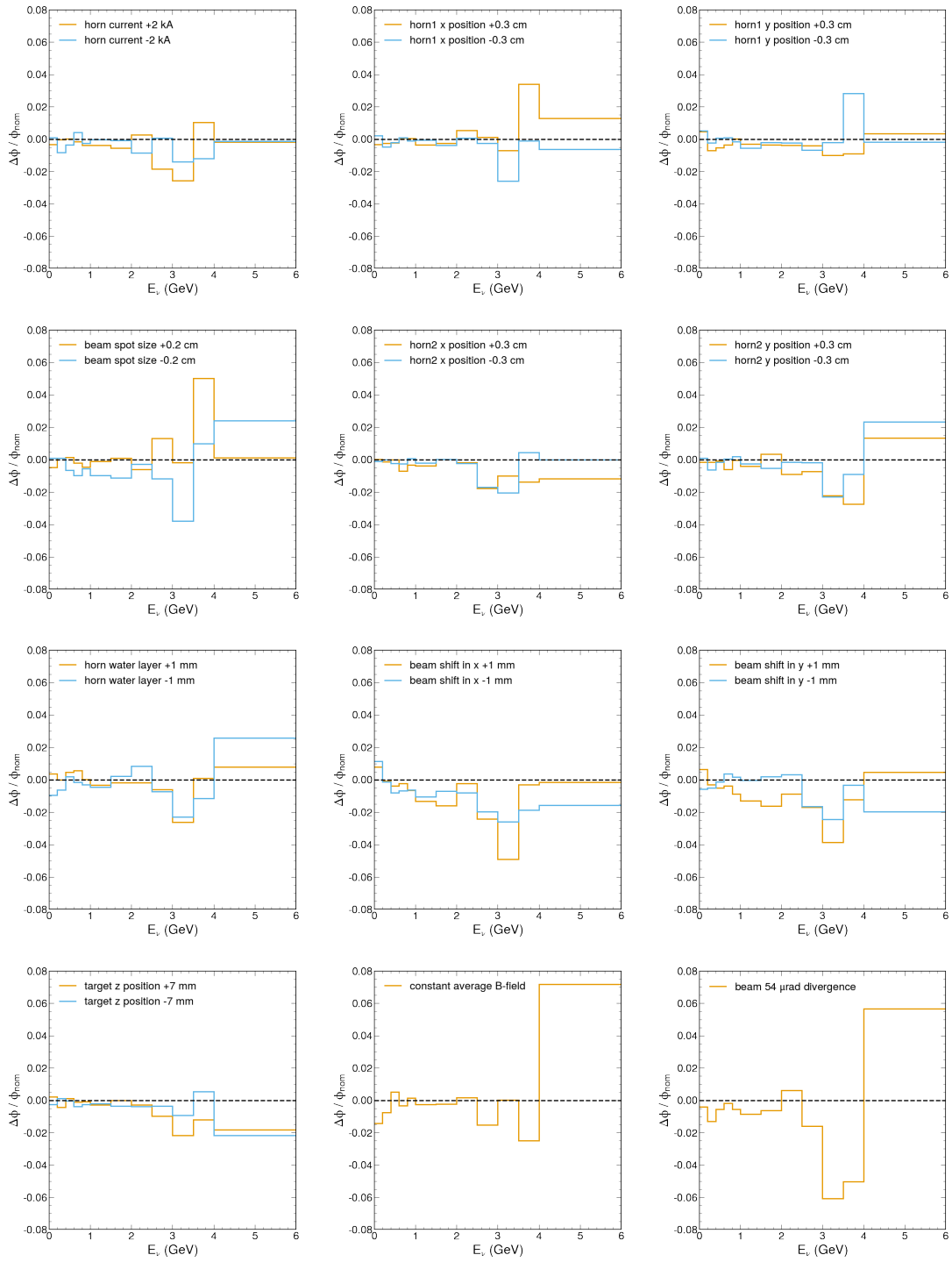

Figure K.1: Beam focusing systematic shifts in the fractional scale (FHC, ν_e).

L Beamline Focusing Systematic Matrices

L.1 Covariance Matrices

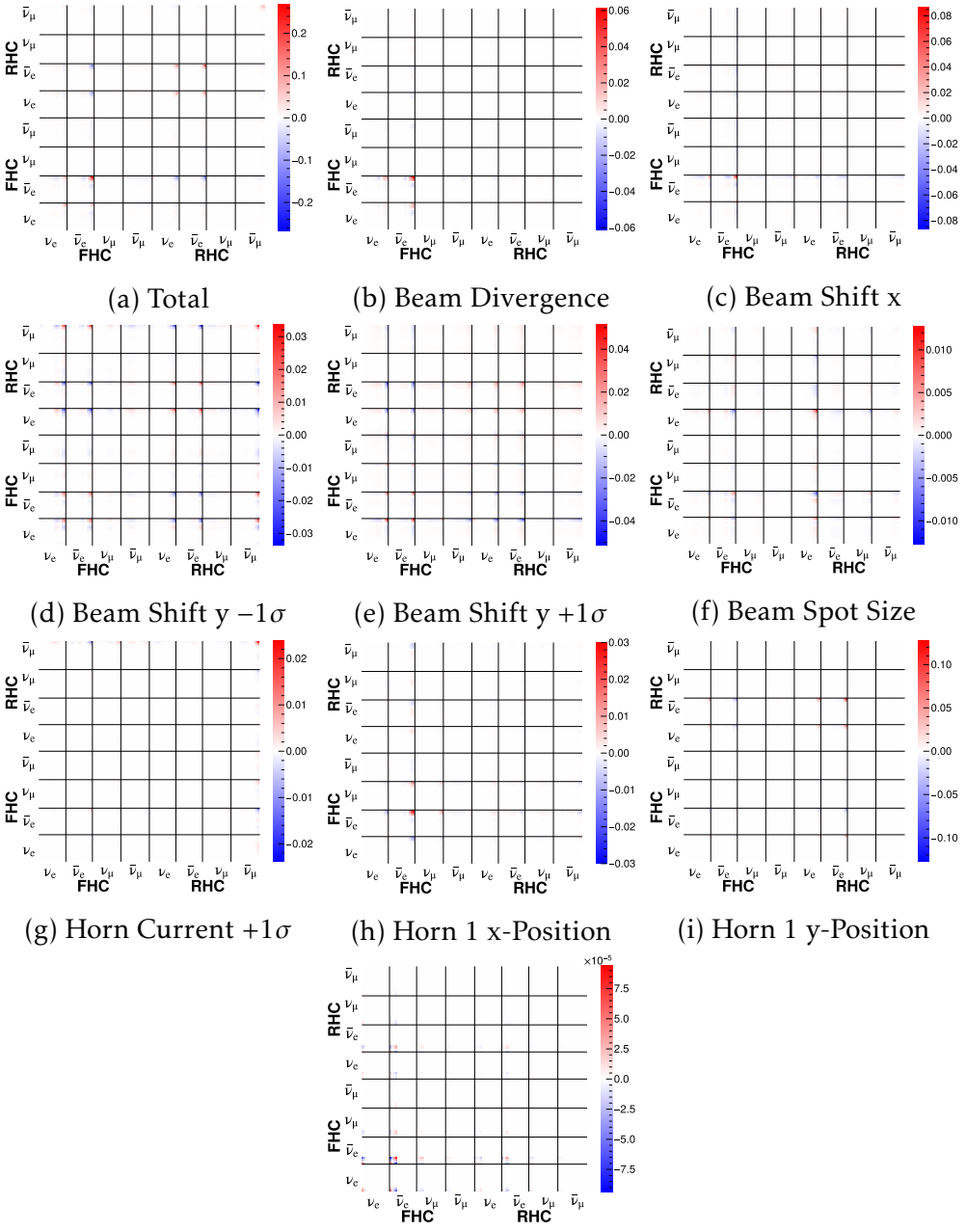

(a) Total

(b) Beam Divergence

(c) Beam Shift x

(d) Beam Shift y -1σ

(e) Beam Shift y $+1\sigma$

(f) Beam Spot Size

(g) Horn Current $+1\sigma$

(h) Horn 1 x-Position

(i) Horn 1 y-Position

(j) Horn Water Layer

Figure L.1: All beam focusing systematic covariance matrices.

L.2 Correlation Matrices

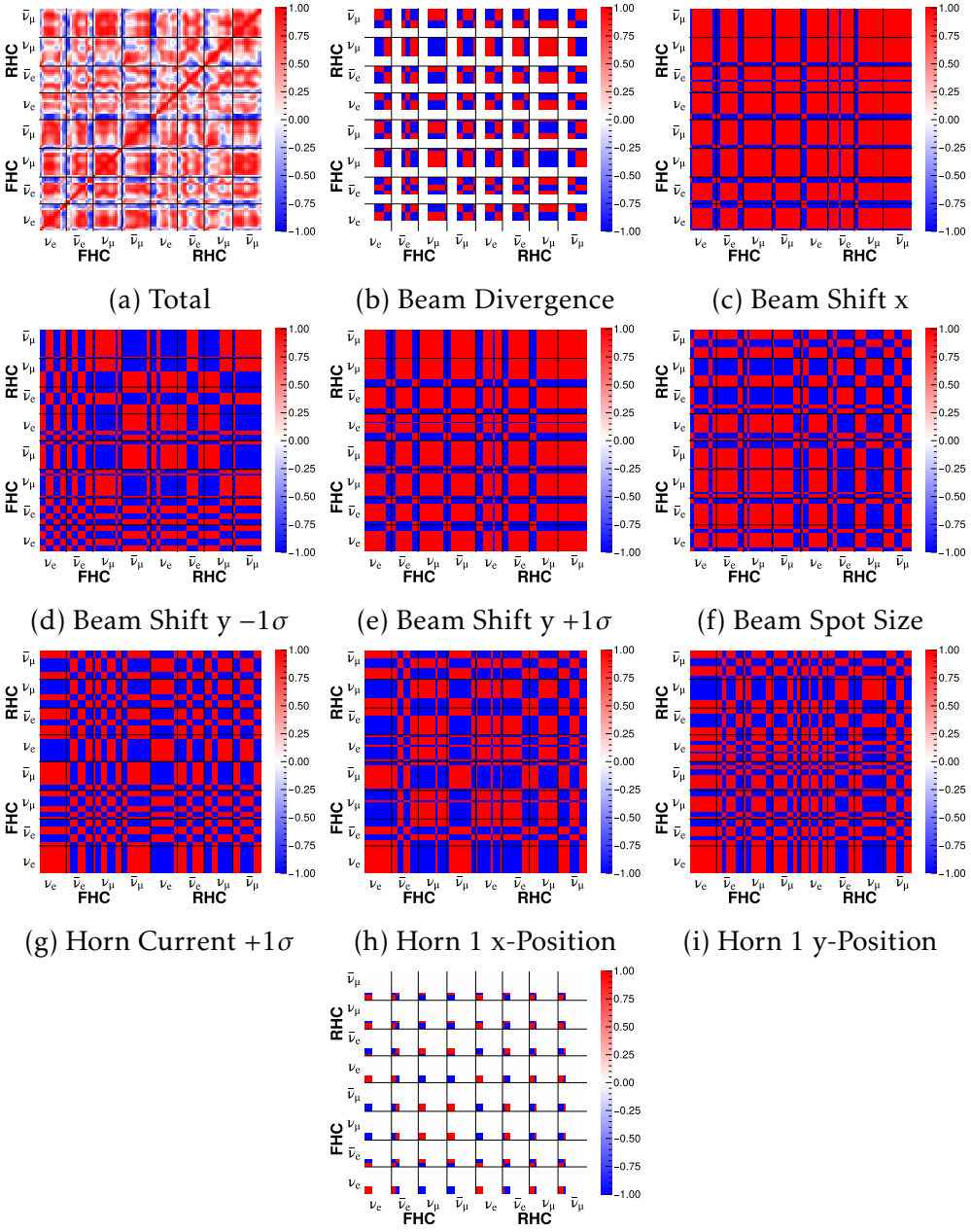

(a) Total (b) Beam Divergence (c) Beam Shift x

(d) Beam Shift y -1σ (e) Beam Shift y $+1\sigma$ (f) Beam Spot Size

(g) Horn Current $+1\sigma$ (h) Horn 1 x-Position (i) Horn 1 y-Position

(j) Horn Water Layer

Figure L.2: All beam focusing systematic correlation matrices.

M Differences Between the 700 KW and 1 MW NuMI Beamline Geometries

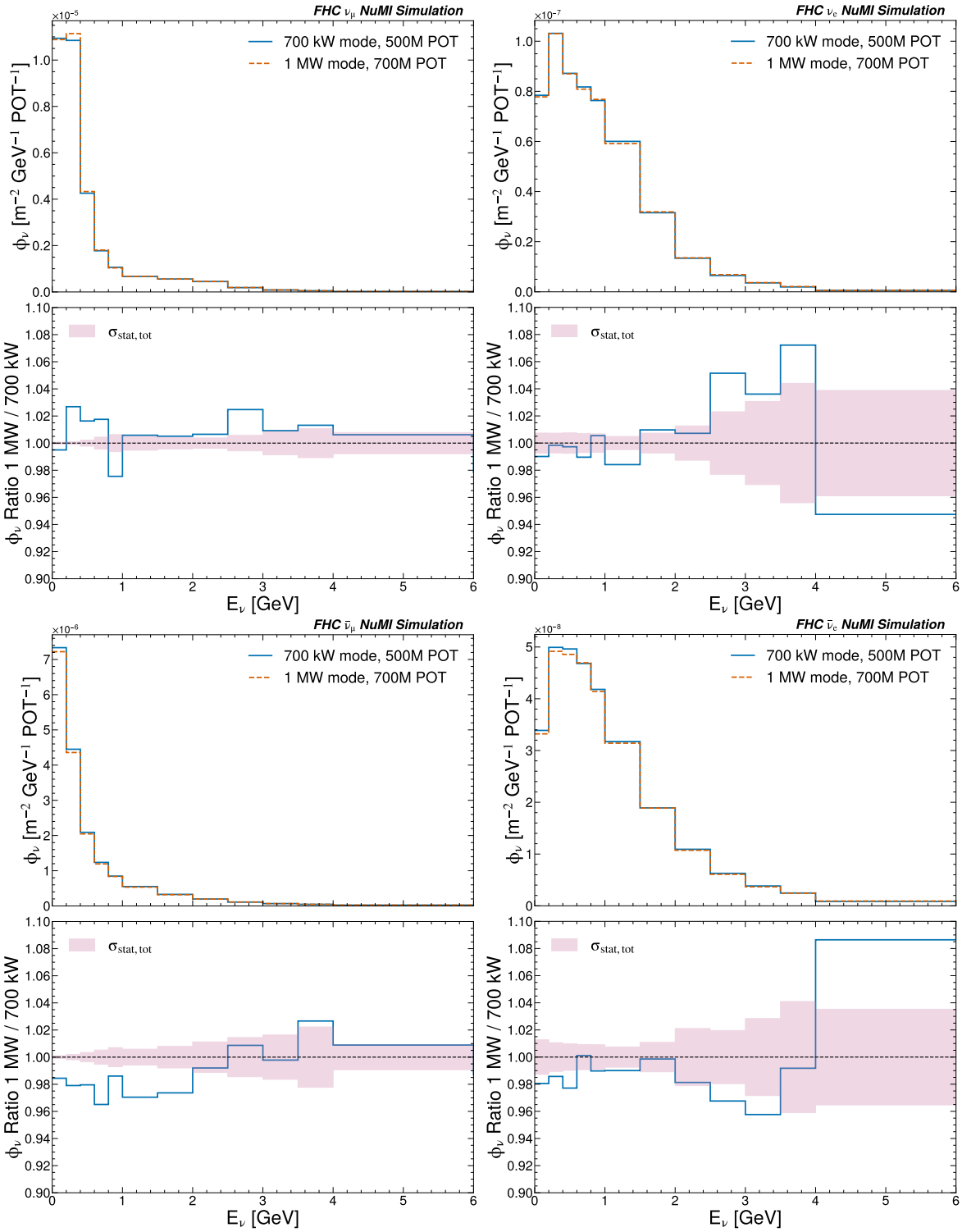

Figure M.1: Comparison of the 700 kW and 1 MW NuMI beam geometries (FHC).

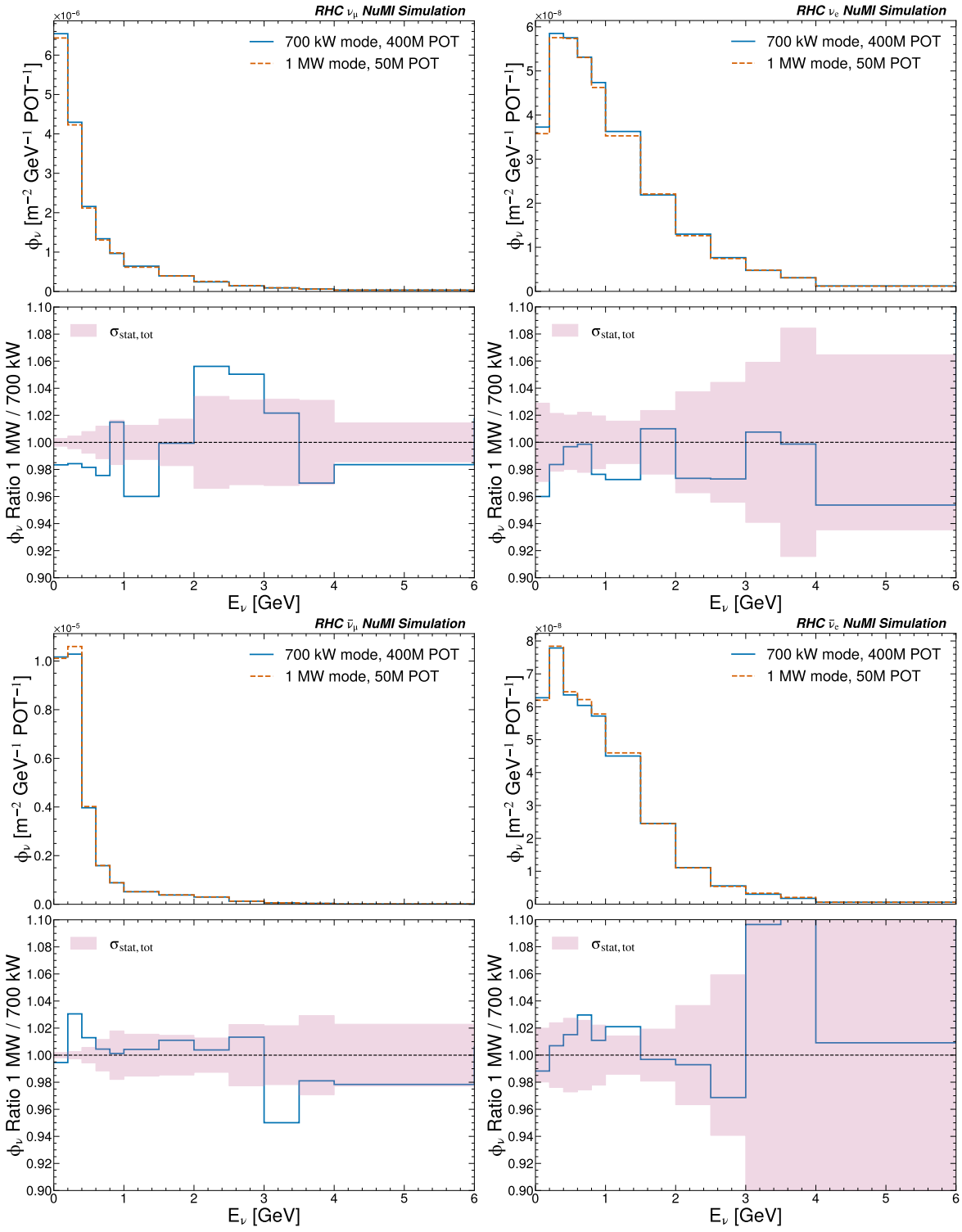

Figure M.2: Comparison of the 700 kW and 1 MW NuMI beam geometries (RHC).

N The NuMI Flux Prediction

N.1 Flux Prediction with Uncertainties

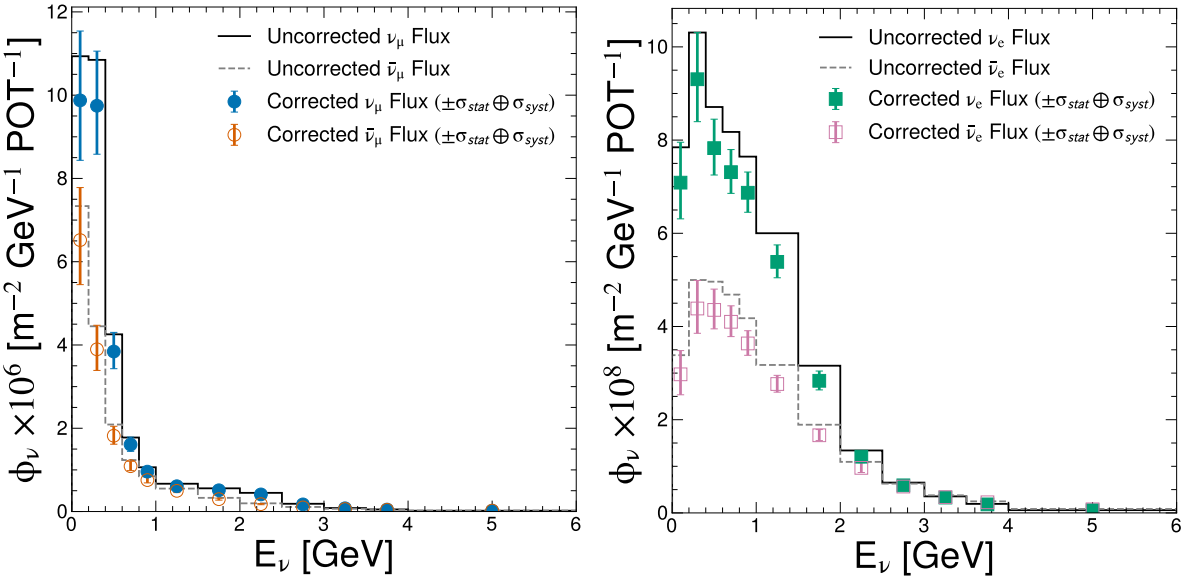

(a) ν_μ and $\bar{\nu}_\mu$ (b) ν_e and $\bar{\nu}_e$

Figure N.1: Forward Horn Current

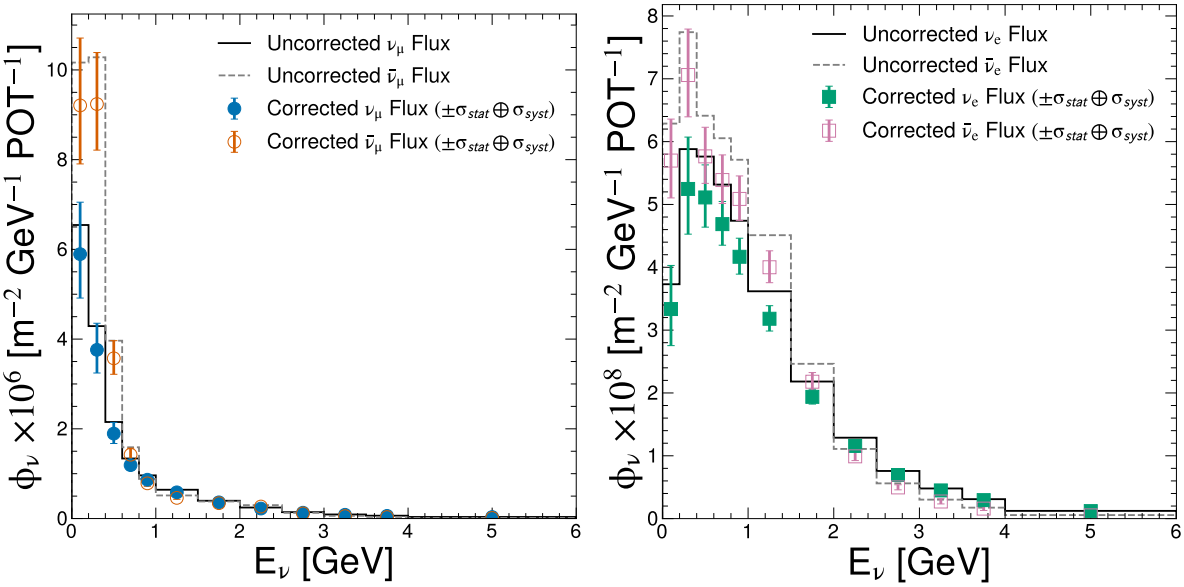

(a) ν_μ and $\bar{\nu}_\mu$ (b) ν_e and $\bar{\nu}_e$

Figure N.2: Reverse Horn Current

N.2 Flux Prediction by Parent Particle

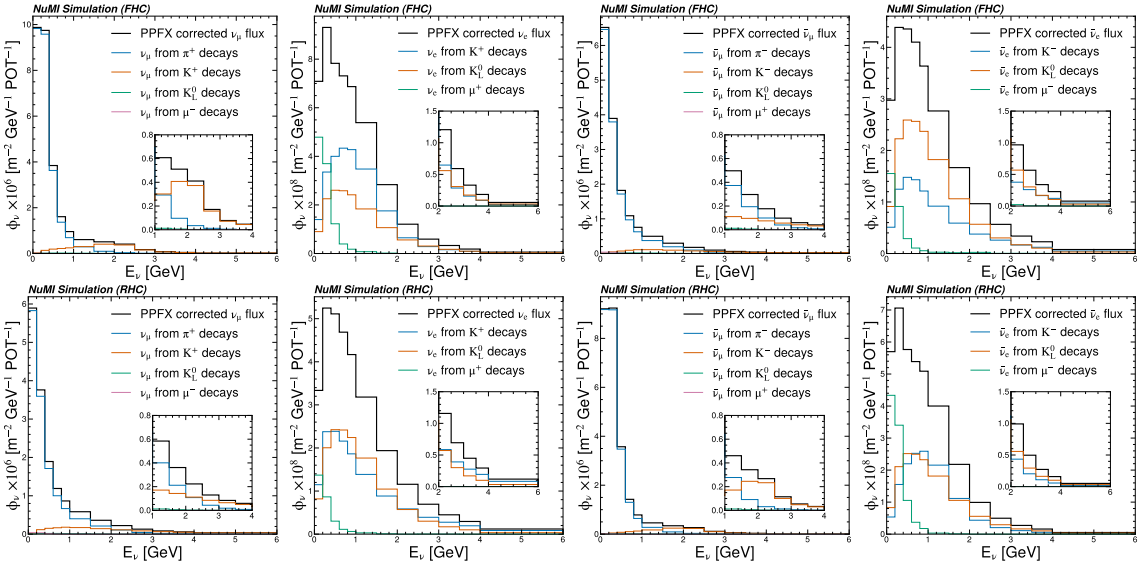

(a) Absolute

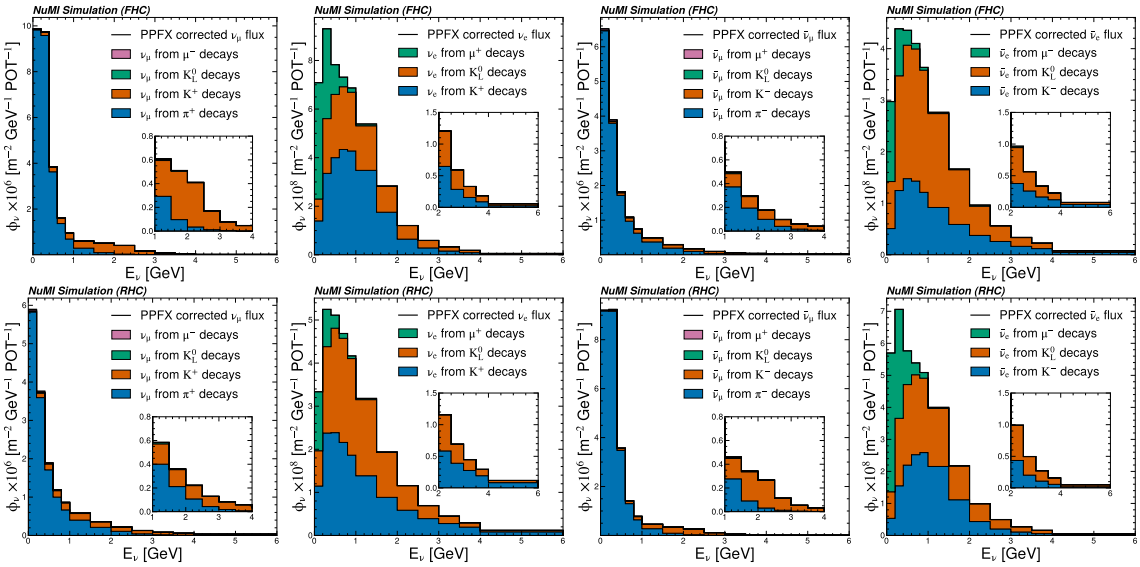

(b) Stacked

N.3 Flux Tables

N.3.1 Flux at the Center of the ICARUS TPC

Table N.1: The predicted NuMI neutrino flux at the geometrical center of the ICARUS TPC. Refer to Table 3.1 for the coordinates.

		Flux [$m^{-2}GeV^{-1}POT^{-1}$]							
		FHC				RHC			
Bin	Interval [GeV]	ν_e $\times 10^8$	$\bar{\nu}_e$ $\times 10^8$	ν_μ $\times 10^6$	$\bar{\nu}_\mu$ $\times 10^6$	ν_e $\times 10^8$	$\bar{\nu}_e$ $\times 10^8$	ν_μ $\times 10^6$	$\bar{\nu}_\mu$ $\times 10^6$
1	[0.0, 0.2)	1.417	0.595	1.975	1.304	0.667	1.140	1.179	1.842
2	[0.2, 0.4)	1.861	0.877	1.949	0.779	1.049	1.412	0.752	1.848
3	[0.4, 0.6)	1.566	0.871	0.769	0.364	1.022	1.153	0.379	0.714
4	[0.6, 0.8)	1.462	0.820	0.322	0.218	0.937	1.078	0.238	0.285
5	[0.8, 1.0)	1.374	0.727	0.192	0.151	0.833	1.018	0.173	0.157
6	[1.0, 1.5)	2.693	1.383	0.304	0.248	1.590	2.000	0.292	0.230
7	[1.5, 2.0)	1.417	0.833	0.255	0.149	0.969	1.089	0.181	0.171
8	[2.0, 2.5)	0.603	0.483	0.205	0.089	0.578	0.496	0.112	0.134
9	[2.5, 3.0)	0.296	0.283	0.086	0.049	0.347	0.248	0.065	0.057
10	[3.0, 3.5)	0.165	0.169	0.039	0.030	0.224	0.136	0.042	0.027
11	[3.5, 4.0)	0.092	0.114	0.023	0.021	0.147	0.080	0.030	0.017
12	[4.0, 6.0)	0.114	0.155	0.038	0.042	0.238	0.103	0.068	0.026
13	[6.0, 8.0)	0.014	0.023	0.008	0.015	0.037	0.016	0.026	0.006
14	[8.0, 12.0)	0.003	0.005	0.002	0.005	0.007	0.003	0.008	0.002
15	[12.0, 20.0]	0	0	9.9e-5	3.36e-4	0	0	4.89e-4	7.7e-5

N.3.2 Flux at the Top of the ICARUS TPC

Table N.2: The predicted NuMI neutrino flux at the upper limit of the ICARUS TPC active volume, above its geometrical center. Refer to Table 3.1 for the coordinates.

		Flux [$m^{-2}GeV^{-1}POT^{-1}$]							
		FHC				RHC			
Bin	Interval [GeV]	ν_e $\times 10^8$	$\bar{\nu}_e$ $\times 10^8$	ν_μ $\times 10^6$	$\bar{\nu}_\mu$ $\times 10^6$	ν_e $\times 10^8$	$\bar{\nu}_e$ $\times 10^8$	ν_μ $\times 10^6$	$\bar{\nu}_\mu$ $\times 10^6$
1	[0.0, 0.2)	1.395	0.588	1.952	1.288	0.659	1.121	1.166	1.822
2	[0.2, 0.4)	1.832	0.868	1.901	0.764	1.037	1.389	0.739	1.805
3	[0.4, 0.6)	1.542	0.858	0.730	0.356	1.012	1.135	0.370	0.678
4	[0.6, 0.8)	1.443	0.810	0.305	0.213	0.926	1.060	0.233	0.269
5	[0.8, 1.0)	1.349	0.717	0.186	0.148	0.824	0.998	0.171	0.151
6	[1.0, 1.5)	2.603	1.349	0.296	0.243	1.553	1.943	0.286	0.224
7	[1.5, 2.0)	1.331	0.803	0.254	0.144	0.928	1.029	0.176	0.169
8	[2.0, 2.5)	0.565	0.459	0.189	0.084	0.555	0.466	0.106	0.124
9	[2.5, 3.0)	0.275	0.268	0.079	0.046	0.329	0.231	0.061	0.053
10	[3.0, 3.5)	0.153	0.159	0.036	0.028	0.214	0.127	0.040	0.025
11	[3.5, 4.0)	0.085	0.106	0.022	0.019	0.141	0.073	0.028	0.016
12	[4.0, 6.0)	0.104	0.144	0.035	0.041	0.217	0.095	0.066	0.024
13	[6.0, 8.0)	0.013	0.020	0.007	0.014	0.033	0.015	0.024	0.005
14	[8.0, 12.0)	0.002	0.004	0.002	0.004	0.006	0.002	0.007	0.001
15	[12.0, 20.0]	0	0	8.7e-5	2.67e-4	0	0	4.02e-4	6.0e-5

N.3.3 Flux at the Bottom of the ICARUS TPC

Table N.3: The predicted NuMI neutrino flux at the lower limit of the ICARUS TPC active volume, below its geometrical center. Refer to Table 3.1 for the coordinates.

		Flux [$m^{-2}GeV^{-1}POT^{-1}$]							
		FHC				RHC			
Bin	Interval [GeV]	ν_e $\times 10^8$	$\bar{\nu}_e$ $\times 10^8$	ν_μ $\times 10^6$	$\bar{\nu}_\mu$ $\times 10^6$	ν_e $\times 10^8$	$\bar{\nu}_e$ $\times 10^8$	ν_μ $\times 10^6$	$\bar{\nu}_\mu$ $\times 10^6$
1	[0.0, 0.2)	1.439	0.600	2.000	1.320	0.675	1.155	1.192	1.862
2	[0.2, 0.4)	1.893	0.888	1.997	0.794	1.060	1.440	0.766	1.891
3	[0.4, 0.6)	1.590	0.883	0.810	0.374	1.037	1.168	0.388	0.753
4	[0.6, 0.8)	1.481	0.829	0.340	0.223	0.947	1.098	0.243	0.302
5	[0.8, 1.0)	1.394	0.739	0.199	0.154	0.843	1.030	0.176	0.163
6	[1.0, 1.5)	2.789	1.419	0.311	0.253	1.631	2.066	0.298	0.237
7	[1.5, 2.0)	1.513	0.869	0.256	0.153	1.006	1.150	0.185	0.173
8	[2.0, 2.5)	0.648	0.500	0.222	0.092	0.608	0.532	0.117	0.144
9	[2.5, 3.0)	0.320	0.298	0.093	0.053	0.366	0.265	0.069	0.062
10	[3.0, 3.5)	0.176	0.177	0.042	0.032	0.232	0.147	0.044	0.029
11	[3.5, 4.0)	0.098	0.124	0.025	0.021	0.158	0.086	0.031	0.018
12	[4.0, 6.0)	0.125	0.168	0.041	0.044	0.260	0.113	0.070	0.027
13	[6.0, 8.0)	0.016	0.027	0.009	0.017	0.042	0.018	0.029	0.007
14	[8.0, 12.0)	0.003	0.005	0.002	0.006	0.008	0.003	0.009	0.002
15	[12.0, 20.0]	0	0	1.22e-4	3.99e-4	0	0	6.01e-4	9.4e-5

O Total Flux Uncertainties

O.1 Forward Horn Current

Interval [GeV]	ν_e	$\bar{\nu}_e$	$\nu_e + \bar{\nu}_e$	ν_μ	$\bar{\nu}_\mu$	$\nu_\mu + \bar{\nu}_\mu$	$\frac{\nu_e+\bar{\nu}_e}{\nu_\mu+\bar{\nu}_\mu}$
[0.0, 0.2]	0.175	0.105	0.121	0.167	0.142	0.134	0.070
[0.0, 0.4]	0.151	0.098	0.112	0.152	0.123	0.114	0.080
[0.0, 0.6]	0.128	0.088	0.098	0.145	0.118	0.109	0.079
[0.0, 0.8]	0.110	0.080	0.087	0.140	0.117	0.106	0.077
[0.0, 1.0]	0.100	0.074	0.079	0.137	0.115	0.104	0.075
[0.0, 1.5]	0.085	0.066	0.067	0.129	0.113	0.100	0.074
[0.0, 2.0]	0.079	0.063	0.063	0.125	0.110	0.097	0.074
[0.0, 2.5]	0.076	0.062	0.061	0.121	0.108	0.095	0.073
[0.0, 3.0]	0.075	0.061	0.060	0.120	0.107	0.094	0.072
[0.0, 3.5]	0.073	0.061	0.060	0.118	0.106	0.094	0.072
[0.0, 4.0]	0.073	0.061	0.059	0.118	0.106	0.093	0.071
[0.0, 6.0]	0.072	0.061	0.059	0.116	0.106	0.092	0.071
[0.0, 8.0]	0.072	0.061	0.058	0.115	0.106	0.092	0.070
[0.0, 12.0]	0.072	0.061	0.058	0.115	0.106	0.092	0.070
[0.0, 20.0]	0.072	0.061	0.058	0.115	0.106	0.092	0.070
[0.2, 20.0]	0.072	0.061	0.058	0.115	0.106	0.092	0.070
[0.4, 20.0]	0.066	0.061	0.055	0.094	0.092	0.076	0.067
[0.6, 20.0]	0.061	0.060	0.051	0.077	0.077	0.061	0.053
[0.8, 20.0]	0.059	0.061	0.050	0.068	0.067	0.053	0.043
[1.0, 20.0]	0.058	0.061	0.049	0.062	0.063	0.049	0.038
[1.5, 20.0]	0.058	0.061	0.048	0.060	0.062	0.047	0.035
[2.0, 20.0]	0.058	0.064	0.049	0.059	0.065	0.046	0.035
[2.5, 20.0]	0.060	0.075	0.050	0.064	0.070	0.049	0.036
[3.0, 20.0]	0.066	0.108	0.058	0.064	0.076	0.049	0.042
[3.5, 20.0]	0.080	0.143	0.072	0.063	0.082	0.050	0.060
[4.0, 20.0]	0.103	0.156	0.091	0.064	0.087	0.052	0.079
[6.0, 20.0]	0.129	0.165	0.117	0.065	0.093	0.054	0.104
[8.0, 20.0]	0.268	0.350	0.272	0.094	0.143	0.079	0.291
[12.0, 20.0]	0.462	0.743	0.503	0.205	0.261	0.178	0.600

O.2 Reverse Horn Current

Interval [GeV]	ν_e	$\bar{\nu}_e$	$\nu_e + \bar{\nu}_e$	ν_μ	$\bar{\nu}_\mu$	$\nu_\mu + \bar{\nu}_\mu$	$\frac{\nu_e+\bar{\nu}_e}{\nu_\mu+\bar{\nu}_\mu}$
[0.0, 0.2]	0.110	0.148	0.115	0.146	0.165	0.136	0.057
[0.0, 0.4]	0.102	0.131	0.107	0.130	0.148	0.118	0.071

[0.0, 0.6]	0.091	0.115	0.096	0.126	0.141	0.112	0.074
[0.0, 0.8]	0.082	0.102	0.085	0.124	0.136	0.110	0.074
[0.0, 1.0]	0.076	0.093	0.078	0.122	0.133	0.108	0.075
[0.0, 1.5]	0.068	0.081	0.068	0.119	0.127	0.104	0.075
[0.0, 2.0]	0.066	0.077	0.065	0.115	0.123	0.100	0.075
[0.0, 2.5]	0.065	0.076	0.065	0.112	0.121	0.098	0.074
[0.0, 3.0]	0.065	0.076	0.064	0.111	0.119	0.097	0.073
[0.0, 3.5]	0.065	0.076	0.064	0.110	0.118	0.096	0.073
[0.0, 4.0]	0.065	0.075	0.064	0.110	0.118	0.096	0.073
[0.0, 6.0]	0.065	0.073	0.063	0.110	0.117	0.095	0.072
[0.0, 8.0]	0.065	0.072	0.063	0.109	0.116	0.095	0.072
[0.0, 12.0]	0.065	0.072	0.063	0.109	0.116	0.095	0.072
[0.0, 20.0]	0.065	0.072	0.063	0.109	0.116	0.095	0.072
[0.2, 20.0]	0.065	0.072	0.063	0.109	0.116	0.095	0.072
[0.4, 20.0]	0.063	0.070	0.060	0.096	0.096	0.080	0.068
[0.6, 20.0]	0.062	0.067	0.058	0.080	0.083	0.065	0.052
[0.8, 20.0]	0.062	0.065	0.057	0.070	0.077	0.057	0.042
[1.0, 20.0]	0.064	0.065	0.058	0.066	0.075	0.054	0.036
[1.5, 20.0]	0.065	0.065	0.059	0.064	0.073	0.052	0.033
[2.0, 20.0]	0.069	0.070	0.063	0.065	0.070	0.050	0.036
[2.5, 20.0]	0.076	0.074	0.066	0.067	0.070	0.051	0.043
[3.0, 20.0]	0.078	0.070	0.064	0.071	0.072	0.052	0.044
[3.5, 20.0]	0.071	0.092	0.062	0.073	0.076	0.055	0.057
[4.0, 20.0]	0.115	0.153	0.089	0.077	0.081	0.058	0.103
[6.0, 20.0]	0.175	0.212	0.132	0.081	0.086	0.061	0.155
[8.0, 20.0]	0.325	0.391	0.298	0.126	0.104	0.081	0.333
[12.0, 20.0]	0.508	0.645	0.501	0.283	0.165	0.137	0.540

References

[1] M. Antonello et al., *ICARUS at FNAL*, 2013, https://arxiv.org/abs/1312.7252.

[2] P. Abratenko et al. (ICARUS Collaboration), "ICARUS at the Fermilab Short-Baseline Neutrino program: initial operation", Eur. Phys. J. C **83**, 467 (2023).

[3] A. Aguilar et al. (LSND Collaboration), "Evidence for neutrino oscillations from the observation of $\bar{\nu}_e$ appearance in a $\bar{\nu}_\mu$ beam", Phys. Rev. D **64**, 112007 (2001), https://link.aps.org/doi/10.1103/PhysRevD.64.112007.

[4] A. A. Aguilar-Arevalo et al. (MiniBooNE Collaboration), "Significant Excess of Electronlike Events in the MiniBooNE Short-Baseline Neutrino Experiment", Phys. Rev. Lett. **121**, 221801 (2018), https://link.aps.org/doi/10.1103/PhysRevLett.121.221801.

[5] F. Kaether et al., "Reanalysis of the Gallex solar neutrino flux and source experiments", Physics Letters B **685**, 47–54 (2010), https://www.sciencedirect.com/science/article/pii/S0370269310000729.

[6] J. N. Abdurashitov et al. (SAGE Collaboration), "Measurement of the solar neutrino capture rate with gallium metal. III. Results for the 2002–2007 data-taking period", Phys. Rev. C **80**, 015807 (2009), https://link.aps.org/doi/10.1103/PhysRevC.80.015807.

[7] A. P. Serebrov et al. (NEUTRINO-4), "First Observation of the Oscillation Effect in the Neutrino-4 Experiment on the Search for the Sterile Neutrino", Pisma Zh. Eksp. Teor. Fiz. **109**, 209–218 (2019).

[8] P. A. Machado, O. Palamara, and D. W. Schmitz, "The short-baseline neutrino program at fermilab", Annual Review of Nuclear and Particle Science **69**, 363–387 (2019), https://doi.org/10.1146/annurev-nucl-101917-020949.

[9] B. Abi et al. (DUNE Collaboration), *The DUNE Far Detector Interim Design Report Volume 1: Physics, Technology and Strategies*, 2018, https://arxiv.org/abs/1807.10334.

[10] K. Mistry, "First Measurement of the Flux-Averaged Differential Charged-Current Electron-Neutrino and Antineutrino Cross Section on Argon with the MicroBooNE Detector", PhD Thesis, The University of Manchester (2022), https://research.manchester.ac.uk/files/213185188/FULL_TEXT.PDF.

[11] L. Aliaga, "Neutrino Flux Prediction for the NuMI Beamline", PhD thesis (The College of William and Mary, Jan. 2016), https://www.osti.gov/biblio/1250884.

[12] L. Aliaga et al. (MINERνA Collaboration), "Neutrino flux predictions for the NuMI beam", Phys. Rev. D **94**, 092005 (2016), https://link.aps.org/doi/10.1103/PhysRevD.94.092005.

[13] *PPFX Redmine page*, (access requires Fermilab account), https://cdcvs.fnal.gov/redmine/projects/ppfx.

[14] *PPFX github repository*, (repository migrated from Redmine in January 2023), https://github.com/kordosky/ppfx.

[15] NA61/SHINE Experiment, https://shine.web.cern.ch/.

[16] T. Akaishi et al., *EMPHATIC: A proposed experiment to measure hadron scattering and production cross sections for improved neutrino flux predictions*, 2019, https://arxiv.org/abs/1912.08841.

[17] P. Adamson et al., "The NuMI neutrino beam", Nucl. Instrum. Methods. Phys. Res. A **806**, 279–306 (2016), https://www.sciencedirect.com/science/article/pii/S016890021501027X.

[18] M. A. Acero et al. (NOvA Collaboration), "First measurement of neutrino oscillation parameters using neutrinos and antineutrinos by NOvA", Phys. Rev. Lett. **123**, 151803 (2019), https://link.aps.org/doi/10.1103/PhysRevLett.123.151803.

[19] K. Yonehara (NuMI Collaboration), "Megawatt upgrade of NuMI target system", PoS **NuFact2021**, 107 (2022).

[20] S. Agostinelli et al. (GEANT4 Collaboration), "Geant4 – a simulation toolkit", Nucl. Instrum. Methods. Phys. Res. A **506**, 250–303 (2003), https://www.sciencedirect.com/science/article/pii/S0168900203013688.

[21] R. Hatcher, *Proposal for a Unified "Flux" N-tuple Format*, MINOS docdb 9070-v4, 2012.

[22] N. Bostan, "Application of hadron production data to Fermilab neutrino beam simulations", Neutrino 2022 poster (2022).

[23] L. Aliaga *et al.*, *NuMI flux systematic uncertainties for NOvA third analyses*, NOνA docdb 17608.
Data path: /pnfs/numix/flux/g4numi_syst_3rd_ana/test_g4numi_v6, 2017.

[24] A. Menegolli, M. Torti, *ICARUS geometry update*, SBN docdb 21693-v3.

[25] A. Aduszkiewicz, *ICARUS location with respect to the NuMI beam line*, SBN docdb 22998-v2.

[26] R. H. Milburn (MINOS Collaboration), *Neutrino beam Simulation using PAW with Weighted Monte Carlos*, MINOS docdb 109.

[27] SBNSoftware, *sbndata*, https://github.com/SBNSoftware/sbndata, 2023.

[28] A. Wood, *Flux-Tool*, https://github.com/woodtp/flux-tool, 2023.

[29] *Proceedings of the 1974 CERN School of Computing: Godøysund, Norway 11 - 24 Aug 1974. 3rd CERN School of Computing*, CERN (CERN, Geneva, 1974), pp. 292–298, https://cds.cern.ch/record/186223.

[30] A. Wood, *NuMI at ICARUS Flux Systematics (Products File)*, https://gitlab.com/apwood-physics/numi-at-icarus-flux-systematics, 2021.

[31] R. L. Workman et al. (Particle Data Group), "Review of Particle Physics", PTEP **2022**, 083C01 (2022).

[32] Data set prepared with the same parameters as the one in Ref. [23].
Data path: /pnfs/numix/flux/g4numi_syst_3rd_ana/testDecayPipeField.